

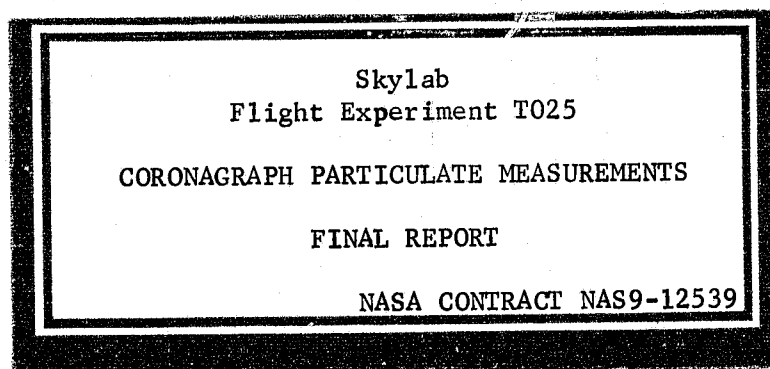
## **General Disclaimer**

### **One or more of the Following Statements may affect this Document**

- This document has been reproduced from the best copy furnished by the organizational source. It is being released in the interest of making available as much information as possible.
- This document may contain data, which exceeds the sheet parameters. It was furnished in this condition by the organizational source and is the best copy available.
- This document may contain tone-on-tone or color graphs, charts and/or pictures, which have been reproduced in black and white.
- This document is paginated as submitted by the original source.
- Portions of this document are not fully legible due to the historical nature of some of the material. However, it is the best reproduction available from the original submission.

NASA CR-

141855



(NASA-CP-141855) CORONAGRAPH PARTICULATE  
MEASUREMENTS. SKYLAB FLIGHT EXPERIMENT T025  
Final Report (Dudley Observatory) 206 p HC  
\$7.25 CSCL 03B

N75-25790

Unclas  
G3/90 26161

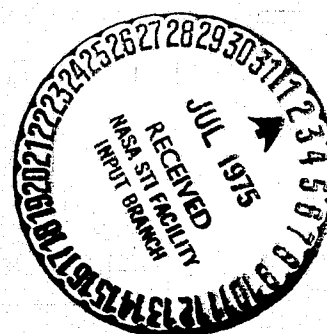


## Table of Contents

I	INTRODUCTION and SUMMARY . . . . .	01
II	PROJECT HISTORY. . . . .	05
	Topical History, Table of Topics . . . . .	10
III	TABLES OF SKYLAB OBSERVATIONS. . . . .	25
IV	COMET INVESTIGATION. . . . .	30
	Kohoutek Observations. . . . .	33
	Paper, Energy Source for Comet Outbursts . . . . .	34
V	ATMOSPHERIC REFRACTION . . . . .	36
	Paper, Stellar Refraction: A Tool to Monitor the Height of the Tropopause from Space . . . . .	37
VI	CORONAGRAPH-HORIZON STUDIES: THEORY, OBSERVATIONS, AND RESULTS. . . . .	57
	Paper, Comments on the Inversion of Horizon Measurements from Space . . . . .	58
	Paper, Atmospheric Aerosols: Results of a Solar Occultation Technique from Skylab . . . . .	90
VII	MICROWAVE LABORATORY . . . . .	123
	Facility Description . . . . .	124
	Paper, Scattering by Spheres with Nonisotropic Refractive Indices. . . . .	128
VIII	SUPPORTING LABORATORY TESTS. . . . .	160
	Table of Tests . . . . .	161

## I Introduction and Summary

The major purpose of the T025 coronagraph program as originally conceived in November 1971 was two-fold: to detect and investigate upper atmospheric aerosols and to monitor the particulate matter in the immediate vicinity of the spacecraft. A third objective - narrow band photography of Comet Kohoutek near perihelion passage - was added in April 1973 after the discovery of the comet. A series of mission mishaps, which included the loss of utilization of the solar airlock and the failure of an onboard camera (see Section II, Project History), necessitated a shift of emphasis within the program. The project was restructured to obtain the maximum scientific gain from the limited Skylab data of a few atmospheric photos. (A summary of all returned data, useful or otherwise, is presented in Section III). A broader theoretical approach was also adopted to extend and formalize the analysis of the atmosphere. Finally, the supporting mission efforts of ground based Kohoutek photography and the experimental investigation of light-scattering by non-ideal particles have been utilized to the fullest extent. The results of these efforts have led to a number of journal publications or papers which will be submitted presently. They comprise Sections IV through VII of this report and should be regarded as the major results of the T025 Skylab experiment. A short summary is presented below:

- 1) A model for comet outbursts (published in Nature) based on the properties of amorphous ice was developed in conjunction with another NASA program at the Dudley Observatory in an effort to understand new comets and predict probabilities of comet outburst (Section IV).



- 2) Ground based narrow-band and white light photography was conducted from a height of 3 km to supply proper exposure settings to the crew. This data has proven to be unique in that it represents the only narrow-band (emission) imagery of Comet Kohoutek this close (ten days) to perihelion. The analysis of this data is being undertaken as F. Giovane's Ph.D. thesis. An abstract of this nearly completed work is also presented in Section IV.
- 3) The effect of atmospheric refraction on the analysis of the T025 atmospheric data was investigated in detail. Although refraction effects proved to be negligible for this purpose, the study suggested that stellar refraction could be used from space as a possible tool to monitor the height of the tropopause. With little effort, the ideas were formalized and the resulting paper has been accepted for publication in the "Journal of Applied Meteorology". A preprint of the paper constitutes Section V.
- 4) Section VI of this report contains the theory, observations and results of the T025 atmospheric program. Two major papers make up this section. The first develops inversion techniques to extract the atmospheric parameters describing aerosols from the observations and shows the advantages of the coronagraph technique. Because the second paper, which will be presented at the May 29 - June 7, 1975, COSPAR meeting

4) continued -

in Bulgaria, represents the most significant return from the Skylab mission data, we present here the abstract from that article:

A simple coronagraph was modified for use aboard Skylab to photograph the earth's horizon just before spacecraft twilight as a device to monitor the aerosol component of the earth's atmosphere above the tropopause. This coronagraph technique allows one to investigate these high altitude aerosols from a uniquely favorable position - in the particles' forward-scattering cone. The method is thus 10 to 100 times more sensitive than daylight horizon scans made when the sun is well above the horizon. An eight month observing program using seven narrow-band filters was planned. Due to a multitude of spacecraft and equipment mishaps, including the loss of access to the solar-airlock, only one reducible photograph was obtained on a late November (1973) EVA. This particular picture was taken through a 250Å bandwidth filter centered on 3600Å. Since aerosol layering is detected as an enhancement of radiation above the Rayleigh background, this wavelength region, although free from the spectral influence of ozone, has a relatively high background level compared to longer wavelengths. Even at this high background level, the coronagraph picture provides evidence which is, if not conclusive of, at least consistent with, an aerosol layer peaking at  $48 \pm 1$  km. The region photographed was centered on 26°SE longitude, 63°OS latitude. This first observation at high southern latitudes suggests the global nature of the layer.

- 5) The microwave similitude laboratory is a facility in which the phenomenon of light-scattering by small particles is scaled to microwave wavelengths so that centimeter-size particles can be manufactured and shaped to represent their micron-size counterparts. As support for our Skylab program, this facility was relocated at the Dudley Observatory and upgraded to include angular scattering measurements as well as extinction. It now is unique in the world in its capabilities to measure back-scattering, forward-scattering ( $< 10^\circ$ ), and particle albedo. The facility description is

5) continued -

presented in Section VII along with the first draft of a paper applying ~~to~~ the microwave technique to the investigation of non-isotropic spheres.

In support of the accomplishments listed above, many hardware tests, film and instrument calibrations, and post-launch verifications were conducted in our Coronagraph and Optical Laboratory. Many of these supporting tests may be of interest to other investigators. The final Section, VIII, presents brief descriptions and results of those tests which we believe would be of a general interest. A table of contents is present at the beginning of the section.

## II PROJECT HISTORY

### Project History

Early in 1972 Dr. J. Mayo Greenberg became Principal Investigator of the existing Skylab T025 Coronagraph Experiment. The experiment had originally been designed to monitor the particulate contamination about the spacecraft. However, Dr. Greenberg not only proposed to study these particles in more detail, but he also intended to utilize the coronagraph to study the earth's atmospheric aerosol distribution. To implement this intention he formed a staff: Dr. D. Schuerman (in March 1972) was to act as project manager, and work on the theoretical and modeling problems; Mr. F. Giovane (in May 1972) was to be responsible for instrumentation, calibration, and photographic reduction; Dr. R. Wang (in January 1972) was to be in charge of the microwave scattering laboratory; and Mr. D. Hardy (in March 1972) was to act as project engineer and to be responsible for the experiment's documentation.

The modification of the coronagraph to achieve the proposed aims became the first goal of this staff. It was quickly realized that several modifications would be necessary. Principal among these were the addition of colored filters and the replacement of the Hassalbold camera by a 35 mm Nikon. The colored filters were added so that quantitative spectral information about light-scattering properties of the aerosols could be obtained. This would be impossible in the existing experiment's white light study. The addition of the Nikon camera had two effects: 1) it allowed direct viewing of the field by the astronauts by means of a penta-prism, and 2) it allowed the use of a UV lens (originally developed for the S063 experiment) which extended the observational range into the UV.

Once the modifications had been initiated, efforts were centered on the supervision of the contractor (MMC) in his implementation of these changes, and in the development of observational programs, instrument calibration, and eventually program reduction methods. Another major effort, instituted after final contract approval in October of 1972, was the construction of the Laboratory for Particle Scattering. This structure (completed shortly after the first Skylab launch) was to house the coronagraph test facility, optics laboratory, and the microwave similitude laboratory.

During this period and up to the launch of Skylab, an intensive effort was directed towards achieving an efficient reduction program for data that was to be returned. Unfortunately, most of this effort went for naught when the Skylab meteor shield was destroyed. The extension of the parasol from the solar airlock prevented the coronagraph from being deployed and invalidated our observational procedures and much of our data reduction methods. The next several months were spent in devising a way that would allow deployment of the coronagraph. An EVA method was devised, and the required hardware was developed for SL-3. However, the lack of time prevented the astronauts from being properly trained in T025 operations, and the coronagraph was not deployed on the 2nd mission. Nonetheless, the general success of SL-3 and our ability to develop an EVA program for the T025 allowed the coronagraph experiment to be included in the Skylab Kohoutek project.

The coronagraph, with its potential capability to observe the comet in emission near perihelion, was considered to be one of the most important

observing programs of the Kohoutek operation. Consequently, major modifications were made during the months prior to the SL-4 launch. The existing filters were supplemented by narrow-band interference filters centered on the emission features of Na, C<sub>2</sub>, CO<sup>+</sup>, CN, OH and adjacent continuum areas. A supporting bracket with precise pointing capability was constructed to mount the coronagraph to a structural strut of the ATM. A new occulting disk, with non-sharp edges and a sight filter, was readied. The crew was EVA trained for our experiment. The deadlines for SL-4 launch were met.

The first EVA atmospheric observing program (22 November 1973) was curtailed when the shutter speed extension knob, supplied by JSC, became unseated. As a result, the astronauts terminated observation after 6 exposures. The subsequent three EVA's (25 December 1973 comet pre-perihelion, 29 December 1973 comet post-perihelion, 03 February 1974 atmospheric aerosols) however, were conducted without apparent mishap, and 82 pictures of the comet and 40 pictures of the atmosphere were taken.

The development of the photographs did not take place until early March when it was tragically found that the results of the 2nd, 3rd, and 4th EVA's were out-of-focus. The out-of-focus situation, as we now have determined, resulted from the loss of the Nikon camera film pressure plate (that is, the springed plate that presses the film against the camera film platen, and thus keeps the film in a single plane of focus).

Several weeks were then spent in an intensive effort to learn whether the out-of-focus images could be refocused by existing image treat-

ment processes. The conclusion was that although refocusing could be achieved, the results and quality could not be guaranteed. Consequently, it was decided that it would not be worthwhile to attempt the defocusing of the out-of-focus frames immediately, and the entire effort was directed towards reducing the in-focus frames.

The in-focus frames were measured with the Spec - Scan 3000S Microdensitometer at Houston. In addition, microdensitometer records were also made of the out-of-focus frames to provide potential investigators interested in the defocusing problem with working data.

The analysis of the in-focus images was concurrent with an extensive theoretical study of the horizon scanning method. In addition, during this period, reduction of the comet data collected in Hawaii was undertaken as were some instrumental calibrations that had been scheduled for the year before but were previously postponed due to scheduling problems.

Based on the results obtained in June from the Spec - Scan 3000S and the concurrent completion of some of the instrument calibrations and theoretical studies, it was concluded that high quality of the 3600Å frame warranted an extensive analysis. The scanning results obtained for the 3600Å frame, however, indicated that the measurements with the Spec - Scan Microdensitometer were not as accurate as required. Consequently, the 3600Å frame was returned to Houston and remeasured in November 1974 on a refurbished 3000S. The resulting data was reduced successfully in the next four months.



Table of Contents of Topical History

Contractual . . . . .	11
Documentation . . . . .	12
Meetings Attended . . . . .	14
Flight Experimental Hardware. . . . .	15
Testing and Associated Hardware . . . . .	16
Test Facility . . . . .	17
Photographic Planning and Processing. . . . .	18
Crew Procedures and Mission Planning. . . . .	20
Comet Kohoutek. . . . .	21
T025 EVA and Related Activities . . . . .	22
T025 Flight Execution . . . . .	23
Data Evaluation, Reduction and Analysis . . . . .	24

Contractual

- a) Dudley involvement 1/72
- b) Extension Submitted 6/72
  - 1) Budget revision and effects 7/72
  - 2) Extension approved 10/72
- c) Kohoutek Modification
  - 1) Additional funding approved 10/73
- d) ECP's
  - 1) 001, 002, 003 approved 8/73
- e) Authorization to reduce S052 data received 11/74

## Documentation

### a) EIS, ERD

- 1) Update 4/72
- 2) Update 5/72 (due to  $\Delta$ CDR)

### b) MRD

- 1) Update 4/72
- 2) Input/update 5/72 (review copy)
- 3) Revised to be compatible with EOH 9/72
- 4) SL-2, SL-3 update 3/73
- 5) SL-4 update to reflect Kohoutek modifications 8-11/73

### c) DRF

- 1) Initial specifications 5/72
- 2) Package submitted 6/72
- 3) Approved 8/72
- 4) Weather data DRF drafted 11/72
- 5) Data and forecast requirements submitted 12/72
- 6) Return of Kohoutek filters submitted 12/73
- 7) Flight film 7/74

### d) EOH

- 1) Procedures defined for SL-2 6/72
- 2) Procedures incorporated 7/72

### e) Check List

- 1) Operational procedures incorporated 7/72
- 2) Revised/refined 10/72
- 3) SL-3, 4 update 11/72
- 4) SL-2, SL-3 update 3/73
- 5) SL-4 update to reflect Kohoutek modifications 8-11/73

### f) Mission Rules

- 1) Emergency procedures defined 7/72

### g) Update Message Pad

- 1) Revised 7/72
- 2) Revised 9/72 (to reflect f/stop and start/stop times)
- 3) Revised/refined 10/72

Documentation - continued

h) Design Certification Review 8/72

i) RIDS

1) Issued at  $\Delta$  CARR 8/72

Meetings Attended

a) SALWG

- 1) First 6/72
- 2) Second 7/72 - coordination of data
- 3) Third 10/72
- 4) Fourth 11/72
- 5) Fifth 4/73
- 6) Sixth 6/73

b) Atmospheric Studies Meeting

- 1) 6/72

c) Crew debriefings (pre-flight)

- 1) With SL-2 crew 1/73
- 2) With SL-3 crew 4/73

d) Comet Conferences

- 1) Baltimore 6/73
- 2) GSFC 7/73
- 3) GSFC 8/73
- 4) Houston 9/73
- 5) Albuquerque 10/73

e) Crew Debriefing (post-flight)

- 1) With SL-4 crew 3/74

f) Simulations Attended

- 1) Paper simulation 5/72
- 2) First simulation 1/73
- 3) Second simulation 2/73
- 4) Third simulation 4/73

### Flight Experiment Hardware

- a) Initial design modifications 3/72
  - 1) Coronagraph baffle
  - 2) Camera, filters, adapters
- b) Fit and Function Test 4/72
  - 1) Nikon camera with filter holders
- c) Hardware specifications for baffle, filters, holders, and light tightness 5/72 (at  $\Delta$ CDR)
- d) Numbers on Nikon view grid
  - 1) Possible problem for readability 5/72
  - 2) Test prove numbers legible 6/72
- e) Neutral density filter
  - 1) Specifications made 5/72 (at  $\Delta$ CDR)
  - 2) Multiple imaging effect detected 8/72
  - 3) Photographs through filters requested by MMC 9/72
- f) Filters (first set)
  - 1) Specifications made 6/72
  - 2) Corion unable to comply and specifications relaxed 7/72
  - 3) Pinholes found but would not significantly affect results 8/72
  - 4) P.I. filters received with modification kit 10/72
- g)  $\Delta$  CARR, equipment acceptable except for a few RIDS which were subsequently corrected 8/72
- h) Instrument realignment
  - 1) Test and Checkout Procedure at KSC prove gross misalignment of T025 2/73
  - 2) Experiment realigned and reticle grid secured 3/73
- i) 2450A filter found defective 3/73
  - 1) Flight Filter replaced 3/73

## Testing and Associated Hardware

- a) Tests at the Coronagraph Test Facility, HAO, Boulder, Colorado  
3/72 and 5/72
  - 1) Size limitation for visibility determined
  - 2) Rejection ratio determined
  - 3) Baffle design finalized
  - 4) Interior spacecraft lighting determined
  - 5) Film selection narrowed
  - 6) Particle density counts calibrated
  - 7) Input to design of Laboratory for Particle Scattering
- b) HAO type visible sensitometer
  - 1) Construction initiated 7/72
  - 2) Construction completed 11/72
- c) Revised OWS lighting arrangement specified 7/72
- d) SAL mock-up received for testing 8/72
- e) UV sensitometer
  - 1) Constructed and operational 3/73
- f) Isodensitometer
  - 1) Calibration studies initiated 9/72
  - 2) Digital recording system rectified 11/72
  - 3) Decoding of tape readout completed 12/72
  - 4) Digital recording system refurbished 6/74

### Test Facility

- a) Initial design of equipment requirements 5/72
- b) Test tunnel and isodensitometer received 6/72
  - 1) Test tunnel outfitted
  - 2) Isodensitometer refurbished
- c) Temporary Coronagraph Test Facility
  - 1) Outfitted 7/72
  - 2) Completed 8/72
  - 3) Calibration testing begun 9/72
- d) Laboratory for Particle Scattering
  - 1) Detailed planning completed 10/72
  - 2) Foundation begun 11/72
  - 3) Foundation completed 12/72
  - 4) Frame completed 2/73
  - 5) Interior begun 3/73
  - 6) Interior completed 4/73
  - 7) Construction completed 7/73
- e) Microwave Scattering Laboratory
  - 1) Operational 9/73



## Photographic Planning and Processing

- a) HAO testing for reduction of film choices 5/72
- b) Film type discussions
  - 1) With PTD 7/72
  - 2) With PTD 8/72
- c) Film loading and handling procedures
  - 1) With J. Ragan (JSC) 7/72
- d) Film Calibration
  - 1) Discussions with J. Ragan 7/72
  - 2) Discussions with Laman and Thompson 7/72
  - 3) Procedures established 11/72
  - 4) Details of calibration roll established 3/73
- e) Film Tests
  - 1) UV sensitivity of various films 7/72
  - 2) IIAO tests (UV sensitive) 8/72
  - 3) Final film selection tests by PTD 10/72
  - 4) 2485 tests, resolution loss 4/73
- f) Film Selection
  - 1) 2403, 2485, S0168 selected 11/72
- g) Optimum Development Times
  - 1) Tests on 2403 3/73
- h) Resolution Testing
  - 1) Using flight type lenses 1/73
  - 2) With P.I. filters 2/73
  - 3) With flight filters 1/73
- i) Absolute Calibration
  - 1) With flight filters at MMC 1/73
- j) Light Piping - subdued light required for film loading 4/73

Photographic Planning and Processing - continued

k) Kohoutek Film

- 1) Additional cassettes requested and approved 10/73
- 2) Pre-flight calibration by PTD at JSC 10/73

l) SL-4 Flight Film Processing

- 1) PTD could not achieve  $\gamma = 1$  with existing processing plan - further testing required 12/73
- 2) Final photographic plan adopted 1/74
- 3) Directed and monitored flight film processing 2-3/74

m) Flight Film - originals and duplicates

- 1) Complete set of second gen. neg. delivered 3/74
- 2) Originals requested per DRF 7/74
- 3) Originals received 8/74

n) Hypersensitization

- 1) Possibility due to exposure to vacuum ruled out 8/74

## Crew Procedures and Mission Planning

- a) Capability developed to calculate orbital data, start/stop times, latitude/longitude 8/72
  - 1) Programs developed 9/72
- b) Weather data acquisition planning 8/72
  - 1) Programs developed 9/72
  - 2) Meeting with Nat. Meteor. Center to arrange acquisition of meteorological data (post flight) 11/72 3/73
  - 3) Data from Air Lines coordinated 3/73
- c) Operation Pointing Problems
  - 1) Attitude hold requirement 3/73
  - 2) T025-ATM alignment 3/73
  - 3) Discussions with H-BAR/sun sensor acquisition 4/73
  - 4) Fit check with S020 "wedge" 4/73
- d) Crew Training Exercise
  - 1) Huntsville 9/73 (2 times)
  - 2) Houston 9/73
  - 3) Huntsville 10/73 (2 times)

Comet Kohoutek

- a) Observing program being planned 4/73
- b) Proposal submitted 7/73
- c) Hardware requirements defined
  - 1) JSC, MMC, MDAC, DO meeting to discuss modifications 7/73
- d) Possible modes of deployment
  - 1) Out of - Z airlock with 180° roll 7/73
  - 2) EVA 8/73
- e) Filters, interference
  - 1) Determination of 15 required 8/73
  - 2) Orders placed 8/73
  - 3) Filters accepted 10/73
  - 4) CARR for filters 10/73
  - 5) Hand carried to KSC 10/73
  - 6) DRF submitted for filter return 12/73
- f) Filter, occulting disk
  - 1) Designed
  - 2) Modifications to back-up occulting disk made at MMC 8/73
  - 3) Testing and fabrication begun 9/73
  - 4) Thermal vacuum tests (and transmission tests) at D.O. 9/73
  - 5) Qual tests at MMC
  - 6) Training filter shipped to JSC 9/73
  - 7) Flight filter hand-carried to KSC 10/73
- g) Ground Based Observations
  - 1) At Hawaii to determine proper exposure times 11/73 - 1/74

## T025 EVA and Related Activities

### a) Meteoroid Shield Loss

- 1) Assessment of thermal damage 6/73

### b) EVA Plans

- 1) Initial plans discussed at MSFC 6/73
- 2) Conceptual ideas for bracket 6/73
- 3) Zero-g simulation at MSFC 6/73
- 4) Modifications of T025 for EVA 6/73
  - A) occulting disk safety cover
  - B) camera body thermal jacket
  - C) cable release and extension knob
  - D) occulting disk edge dulling
- 5) PDR of modifications 8/73
- 6) CDR of modifications 9/73
- 7) CARR of modifications 9/73

### T025 Flight Execution

- a) First EVA, (November 22, 1973; Astronaut Pogue)
  - 1) Preparation 11/73
  - 2) Operation, with camera failure 11/73
- b) Joint effort with S063
  - 1) Arrangements and goals 11/73
  - 2) Nine (9) sequences taken 12/73
  - 3) Additional sequences taken 1/74
- c) Kohoutek EVA's, December 25 and 29, 1973; Astronauts Pogue and Gibson)
  - 1) Both EVA's (25th and 29th) apparently successfully completed 12/73
- d) Operational Flight Hardware Problems
  - 1) First EVA problem diagnosed 11/73 12/73
- e) Second Atmosphere EVA (February 3, 1974; Astronaut Gibson)
  - 1) Approved by CCB for early February 12/73
  - 2) Preparation and operation 2/74

## Data Evaluation, Reduction and Analysis

### a) Initial Data Evaluation

- 1) All but 6 frames out-of-focus 3/74
- 2) Tests conducted to determine cause 3/74
- 3) Effects of out-of-focus condition 3/74
- 4) Initial data on 6 good frames 3/74

### b) Image Restoration (JPL)

- 1) Assessed as a possibility 3/74
- 2) Meeting to determine quality and cost 6/74
- 3) Decided not to pursue at this time 8/74

### c) Data Reduction of EVA-1

- 1) Planned and outlined 3/74
- 2) Approach to reduction plan 4/74
- 3) Plan for Kohoutek film 4/74
- 4) Possible reduction of contamination data 4/74
- 5) Plate scale determined 6/74 8/74
- 6) Vignetting function determined 6/74 8/74
- 7) Deterioration of 2530Å filter 6/74
- 8) Not satisfied with Houston digitized data 7/74
- 9) Tests require use of electric Nikon for simulation 7/74
- 10) Electric Nikon can be shimmed to simulate flight data 8/74
- 11) Reciprocity tests 8/74
- 12) Spectral absolute calibration of flight film 8/74
- 13) Measurements of flight originals on Houston desitometer 8/74 1/75

### d) Comet Observations

- 1) Reduction(with calibration plate scale vignetting) 6 - 7/74
- 2) All white light photos reduced to integrated energies 8/74
- 3) Corrected to zero air mass
- 4) Narrow band photos reduced

### III TABLES OF SKYLAB OBSERVATIONS



# T025 Photographic Log

22 November 1974      Film #BE03      Nikon Camera NK01

Nikon 27 mm UV lens at f/2.0

<u>Frame</u>	<u>Filter</u>	<u>Shutter Speed (sec)</u>	<u>Comments</u>
1	Blank	1/1000	Atmosphere in-focus
2	Blank	1/30	"
3	2530	4	"
4	2530	1	"
5	3600	1/15	"
6	3600	unrecorded	"

Termination due to camera malfunction. Frames 7 - 40 were not taken due to shutter-speed extention knob not being seated properly on camera.

## Notes:

Frames 1 & 2 - made for purposes of precisely locating sun's image behind occulting disk. Background level high as expected. Sun's location well determined.

Frames 3 & 4 - 2530 filter shown to have deteriorated in flight. Frames show ozone layering but not of sufficient quality to warrant quantitative analysis.

Frame 5 - good quality, no problems with light scattering in filter. Exposure time selection perfect.

Frame 6 - good quality, no crew record of exposure or time when taken.

25 December 1973 Film #BE04 Nikon Camera NK02

Nikon 27 mm UV Lens at f/2.0

<u>Frame</u>	<u>Filter</u>	<u>Shutter Speed (sec)</u>	<u>Comments</u>
1	Blank	1/125	Comet, out-of-focus
2	Blank	1/125	"
3	Blank	1/1000	"
4	2530	80	"
5	2530	10	"
6	3600	1/2	"
7	3600	1/15	"
8	3361	14	"
9	3361	2	"
10	3873	14	"
11	3873	2	"
12	3873	1/4	"
13	4700	2	"
14	4700	1/4	"
15	3100	14	"
16	3100	2	"
17	3100	1/4	"
18	6000	1/30	"
19	6000	1/250	"
20	6000	1/1000	"
21	3250	14	"
22	3250	2	"
23	3250	1/4	"
24	2800	7	"
25	2800	1	"
26	4430	2	"
27	4430	1/4	"
28	5500	1/2	"
29	5500	1/15	"
30	4262	7	"
31	4262	1	"
32	3940	14	"
33	3940	2	"
34	3940	1/4	"
35	4900	2	"
36	4900	1/4	"
37	5890	4	"
38	5890	1/2	"
39	3873	14	"
40	3873	2	"
41	3873	1/4	"

Normal termination of sequence.

29 December 1973      Film #BE05      Nikon Camera   NK02

Nikon 27 mm   UV Lens at f/2.0

<u>Frame</u>	<u>Filter</u>	<u>Shutter Speed (sec)</u>	<u>Comments</u>
1	Blank	1/125	Comet, out-of-focus
2	Blank	1/1000	"
3	2530	80	"
4	2530	10	"
5	3600	1/2	"
6	3600	1/15	"
7	3361	14	"
8	3361	2	"
9	3873	14	"
10	3873	2	"
11	3873	1/4	"
12	4700	2	"
13	4700	1/4	"
14	3100	14	"
15	3100	2	"
16	3100	1/4	"
17	6000	1/30	"
18	6000	1/250	"
19	6000	1/1000	"
20	3250	14	"
21	3250	2	"
22	3250	1/4	"
23	2800	7	"
24	2800	1	"
25	4430	1	"
26	4430	2	"
27	4430	1/4	"
28	5500	1/2	"
29	5500	1/15	"
30	4262	7	"
31	4262	1	"
32	3940	14	"
33	3940	2	"
34	3940	1/4	"
35	4900	1/4	"
36	4900	2	"
37	5890	4	"
38	5890	1/2	"
39	3873	14	"
40	3873	2	"
41	3873	1/4	"

Normal termination of sequence.

03 February 1974      Film #BE16      Nikon Camera   NK02

Nikon 27 mm   UV Lens at f/2.0

<u>Frame</u>	<u>Filter</u>	<u>Shutter Speed (sec)</u>	<u>Comments</u>
1	Blank	1/1000	Atmosphere, out-of-focus
2	Blank	1/30	"
3	2530	4	"
4	2530	1	"
5	3600	1/15	"
6	3600	1/500	"
7	3250	1/30	"
8	3250	1	"
9	2800	1	"
10	2800	1/15	"
11	4430	1/4	"
12	4430	1/250	"
13	5500	1/250	"
14	5500	1/4	"
15	Blank	1/1000	"
16	2530	4	"
17	2530	1	"
18	3600	1/15	"
19	3600	1/500	"
20	3250	1/30	"
21	3250	1	"
22	2800	1	"
23	2800	1/15	"
24	4430	1/4	"
25	4430	1/250	"
26	5500	1/250	"
27	5500	1/4	"
28	2530	4	"
29	2530	1	"
30	3600	1/15	"
31	3600	1/500	"
32	Blank	1/1000	"
33	3250	1/30	"
34	3250	1	"
35	2800	1	"
36	2800	1/15	"
37	4430	1/4	"
38	4430	1/250	"
39	5500	1/250	"
40	5500	1/4	"

Normal termination of sequence.

#### IV COMET INVESTIGATION

### Comet Investigation

The intended aim of the T025 Kohoutek mission was to make narrow-band emission photographs of the comet in OH, CN, CO<sup>+</sup>, C<sub>2</sub> and Na. These observations, if they had been successful, would have allowed for the first time a series of photographs in emission bands and lines to be made of a comet when it is subjected to intensive radiative and gravitational forces associated with perihelion passage. The morphology of the comet in emission gained from these photographs would have proved extremely valuable in providing parent-daughter molecule relationships. Consequently, the failure of these observations, due to the out-of-focus Nikon camera, were extremely unfortunate.

Although the comet observations from Skylab were unsuccessful, several hundred exposures were made from an observing site at 3000 m on Haleakala, Maui, Hawaii to support the Kohoutek operation on Skylab. Photographs were taken with the T025 filters and both the 27 mm f/2.0 UV lens and the 46 mm f/1.2 lens to obtain exposures for the S063 and T025 experiments. Mr. Giovane decided, after it was learned that the Skylab data did not contain worthwhile comet data, to reduce the Haleakala photographs for his Ph.D. thesis. The photographs were taken under extremely poor photometric conditions, with the optical path occasionally exceeding 40 air masses, as the comet was photographed near to or below the geographic horizon. Because of the difficulty and time consuming nature of the analysis, the reduction was limited to just a few of the hundreds of frames available.

This reduction was developed in two parts. The first part involved the reduction of 15 frames taken on nights between 06 and 19 December, using the 46 mm lens and no filters. These photographs were originally taken as position orientation frames for the narrow-band photographs. However, it was thought their reduction would provide invaluable experience and information needed for the narrow-band reduction. The results, now nearly complete, provide a morphologic picture of the comet just before perihelion and also yield the magnitude determined in absolute units (that is  $\text{ergs/cm}^2\text{-sec}$ ). It is expected that these results will be submitted for publication in the very near future.

The second part of the reduction involves 14 narrow-band photographs taken of the emission spectra of the comet in Na 5890, Cn 3770, and C<sub>2</sub> 4700. These photographs show a steady brightening of the comet in each of these emission lines, with Na 5890 becoming very strong as perihelion approached. They also provide the first morphologic history of a comet along with absolute magnitude close to perihelion. The results will be submitted for publication soon.

A list of the recorded observations is presented in Table 1.

In addition, while preparing for the Kohoutek mission, D. Schuerman began a literature search on comets. Reflections on the nature of comet outbursts prompted a joint study with other groups connected with the observatory. The results of that study have been published in Nature, and a reprint is presented at the end of this section.

Table of Comet Observations

White Light

<u>Date</u>	<u>No. Frames Reduced</u>
06 Dec	2
07 Dec	2
13 Dec	1
14 Dec	2
16 Dec	3
17 Dec	2
18 Dec	1
19 Dec	1

Narrow Band Emission

	<u>Date</u>	<u>Time (GMT)</u>
<u>C<sub>2</sub></u>	14 Dec	15 <sup>h</sup> 45 <sup>m</sup>
	16 Dec	15 <sup>h</sup> 42 <sup>m</sup>
	17 Dec	15 <sup>h</sup> 46 <sup>m</sup>
<u>Continuum C<sub>2</sub></u>	16 Dec	15 <sup>h</sup> 32 <sup>m</sup>
<u>Na</u>	16 Dec	15 <sup>h</sup> 23 <sup>m</sup>
	17 Dec	15 <sup>h</sup> 30 <sup>m</sup>
	18 Dec	15 <sup>h</sup> 47 <sup>m</sup>
	19 Dec	15 <sup>h</sup> 56 <sup>m</sup>
<u>CN</u>	14 Dec	15 <sup>h</sup> 30 <sup>m</sup>
	15 Dec	15 <sup>h</sup> 45 <sup>m</sup>
	17 Dec	15 <sup>h</sup> 46 <sup>m</sup>
	18 Dec	15 <sup>h</sup> 54 <sup>m</sup>
	19 Dec	15 <sup>h</sup> 56 <sup>m</sup>



## Energy source for comet outbursts

A COMET nucleus is generally recognised as an icy conglomerate, as was originally proposed by Whipple<sup>1</sup>. The Orbiting Astronomical Observatory observations of Comet Tago-Sato-Kosaka<sup>2</sup> and Comet Bennett<sup>3</sup> support the current ideas that H<sub>2</sub>O is a major component of comets. If comets were indeed formed through an accretion mechanism at distances of many AU from the Sun, what is the nature of the resulting form of water ice?

A number of studies on the deposition of water vapour at low pressures and temperatures indicate that amorphous ice is formed. The reported physical properties include: a density of 2.3 g cm<sup>-3</sup> (ref. 4), a specific heat 25% greater than that of ordinary hexagonal ice, and a latent heat for the phase transition from amorphous to cubic ice of  $24 \pm 2$  cal g<sup>-1</sup> (ref. 5). The transition occurs at a temperature near 140 K (ref. 6). The presence of impurities seems to enhance the growth of clathrate hydrate ices, but both the clathrates and the amorphous water ice can apparently coexist at densities of 1.4–1.7 g cm<sup>-3</sup> (ref. 4). Clathrate compounds have densities which are typically 0.3–0.5 g cm<sup>-3</sup> (ref. 7).

Observational evidence indicates that comet outbursts require an internal energy source<sup>8</sup>. If at least the surface of a comet nucleus contains a substantial percentage of amorphous ice, then the phase transition of the amorphous ice to a cubic structure provides a release of energy which may be responsible for the outbursts observed in many comets. In addition, if the density of amorphous ice is indeed about 2 g cm<sup>-3</sup>, then a 'pulverising' mechanism would exist because of the abrupt stresses introduced by the volume change in the solid as the density of the ice changes by a factor of two.

The total energy released during a cometary outburst is of the order of 10<sup>21</sup> erg with an accompanying mass loss of 10<sup>12</sup> g (ref. 8). The resulting energy requirement of 10<sup>9</sup> erg g<sup>-1</sup> compares favourably with the 10<sup>9</sup> erg g<sup>-1</sup> released during the amorphous–cubic phase change.

Any theory to explain cometary outbursts must consider the spatial distribution of the phenomenon. Figure 1 reports the results of a study in which the positions of the comets are shown at the time of outburst<sup>9</sup>. Although some observational selection effects may be present, a definite clustering is apparent within 2.5 AU from the Sun. Calculations<sup>10</sup> have shown that celestial bodies consisting of water ice with an albedo of 0.6, at a distance of 2.5 AU from the Sun, have expected surface temperatures ranging from 150 K for a rapidly rotating sphere, to 180 K for a non-rotating sphere (see Figs 1 and 2 of ref. 10). The phase transition from amorphous to cubic ice requires a temperature near 140 K. Higher temperatures are necessary if the surface has an insulating layer such as that predicted in the model we shall present here.

Any volume element which undergoes this phase transition increases its temperature by about 45 K. Therefore, the heat released can trigger the surrounding material so that the phase change is, in effect, a self feeding mechanism which propagates to a distance where the local temperature is near 100 K.

The outburst of a comet can therefore be envisaged as occurring in a series of consecutive steps: initiation, propagation, pulverisation, sublimation, ejection, and insulation.

Depending upon the condition of the surface of the comet, the amorphous–cubic ice phase transition can be achieved at different solar distances. If the surface is amorphous ice, an outburst is most probable at about 2.5 AU from the Sun. If the surface is covered with an insulating layer, however, a closer approach to the Sun is required. On the other hand, if amorphous ice is in heat exchange with material with a temperature which increases faster than that of the ice, then an outburst can be expected at greater distances. If the temperature

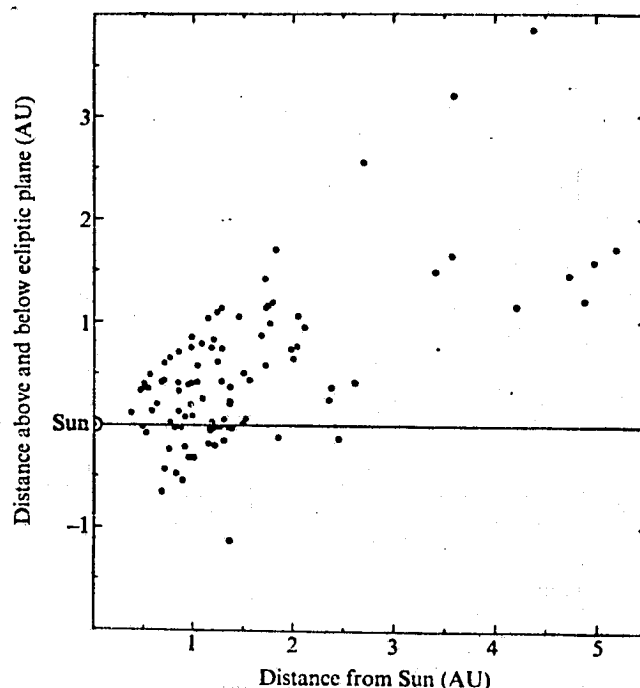


Fig. 1 Positions of comets at the time of outbursts. ○, Hypothetical outbursts preceding discovery; ●, observed outbursts after discovery<sup>9</sup>. (Courtesy of the IAU.)

of the ice is slightly below the transition temperature, thermal spikes provided by solar activity could trigger the outburst.

Once the phase transition has been initiated, it will propagate within a region where the temperature of the ice is greater than 100 K. The volume into which the transition can propagate can be estimated. Our calculations consider a spherical comet with a radius of 5 km. For a rough estimate we assume that the surface temperature around the subsolar point decreases as a cosine function. For a subsolar temperature of 140 K, the surface area with a temperature above 100 K is bounded by a circle and contains 14% of the total surface area of the comet. Following Sommerfeld's<sup>11</sup> development, it is possible to estimate the depth at which the phase transition terminates 1 m below the subsolar point. For this calculation the thermal diffusivity of glass,  $2 \times 10^{-2}$  cm<sup>2</sup> s<sup>-1</sup>, is used. As this depth is reduced to zero at the perimeter of the previously computed area, an average depth of 50 cm is assumed. The resulting volume which undergoes the phase transition is  $2.2 \times 10^{13}$  cm<sup>3</sup>. The density of amorphous ice is about 2 g cm<sup>-3</sup> and so the mass involved is  $5 \times 10^{13}$  g.

The transformation of amorphous ice into cubic ice with a density of 0.94 g cm<sup>-3</sup>, must induce severe strains of the order of 20–30% which will pulverise the ice. It is useful to estimate the particle size which results from the fracturing process. For a stress,  $S$ , of about 10<sup>4</sup> pound inch<sup>-2</sup>,  $W$  is proportional to  $S^{-1}$ , where  $W$  is the average mass of the ten largest particles that result when the stressed material fractures. If this relationship holds in general for higher stresses, then an extrapolation to the anticipated stress encountered for the amorphous–cubic ice transformation ( $\sim 10^5$  pound inch<sup>-2</sup> for strains of 20–30%), shows that  $W$  is of the order of  $4 \times 10^{-9}$  g. This implies that the largest particle has a size of about 10  $\mu$ m.

This mechanism therefore automatically provides a source of particulate matter which creates a huge surface area. Consequently, the equilibrium vapour pressure between the particulates will be rapidly established. With the mass ( $5 \times 10^{13}$  g)

involved in the phase transition the energy,  $E$ , which is released, is given by:

$$E = 5 \times 10^{13} \text{ g} \times 24 \text{ calorie g}^{-1} \\ = 10^{15} \text{ calorie}$$

This can generate water vapour of mass,  $M$ :

$$M = E/H = 10^{15} \text{ calorie}/650 \text{ calorie g}^{-1} \\ = 1.5 \times 10^{12} \text{ g}$$

where  $H$  is the heat of sublimation. This means that 3% of the generated particulate matter is sublimated. This gas must certainly expand into the vacuum of space at a few times the velocity of sound, carrying with it, at least to an order of magnitude, a comparable mass of dust. This mass is consistent with observed values for typical comet outbursts<sup>6</sup>.

A large fraction of the fractured material remains on the surface. This effectively creates an insulating layer with a high albedo which tends to prevent further outbursts for some time.

This picture of comet outbursts can be subjected to many refinements, such as variations of comet sizes, or of rotation rates and inclinations, impurities and inhomogeneities in the ice, and orbital parameters. The general features of this theory are, however, consistent with observations and in our opinion provide for a more plausible source of energy than has been previously suggested. Those suggestions have included the vaporisation of pockets of methane and/or carbon dioxide<sup>6</sup>, explosive radical reactions<sup>12</sup>, and collisions with interplanetary boulders.

We thank Dr C. L. Hemenway of the Dudley Observatory, New York for discussions and Drs W. T. Brydges and T. R.

Kozlowski of the Corning Glass Works, Corning, New York for providing the glass shattering data. We also acknowledge support from NASA.

HARVEY PATASHNICK

Dudley Observatory,  
Albany, New York 12205

GEORG RUPPRECHT

Bendix Corporation,  
Denver, Colorado 80236

DONALD W. SCHUERMAN

Dudley Observatory

Received March 4; revised May 7, 1974.

- <sup>1</sup> Whipple, F. L., *Astrophys. J.*, **111**, 375 (1950).
- <sup>2</sup> Jenkins, E. B., and Wingert, D. W., *Astrophys. J.*, **174**, 697 (1972).
- <sup>3</sup> Code, A. D., Houck, T. E., and Lillie, C. F., *The Scientific Results from the Orbiting Astronomical Observatory (OAO-2)*, NASA SP-310, 109 (1972).
- <sup>4</sup> Delsemme, A. H., and Wenger, A., *Science*, **167**, 44 (1970).
- <sup>5</sup> Ghormley, F. A., *J. chem. Phys.*, **46**, 1321 (1966).
- <sup>6</sup> McMillan, F. A., and Los, S. C., *Nature*, **206**, 806 (1965).
- <sup>7</sup> Delsemme, A. H., and Wenger, A., *Planet. Space Sci.*, **18**, 709 (1970).
- <sup>8</sup> Whitney, C., *Astrophys. J.*, **122**, 190 (1955).
- <sup>9</sup> Pittich, E. M., *Splitting and Sudden Outbursts of Comets as Indicators of Nongravitational Effects*, (Forty-fifth IAU Symposium, Leningrad, 1970), 283 (Reidel, Dordrecht, 1972).
- <sup>10</sup> Watson, K., Murray, B. C., and Brown, H., *Icarus*, **1**, 317 (1963).
- <sup>11</sup> Sommerfeld, A., *Partial Differential Equations*, 68 (Academic Press, New York, 1949).
- <sup>12</sup> Donn, B., and Urey, H. C., *Astrophys. J.*, **123**, 339 (1956).

## V ATMOSPHERIC REFRACTION

**STELLAR REFRACTION: A TOOL TO MONITOR THE  
HEIGHT OF THE TROPOPAUSE FROM SPACE\***

**Donald W. Schuerman, Frank Giovane, and J. Mayo Greenberg**

**Dudley Observatory**

**and**

**The State University of New York at Albany**

**Albany, New York**

**Revised: \_\_\_\_\_**

**\* Accepted for future publication in the  
"Journal of Applied Meteorology"**

## Abstract

Calculations of stellar refraction for a setting or rising star as viewed from a spacecraft show that the tropopause is a discernable feature in a plot of refraction vs. time. The height of the tropopause is easily obtained from such a plot. Since the refraction suffered by the starlight appears to be measurable with some precision from orbital altitudes, we suggest this technique as a method for remotely monitoring the height of the tropopause. Although limited to night-time measurements, the method is independent of supporting data or model fitting and easily lends itself to on-line data reduction.

## 1. Introduction

If one observes the setting or rising of a star from above the earth's atmosphere, the apparent zenith angle of the star at any given moment is determined by the refraction suffered by the starlight passing through the atmosphere. The calculation of this effect is given in the next section. Since the index of refraction is essentially a function of the density, such calculations depend upon the specific structure of the atmosphere. We have found that each of three seasonal changes in representative density profiles produces a measurable signature on the apparent trajectory of a star. The effect of the tropopause is a clearly identifiable feature of the trajectory for each of the models we have chosen. This suggests that from orbital altitudes this technique could be used to globally monitor the height of the tropopause independently of other supporting data. In this paper, the tropopause is defined by vertical changes in the lapse rate of temperature as opposed to a more generalized criterion such as that given by Danielsen (1968).

## 2. Calculation of Refraction

Following Fesenkov (1959), the path of a light ray through the atmosphere may be described in polar coordinates  $(r, \phi)$  by

$$K = \text{constant} = n(r) r \sin \zeta \quad (1)$$

and

$$\frac{dr}{r d\phi} = \cot \zeta \quad (2)$$

where  $\zeta$  is the angle formed between the ray of light and the radius vector  $\underline{r}$  (see Fig. 1) and  $n(r)$  is the index of refraction. The angle of refraction  $R$  for a stellar observer at  $P$  is given by

$$R = \zeta + \phi - 90^\circ. \quad (3)$$

For an observer at point  $Q$  looking along the light path whose closest approach to the earth  $h$  occurs at point  $P$ , the difference between the zenith angle  $Z$  of a star and its observed zenith angle  $Z_{OB}$  is evidently

$$Z - Z_{OB} = 2R(h) \quad (4)$$

where

$$Z_{OB} = 180^\circ - \zeta. \quad (5)$$

For any given tangent height  $h$ , one may calculate  $R$  from (3) by integrating Eqs. (1) and (2). The constant in (1) is evaluated

for each tangent height at P where  $\zeta = 90^\circ$  so that

$$K = (E+h)n(h), \quad (6)$$

E being the radius of the earth. In subsequent numerical calculations we set  $E = 6370$  km.

The final ingredient necessary for the calculation is the specification of the index of refraction as a function of height. We assume here that  $R$  is a linear function of density,  $n(h) = 1 + c(\lambda)\rho(h)$  where  $c(\lambda)$  is slightly dependent on wavelength as given by Allen (1963). In this approximation we find that  $n-1$  is accurate to  $\frac{1}{2}\%$  when compared to the more exact expression given by Allen.

We have found the following technique of integration to be somewhat more convenient than that given by Fesenkov. In integrating Eqs. (1) and (2) from  $r_1$  to  $r_2$ , let  $x = n_1 r/K$ . Furthermore, we assume the logarithm of the density within the atmosphere varies linearly from  $r_1$  to  $r_2$  so that

$$n = 1 + (n_1 - 1)e^{-y}, \quad n_2 \leq n \leq n_1 \quad (7)$$

where  $n_1$  is the index of refraction at  $r_1$ ,  $y = (x_2 - x_1)/x_H$ , and  $x_H$  is related to the density scale height  $H$  by

$$x_H = \frac{n_1 H}{K} = \frac{n_1}{K} \frac{(r_2 - r_1)}{\ln(\rho_1/\rho_2)} \quad (8)$$



Eqs. (1) and (2) are then combined to yield

$$\phi_2 - \phi_1 = \int_{x_1}^{x_2} \frac{dx}{x \left[ x^2 \left\{ 1 + \left( \frac{n_1 - 1}{n_1} \right) (e^{-y} - 1) \right\}^2 - 1 \right]^{\frac{1}{2}}} \quad (9)$$

To first order accuracy in  $(n_1 - 1)/n_1$  and to second order accuracy in  $y$ , (9) may be integrated to obtain

$$\begin{aligned} \phi_2 - \phi_1 = & \cos^{-1} \left( \frac{1}{x_2} \right) - \cos^{-1} \left( \frac{1}{x_1} \right) + \left( \frac{n_1 - 1}{n_1} \right) \frac{1}{x_H} \left[ \ln \left\{ \frac{x_2 + (x_2^2 - 1)^{\frac{1}{2}}}{x_1 + (x_1^2 - 1)^{\frac{1}{2}}} \right\} - \frac{(x_2 - x_1)}{(x_2^2 - 1)^{\frac{1}{2}}} \right] \\ & + \left( \frac{n_1 - 1}{n_1} \right) \left( \frac{1}{x_H} \right)^2 \left[ \frac{(x_2 - x_1)^2}{2(x_2^2 - 1)^{\frac{1}{2}}} - (x_2^2 - 1)^{\frac{1}{2}} + (x_1^2 - 1)^{\frac{1}{2}} + x_1 \ln \left\{ \frac{x_2 + (x_2^2 - 1)^{\frac{1}{2}}}{x_1 + (x_1^2 - 1)^{\frac{1}{2}}} \right\} \right] \quad (10) \end{aligned}$$

For a given density profile, we start the integration at some tangent height  $h$ , setting  $r = (E + h)$ . Because of the restriction leading to (9) that  $y$  be small, we have selected  $\Delta r$  to be one kilometer so that  $y \approx 0.1$ . The resulting increment in  $\phi$  is calculated from Eq. (10). With  $\xi$  known from (1),  $R$  is known via Eq. (3). The integration is continued by one kilometer increments in  $r$  until  $R$  approaches a constant value. Table 1 shows the results of our calculation of  $R$  parameterized by the tangent height  $h$  for 3 density profiles taken from the U. S. Standard Atmosphere, 1962, and Supplement, 1966, for  $45^\circ$  N latitude.

The difference between the true and observed position of a star

TABLE 1

Angle of single refraction as a function of tangent height  
at 5000Å for three different U.S. Standard Atmospheres.

h (km)	45°N. July R(h) (deg.)	Mean Annual R(h) (deg.)	45°N. January R(h) (deg.)
0	.5238		
1	.4767	.5398	
2	.4274	.4934	.6139
3	.3910	.4504	.5472
4	.3565	.4102	.4853
5	.3240	.3731	.4250
6	.2932	.3387	.3847
7	.2664	.3069	.3475
8	.2416	.2777	.3134
9	.2188	.2509	.2821
10	.1977	.2265	.2540
11	.1784	.2050	.2288
12	.1617	.1926	.2128
13	.1518	.1644	.1826
14	.1298	.1401	.1563
15	.1106	.1195	.1339
16	.0944	.1019	.1146
17	.0812	.0870	.0982
18	.0688	.0743	.0841
19	.0583	.0634	.0722
20	.0495	.0542	.0617
21	.0420	.0467	.0530
22	.0357	.0396	.0453
23	.0304	.0337	.0387
24	.0259	.0286	.0330
25	.0221	.0243	.0282
26	.0188	.0207	.0240
27	.0162	.0177	.0205
28	.0138	.0151	.0176
29	.0117	.0129	.0151
30	.0100	.0110	.0128
31	.0085	.0094	.0109
32	.0073	.0081	.0093
33	.0062	.0070	.0079
34	.0053	.0059	.0068
35	.0046	.0050	.0058
36	.0039	.0043	.0049
37	.0034	.0036	.0041
38	.0029	.0031	.0035
39	.0025	.0026	.0029
40	.0021	.0023	.0025
		.0019	.0021
			.0018

near the limb as viewed from outside the atmosphere is given by Eq. (4) if one knows the tangent height  $h$  of the light ray. Here, we choose to specify  $h$  and then compute the true zenith angle  $Z$  from (4), (5) and (1) so that

$$Z = 2R(h) + 180^\circ - \sin^{-1}\left(\frac{(E+h)n(h)}{E+a}\right) \quad (11)$$

where  $a$  is the observer's altitude ( $a \geq 40$  km). For  $a = 440$  km (SKYLAB altitude), we have plotted  $Z - Z_{OB}$  vs  $Z$  in Fig. 2 for the three standard atmospheres previously mentioned. The position along each curve is parameterized by the tangent height  $h$ . Note that each curve has a "knee". This feature occurs at a unique value of  $h$  for each curve—13 km, 11 km, and 10 km for the July, mean, and January profiles, respectively. This corresponds to the height of the tropopause as is seen in Fig. 3 where the temperature profiles for these three atmospheres are presented.

The coordinate scale in Fig. 2 shows that the "knee" in each curve is characterized by a deviation of  $Z - Z_{OB}$  of about 20 arc seconds from a smoothed curve. This suggests that the feature is accessible to measurement as discussed in the next section. The abscissa in Fig. 2 is directly proportional to time. For an orbiting altitude of 440 km, a spacecraft's circular angular velocity,  $\omega$ , is about  $4^\circ/\text{min}$ . A star near the orbital plane will geometrically set (rise) at this rate,  $dZ/dt = \omega$ . Stars further removed from the plane will appear to move at a slower rate. The rate of stellar motion,  $dZ/dt$ , is related to the apparent motion of the star through the atmosphere,  $dh/dt$ , by the differentiation of Eq. (11) with respect to time. More

conveniently, one can read off  $\Delta h$  and the corresponding  $\Delta Z (= \omega \Delta t)$  from Fig. 2 to find  $dh/dt$  in the region  $9 \text{ km} \leq h \leq 14 \text{ km}$ . Thus, in this region, a star in the orbital plane will appear to move through a one kilometer layer in about 0.75 sec. This is about twice the time one would compute if there were no refraction ( $R(h) = 0$  and  $n(h) = 1$  in Eq. (11)). If the star is not in the orbital plane, the star will appear to move through a one kilometer layer on a "slanted path" in a time exceeding 0.75 sec. With the relation between  $Z$  and time known from the slope of the curves in Fig. 2, it is evident that the value of  $Z - Z_{OB}$  will change by 20 arc sec in about 0.1 sec of time. Thus, any detection system which can distinguish the "knee" in the curve will provide a resolution of the tropopause height of better than 0.15 km.

In using this method, a graph similar to Fig. 2 may be constructed by continuously tracking a single star or by measuring  $Z$  and  $Z_{OB}$  for a number of stars from a few photographs of rich star fields near the horizon. The values of  $h$  appearing in Fig. 2 are located in the following manner. The combining of Eqs. (4) and (11) yields

$$\sin(Z_{OB}) = \frac{(E+h)n(h)}{(E+a)} \quad (12)$$

In practice, perturbations of the values of  $n(h)$  from those calculated using the mean annual density profile have a negligible ( $< 0.15 \text{ km}$ ) effect on the resulting values of  $h$  found from (12). This means that Fig. 2 may be constructed entirely from observations and a standard table of  $n(h)$ . In this

sense, the method does not require supporting data or fitting of various models.

In the above analysis, we have assumed spherical symmetry through those regions of the atmosphere traversed by the starlight. Most of the refraction effects of interest arise in a region of influence between 9 and 15 km. Density variations above 15 km do not influence the "knee" structure in Fig. 2. The region of influence corresponds to a geocentric angle,  $\phi$ , of about  $5^\circ$ . If the atmosphere is not spherically symmetric in this region, one would expect the knee in Fig. 2 to have a more rounded appearance and the resulting tropopause height to be interpreted as an average height.

This technique essentially measures average density deviations from a smoothed background density as a function of height. The density deviations associated with standard tropopause models are readily detectable. At present, the observational effects of jet streams or extreme variations in tropopause height within the region of influence are unknown.

### 3. Comments on Measuring the Refraction

There are no major technical difficulties which prevent the orbital monitoring of the tropopause height. In general, three atmospheric factors affect such a measurement: color dispersion, turbidity, and turbulence. The color dispersion, which decreases with longer wavelength, can be reduced to an acceptable level by an appropriate bandpass filter. For example, a  $1000\text{\AA}$  bandpass centered at  $6500\text{\AA}$  results in a chromatic image spread of about 6 arc sec when a star is viewed through the 10 km level of the atmosphere. The turbidity, varying approximately as  $\lambda^{-4}$ , is also minimized by the selection of a long wavelength centered bandpass and for  $7000\text{\AA}$  amounts to less than one stellar magnitude for a star viewed through the 10 km level. The effect of turbulence, which could potentially cause apparent stellar image motion and thus reduce the accuracy of the tropopause measurement, is not well known. However, the image motion experienced with ground based telescopes is due almost entirely to atmospheric conditions in the immediate environs of the telescope and not to high level atmospheric effects. Since the total rms motion at a good ground observing site is about 1 arc sec, it is expected that image motion experienced by a satellite telescope would be substantially lower.

To resolve the "knee" in Fig. 2, a resolution of about 6 arc sec is necessary. The star will appear to move 6 arc sec in about .03 seconds of time. If we consider using stars equal to or brighter than say 3.0 magnitudes, they will appear to be brighter than 5.5 magnitudes when viewed through the atmosphere at a tangent height of 7 km. With a  $1000\text{\AA}$  bandpass filter centered at  $6500\text{\AA}$

the demands on the detection system are not severe. The requirements are satisfied, for example, by an aerographic camera with a 900 mm focal length f/5.6 lens, used with Tri X Astrographic film. A 5 x 5 inch film format would provide a sufficiently large field of view ( $8^{\circ} \times 8^{\circ}$ ) to include unrefracted stars so that accurate relative position measurements could be made. In addition, the satellite would have to maintain its attitude to within a few seconds of arc during the 0.03 sec exposure. Since present satellites are stabilized to a few arc sec per sec of time (Caron and Simon, 1975, and Marshall Space Flight Center, 1973), this should not prove to be a problem. Although a satellite system would, in practice, employ photoelectric star trackers, the above photographic example illustrates the ease with which sufficiently accurate observations could be attained to sense the tropopause height.

#### 4. Conclusion

The measurement of the position of rising or setting stars viewed from orbital altitudes provides a means of remote sensing of the height of the tropopause. Such a method has a number of advantages:

- 1) The method does not rely on any other supporting data, models, or measurements.
- 2) A very small amount of data analysis is needed to locate the "knee" and compute the angles of interest so that the method would readily lend itself to real-time or on-line data reduction.
- 3) Being a remote sensing technique, the method could be used for regions of the globe for which existing methods are not feasible.

There do exist, however, certain inherent constraints. A dark limb is required; for example, the Arctic region could not be monitored during the summer months. A cloudless atmosphere above the tropopause is also required, at least to the extent that stars are visible through the 8 or 9 km layer. But because an exact stellar flux measurement is not necessary (only the apparent position of the star is of importance), noctilucent or mother-of-pearl clouds along the line of sight would interfere with such measurements only if they reduced the stellar flux below a detectable level. Finally, the exact regions to be investigated are determined by the number of suitable stars and their relation to the orbital plane of the observing satellite.



Although we have stressed in this paper only the measurement of the height of the tropopause, additional information on the density profile is contained in the track of a setting or rising star. In a future paper, we hope to investigate both the extent of this information in the context of instrumental noise, atmospheric turbulence, and other uncertainties in the measurements, and, in addition, the coverage provided by a given number of suitable stars.

### Acknowledgements

We wish to thank Dr. Volker Mohnen for pointing out the relevance of our refraction studies to the tropopause problem and for his encouraging this effort and Dr. Edwin Danielsen for a critical reading of the manuscript. This work was supported in part by NASA Contract NAS 9-12539.

## References

- Allen, C. W., 1963: Astrophysical Quantities, London, The Athlone Press, p. 119.
- Caron, R. H., and Simon, K. W., 1975: Attitude Time Series Estimator for Rectification of Spaceborne Imagery., J. Spacecr. and Rockets, 12, p. 27-32.
- Danielsen, Edwin F., 1968: Stratospheric - Tropospheric Exchange Based on Radioactivity, Ozone, and Potential Vorticity, J. Appl. Meteor., 25, p. 502-518.
- Fesenkov, V. G., 1959: On the Optical State of the Atmosphere Illuminated by Twilight., Soviet Astron. AJ, 3, p. 207-213.
- Marshall Space Flight Center, 1973: Skylab Final Report, MSC-07191, 6/21/72, revised 3/1/73.
- U. S. Standard Atmosphere, 1962, Washington, D. C., U. S. Government Printing Office.
- U. S. Standard Atmosphere Supplements, 1966, Washington, D. C., U. S. Government Printing Office.

# Captions to Figures

Fig. 1 The geometry showing the refraction ( $Z - Z_{OB}$ ) for an observer at Q. The dashed curve is the actual light path.

Fig. 2 Refraction vs. true zenith angle of a setting (rising) star for an observer at 440 km. The dots and numbers refer to the tangent height in km through which the light ray is passing.  $Z$ , the true zenith angle of the observed star, is proportional to time,  $Z = \omega t$ . In this example,  $\omega = 4$  arc min/sec. The dots marked by subscripted T's identify the "knee" structure and correspond to equivalent points in Fig. 3.

Fig. 3 Temperature profiles from the U. S. Standard Atmosphere, 1962 and U. S. Standard Atmosphere Supplement, 1966. The subscripted T's designate the tropopause. Compare with Fig. 2.

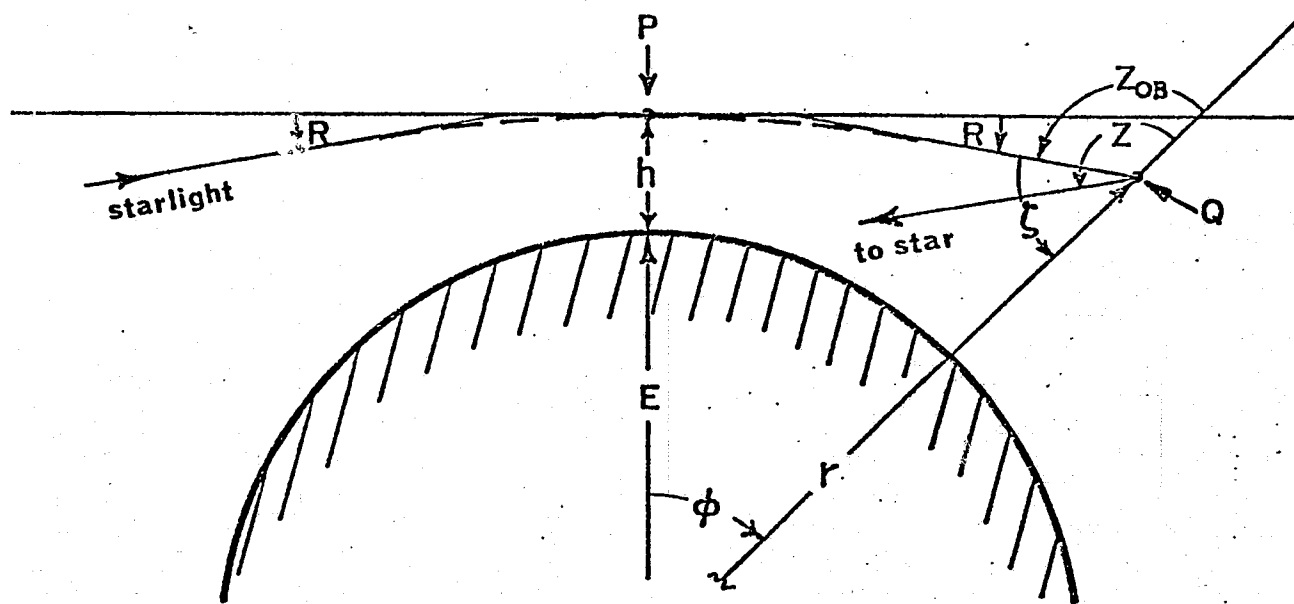


Fig. 1

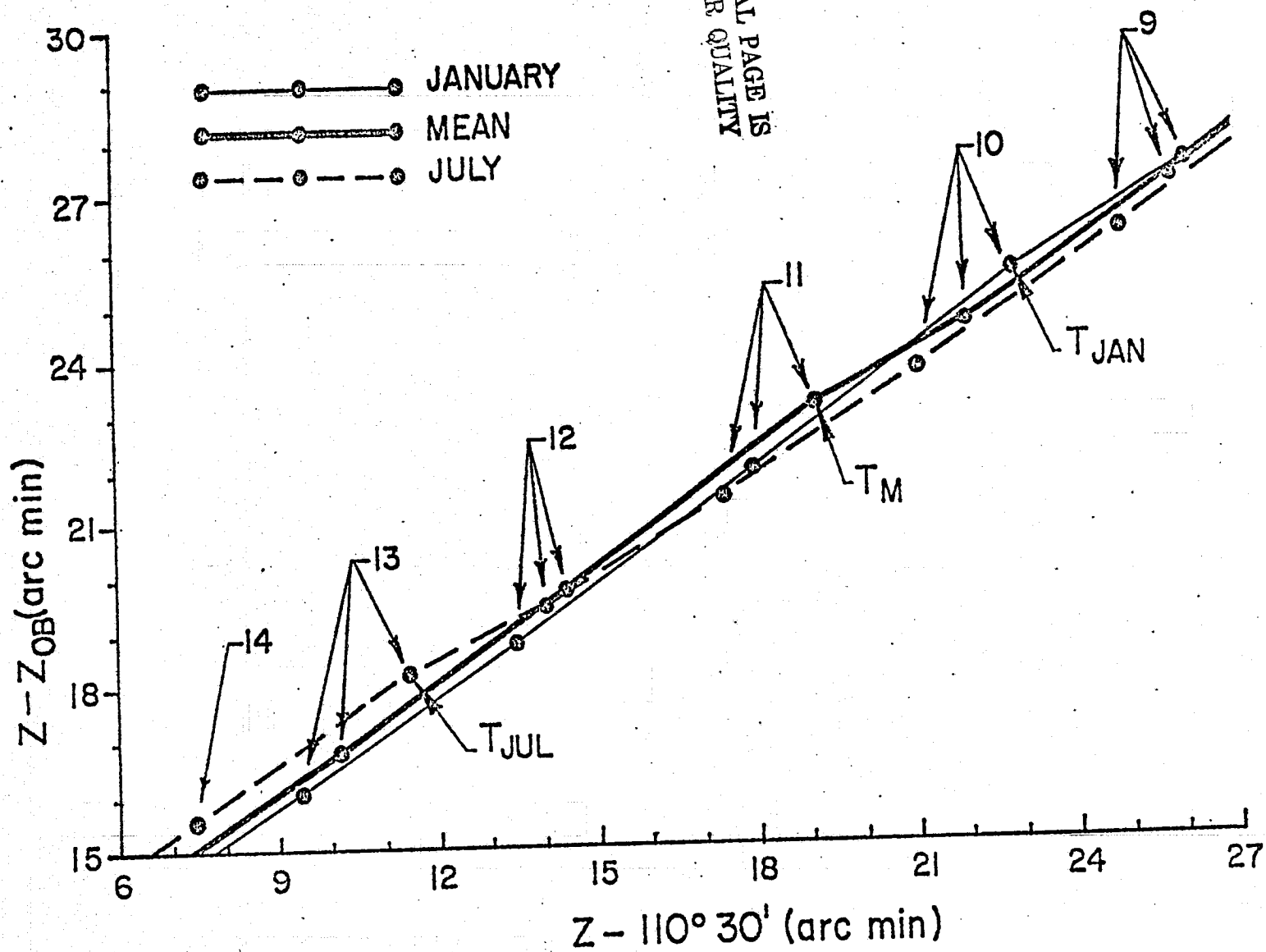


Fig. 2

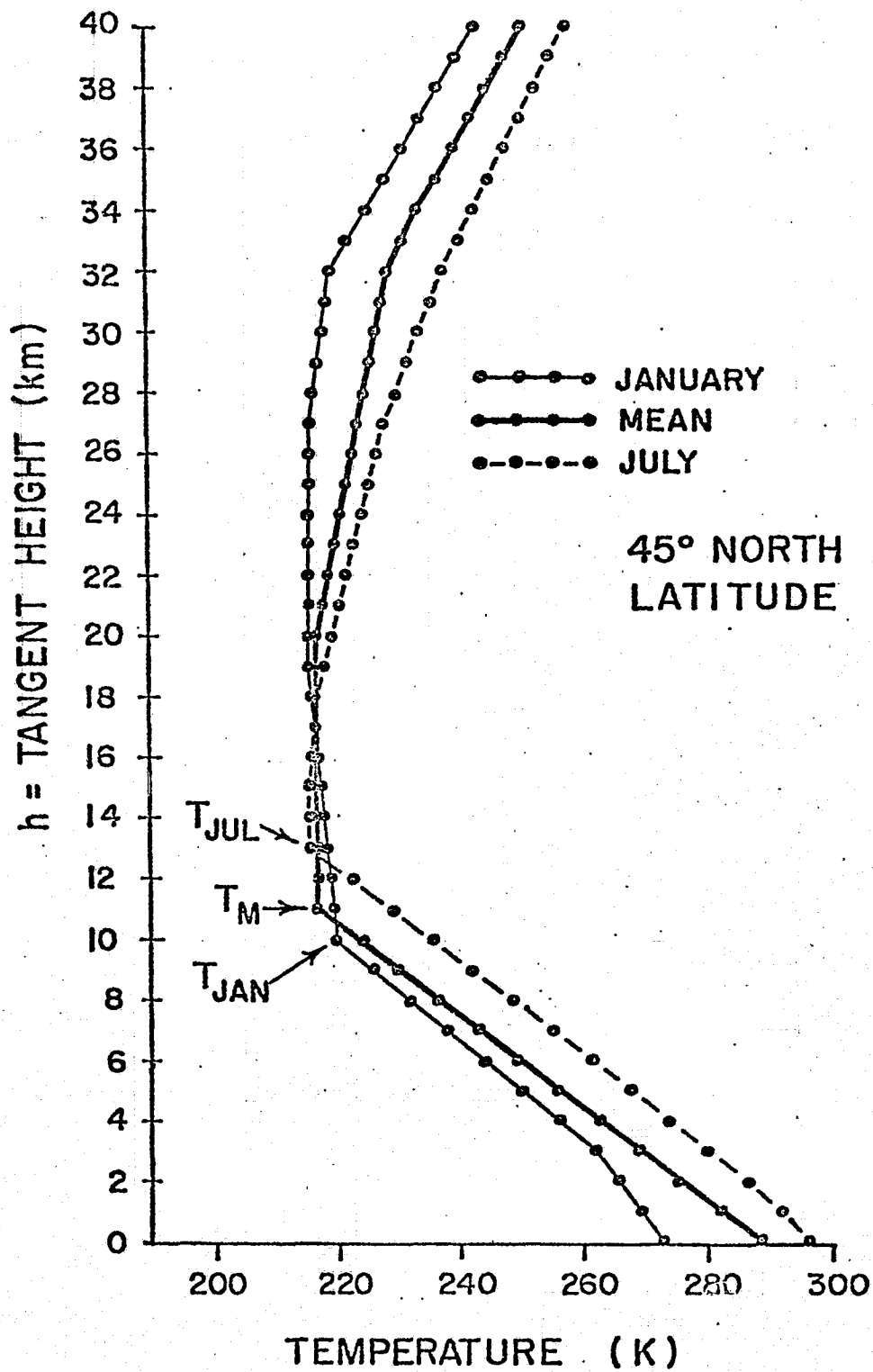


Fig. 3

**VI CORONAGRAPH-HORIZON STUDIES:**

**THEORY, OBSERVATIONS, AND RESULTS**



COMMENTS ON THE INVERSION OF HORIZON RADIANCES FROM SPACE

Donald W. Schuerman, Frank Giovane, and J. Mayo Greenberg

Dudley Observatory

and

The State University of New York at Albany

Albany, New York

Received: \_\_\_\_\_

## COMMENTS ON THE INVERSION OF HORIZON RADIANCES FROM SPACE

### Introduction

Satellite monitoring of horizon radiance profiles is a promising means of remotely sensing the aerosol constituent of the atmosphere on a global basis. Horizon observations provide the long pathlengths necessary to investigate the tenuous constituents of the stratosphere and mesosphere and also yield, because of the geometry involved, a natural vertical height resolution. The power of the technique was demonstrated from the Mercury 8 manned satellite (Mateer, Dave, Dunkelman and Evans, 1967) when a stratospheric dust layer was photographed using an on-board camera. Since then, limb horizon studies and observations have been pursued in both the Soviet Union (Kondratyev, Volynov and Galstev, 1971) and the United States (Grey and Merritt, 1971). Limb extinction measurements from high altitude balloons (Volz, 1971) have also been employed to investigate stratospheric aerosols, and Peppin, Rosen, Hofman and Kroening (1971) are proposing to adapt their solar extinction balloon methods to satellite monitoring.

The calculation of the day-time limb radiance profiles, assuming a given atmospheric structure, is a complex problem. The non-parallel geometry involved makes the inclusion of multiple scattering effects difficult. Three methods have been developed to cope with this problem. Collins, Blathner, Wells and Horak (1972) and others employ a backward Monte-Carlo technique. Gray, Malchow, Merritt, Var and Whitney (1973) have introduced

a multi-stream method. An Eddington-type approximation has been developed by Minin and Sobolev (1964) and expanded by Smoktiy (1969). The solution of the inverse problem, the extraction of information concerning the constituents of the atmosphere given the limb radiance, is only in its initial stage of development. Gray et al. (1973) have approached the problem using "filtering techniques" whereby the scattering constituents and their characteristics are adjusted to provide a best fit to the horizon data. The uniqueness of such solutions is not currently known. In this paper we suggest some elemental approaches to a direct solution of the inverse problem.

### A Statement of the Problem

The equation of radiative transfer defining the change in specific intensity over an element of the path  $ds$  is given by

$$\frac{dI}{ds} = \kappa I + \kappa B \quad (1)$$

where  $\kappa$  is the extinction coefficient.

The source function  $B$  is given by

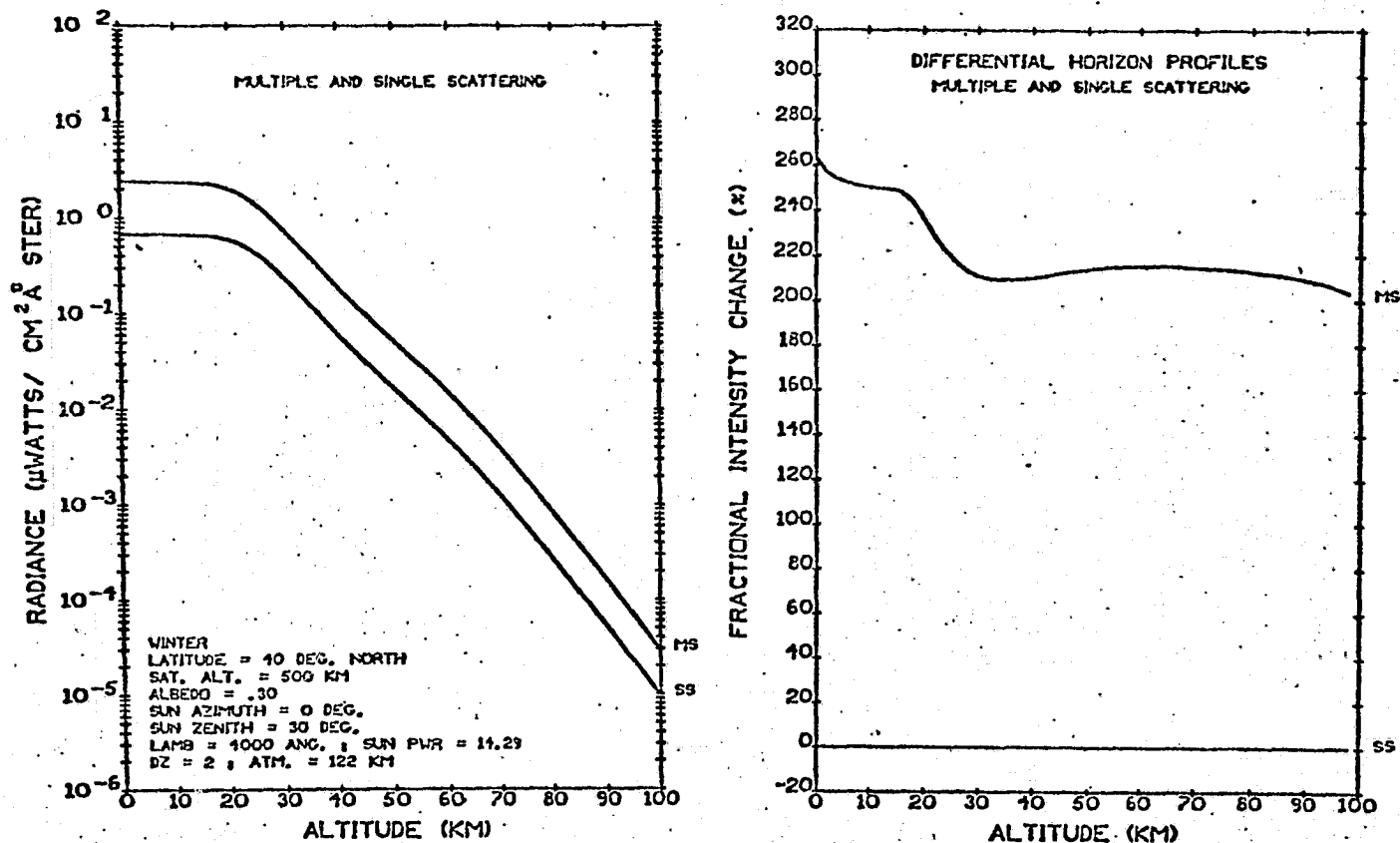
$$B = \beta \int I f(\omega, \omega') \frac{d\omega'}{4\pi} + \beta B_1 \quad (2)$$

where  $\beta$  is the single particle albedo,  $f(\omega, \omega')$  is the phase function, and  $B_1$  is the contribution to  $B$  caused by first order scattering, the scattering of radiation coming directly from the sun. Appropriate boundary conditions must take into account the reflective properties of the earth's surface or cloud decks. The first term on the right hand side (RHS) of equation (2) represents the contribution of multiple scattering to the source function. It is the coupling of this term with equation (1) through the complex geometry represented in the path length  $ds$  which makes the solution of this problem difficult, albeit soluble by the three methods previously mentioned. For a given solar angle, the final intensity observed is then a function of the zenith ( $Z$ ) and azimuthal ( $Az$ ) angles of the observer's line of sight and is given symbolically by

$$I(Z, Az) = R(Z, Az) + \int G(\omega, \omega') \frac{d\omega'}{4\pi} \quad (3)$$

The first term on the RHS of equation (3) represents the single scattering contribution to the observed radiance, while the second term represents multiple scattering effects. Note that this second term presumes a knowledge of the specific intensity along the entire line of sight,  $s$ . For an exact expression of the integrand see, for example, Kondratyev et al. (1971).

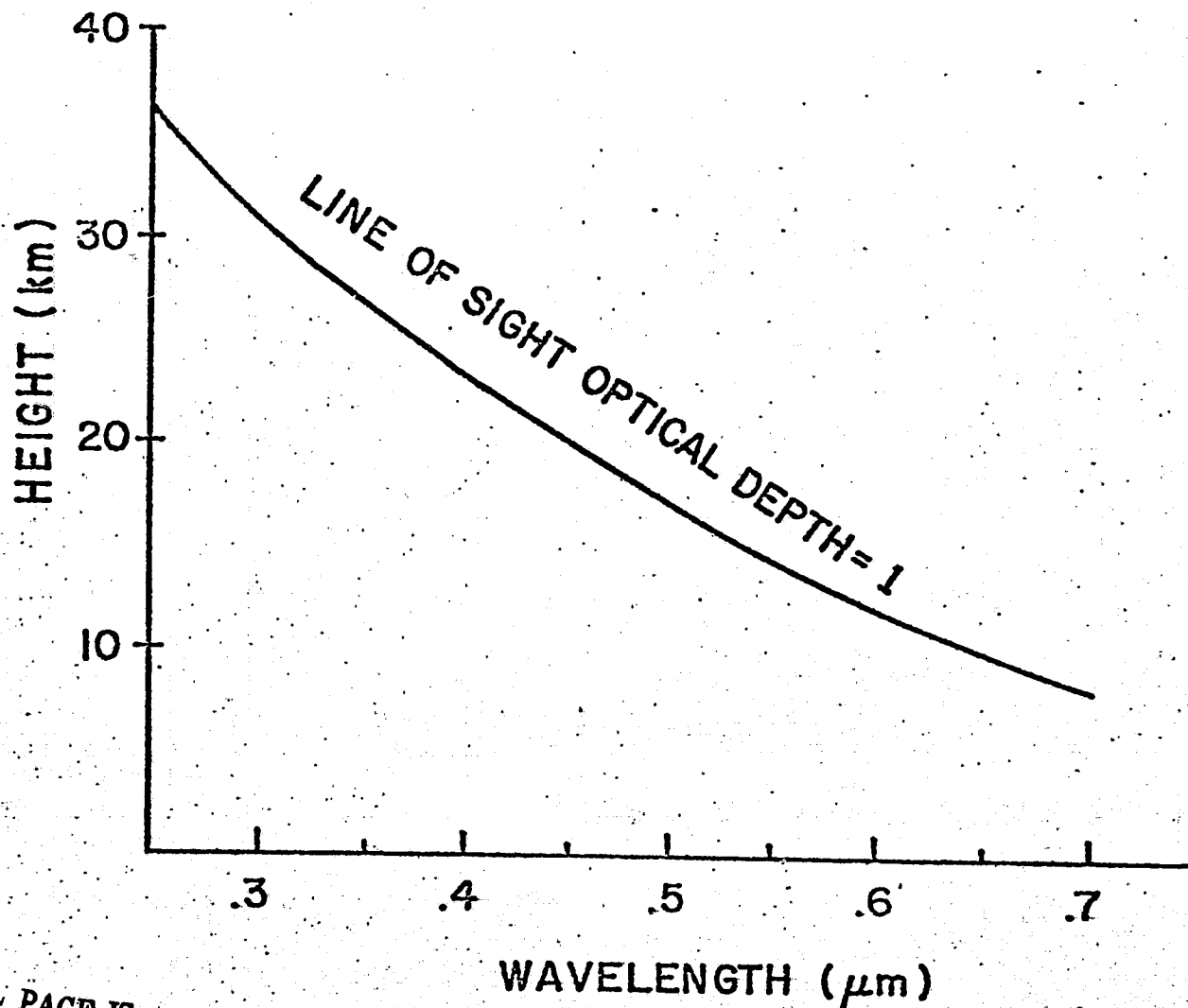
An iterative method of attack on the inverse problem is suggested by equation (3). Suppose that from some standard model of the atmosphere one calculates, by one of the three previously mentioned methods, the radiation field throughout the atmosphere. For a given set ( $i=1,2,\dots,n$ ) of observations,  $I_i(Z_i, Az)$ , one could compute from equation (3) a first approximation to the single scattering term,  $R(Z, Az)$ . Now the problem is simplified a great deal. If this single scattering problem could be inverted to yield a new atmospheric structure (an improvement on the standard model), this new structure would serve as a basis for computing a better approximation to multiple scattering. By successive iterations, the true structure of the atmosphere could be deduced. Aside from the questions of convergence of such a scheme, we suggest that an investigation of the inversion of the single scattering problem is of primary importance to the inversion of the complete problem. This suspicion is strengthened by comparison of the effects of multiple scattering with single scattering models for selected cases. Figure 1 by Gray et al. (1973) compares a single scattering (ss) profile with one that includes multiple scattering (ms) for the specific parameters listed. Note that above about 25 km, the shapes of the profiles are almost identical. Because of the logarithmic



ORIGINAL PAGE IS  
OF POOR QUALITY

Fig. 1 A comparison by Gray et al. (1973) of a single scattering (SS) radiance profile with one which also includes multiple scattering (MS) effects for the parameters listed.

coordinate scale used, this suggests that, to a good approximation above 25 km (at 4000<sup>8</sup>Å), the true radiance is just a constant factor times the single scattered radiance. This approximation fails to some extent for altitudes below 25 km where the optical depth along the line of sight is near to or greater than unity. For longer wavelengths, the optical depth equals unity at successively lower altitudes. (For reference, we show in Figure 2 this wavelength dependence for a Rayleigh scattering atmosphere.) The proportionality between single and multiple scattering radiances is not necessarily a general property of all profiles. In fact, this relationship deteriorates somewhat for longer wavelengths (Gray et al. 1973) and perhaps with increasing solar zenith angle (Kondratyev et al. 1971). However, this relationship does suggest that the inversion of the single scattering problem is fundamental to the solution of the complete problem. Finally, we remark that a study of the single scattering inverse problem should suggest what measurements and which instrumentation are best suited for horizon observations and what auxiliary measurements would be helpful in the remote sensing of stratospheric aerosols. For the above reasons, the remaining portions of this paper are devoted to the inversion of single scattering horizon profiles.



ORIGINAL PAGE IS  
OF POOR QUALITY

Fig. 2 The tangent height at which the line of sight optical depth equals unity as a function of wavelength for an observer outside the atmosphere. A Rayleigh scattering atmosphere (no aerosols) is assumed.



### Uncoupling of Layers

The direct calculation of the single scattering intensity of the horizon radiance is straightforward but cumbersome because of the geometry involved. Since an understanding of this geometry is vital to the inversion process, we review here the significant relationships and establish our nomenclature. Figure 3 identifies the needed parameters. It is assumed that an observer at the point O knows his altitude (a), the earth's radius (R), the zenith angle of the sun (SA), and both the zenith (Z) and azimuthal (Az) angles of the line of sight, s. Az is measured from the solar meridian. For ease of presentation, the figure shows only the particular case for  $Az = 0$ , but the development of the pertinent formulas is for the general case,  $Az \neq 0$ . The line of sight (neglecting refraction) has as its closest approach to the earth the distance Y, which we refer to as the tangent height. Y and Z are related by

$$\sin (180^\circ - Z) = \frac{R+Y}{R+a} \quad (4)$$

Also needed are expressions for  $\psi$ , the angle between the vector through Y and the terminator, and  $\phi$ , the scattering angle. We find that

$$\sin \psi = \cos SA \sin Z - \sin SA \cos Z \cos Az \quad (5)$$

and

$$\cos \phi = \cos SA \cos Z + \sin SA \sin Z \cos Az. \quad (6)$$

In describing the scattering process at some point, P(h), we need



expressions for the path length elements  $ds$  and  $dt$  where  $ds$  is an element along the line of sight to  $P(h)$  and  $dt$  is an element along the path of solar radiation to  $P(h)$ . Let  $(R+y)$  be the distance of closest approach to the center of the earth on path  $\underline{t}$ . Likewise,  $(R+Y)$  is defined by the distance of closest approach along the line of sight. It is then clear from the figure that

$$ds = \frac{(R+h'') dh''}{\{(R+h'')^2 - (R+Y)^2\}^{1/2}} \quad \text{and} \quad dt = \frac{(R+h') dh'}{\{(R+h')^2 - (R+y)^2\}^{1/2}} \quad (7)$$

The quantity  $(R+Y)^2$  is defined by equation 4, but  $(R+y)^2$  is a function of the point  $P(h)$ . We find that the general relation is

$$(R+y)^2 = (R+h)^2 - [(R+Y) \sin \psi \pm \{(R+h)^2 - (R+Y)^2\}^{1/2} \cos \phi]^2. \quad (8)$$

Proper attention must be given to the choice of signs in equation (8).

If the point  $P$  is between points  $O$  and  $Q$  on the line of sight, the negative sign is used. If  $P$  is sunward of  $Q$ , the positive sign is employed. Notice also in equation (8) that  $y$  is not necessarily positive.

Equipped with the above geometry, we can now describe the single scattering process at the point  $P$ . Let the solar flux at the point  $P$  be given by  $F_p(h) = F_0 E_1$  where

$$E_1 = \exp \int_h^{h_t} \frac{\kappa(h') (R+h') dh'}{\{(R+h')^2 - (R+y(h))^2\}^{1/2}}, \quad (9)$$

$F_0$  being the unattenuated solar flux and  $\kappa$  the coefficient of extinction. The starred integral sign represents the fact that the integration over

the path may take one through the branch point of the integrand in equation (9). In such cases (as in Figure 3) the starred integral sign is interpreted to read

$$\int_{\star, h}^{h_t} = \int_y^{h_t} + \int_y^h. \quad (10)$$

The radiation scattered at point P suffers a further attenuation,  $E_2$ , on its way to the observer:

$$E_2 = \exp \left[ - \int_{\star, h}^{h_t} \frac{\kappa(h'')(R+h'') dh''}{\{(R+h'')^2 - (R+Y)^2\}^{1/2}} \right] \quad (11)$$

where the starred integral sign has the same meaning as before if  $y$  is replaced by  $Y$  in equation (10). The scattering process itself is described by the scattering coefficient  $\sigma(h)$  and a phase function,  $f(\phi, h)$  (normalized to  $4\pi$ ), so that the contribution from the scattering element at P to the monochromatic specific intensity of the observer is

$$R_p(h, s) = F_\odot \frac{f(\phi, h)}{4\pi} \sigma(h) E_1(h) E_2(h) ds. \quad (12)$$

The total monochromatic intensity observed at O is then the totality of contributions from all points along the line of sight,

$$R(Y, Az, SA) = F_\odot \int_{\star, h_t}^{h_t} \frac{f(\phi, h)}{4\pi} \sigma(h) E_1(h) E_2(h) \frac{(R+h) dh}{\{(R+h)^2 - (R+Y)^2\}^{1/2}}. \quad (13)$$

The two attenuation terms,  $E_1$  and  $E_2$ , involve the extinction

coefficient  $\kappa$  at the wavelength under investigation. Radiation is attenuated by both scattering and absorption processes. We assume that the scattering is attributable to molecular (Rayleigh) and aerosol scattering and absorption is due to aerosols and ozone. By the proper choice of the bandpass, other molecular bands and spectral features can be avoided. Thus

$$\kappa = \sigma_m + \sigma_a + a_a + a_o = \sigma + a \quad (14)$$

where  $\sigma$  represents scattering terms,  $a$  represents absorption, and the subscripts  $m$ ,  $a$ , and  $o$  stand for molecular, aerosol and ozone, respectively. The single scattering albedo is thus given by  $\beta = \sigma / (\sigma + a)$ .

The scattering function,  $\frac{f(\phi, h)}{4\pi} \sigma(h)$ , in equation (13) likewise consists of two components,

$$f(\phi, h) \sigma(h) = f_m(\phi) \sigma_m(h) \left( 1 + \frac{f_a(\phi, h) \sigma_a(h)}{f_m(\phi) \sigma_m(h)} \right) \quad (15)$$

where the phase function for Rayleigh scattering is given by

$$f_m = \frac{3}{4} (1 + \cos^2 \phi). \quad (16)$$

The advantages of the daylight horizon scanning method become obvious when one attempts to investigate the inversion of equation (13). Thanks to the unique vantage point of the spacecraft, any observation along the line of sight parameterized by the tangent height  $Y$  is affected in the single scattering approximation only by the scattering characteristics at height  $Y$  and those above  $Y$ . The lower levels of the atmosphere are not involved. Only for spacecraft horizon observations can the line of sight be parameterized by the height  $Y$ , and only for horizon daylight ( $\psi$  positive

in Figure 3) observations do the layers below Y not contribute to the single scattering term. Observations made after spacecraft sunset must deal with a coupling in the attenuation term,  $E_1$ , of all layers. The advantages thus gained by daylight horizon observations should be exploited wherever feasible. For this reason, an iterative procedure (as discussed in Section II) which updates the multiple scattering contribution after comparisons with observations allows one to attack the inversion problem at a point where these advantages can best be brought into play.

Assume that the atmosphere consists of a series of homogeneous, concentric shells as represented in Figure 4. Furthermore, assume that the atmospheric structure above layer  $n$  is known. Schematically, let  $F_{\odot} \frac{f(\phi)D}{4\pi}$  represent the summation of single scattering events from point 1 to point 2 along the line of sight, and let  $F_{\odot} \frac{f(\phi)A}{4\pi}$  represent the same between points 3 and 4. Furthermore, let  $B$ ,  $C$  and  $E$  represent the attenuation suffered along the paths shown in the figure. The five quantities,  $A$  through  $D$ , can be computed since they are derived from the known atmospheric structure above layer  $n$ . The thickness of the layer  $n$  itself is determined by the resolution of the detector. By a suitable differencing of equation (13), the total monochromatic intensity due to single scattering along the line of sight is given by

$$4\pi \frac{R}{F_{\odot}} = fD + E \left\{ fAe^{-2\kappa s} + f\sigma s [ B e^{-\kappa bs} + Ce^{-\kappa cs} ] \right\} \quad (17)$$

where

$$b = \frac{(t_2 + 3s/2)}{s} \quad \text{and} \quad c = \frac{(t_1 + s/2)}{s} \quad (18)$$

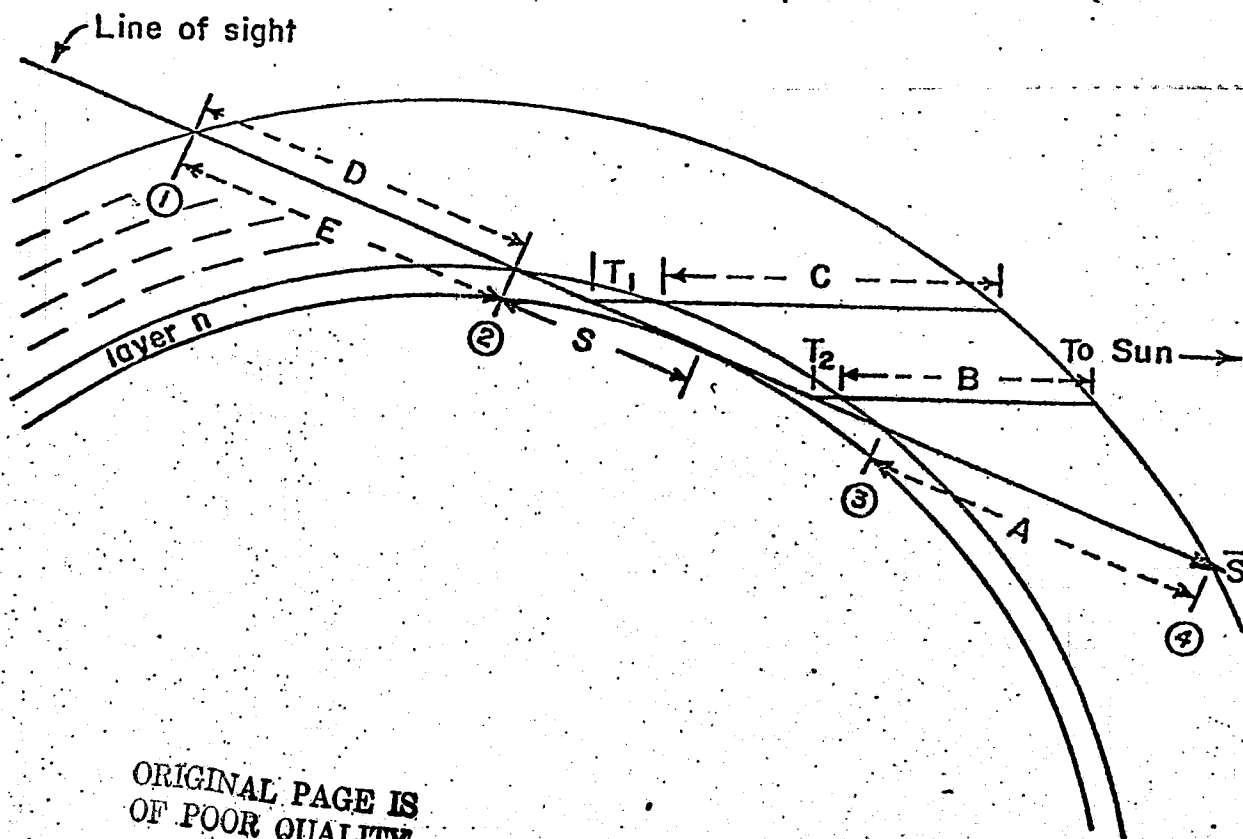


Fig. 4 A schematic representation isolating the  $n^{\text{th}}$  layer from overlying layers. The quantities  $S$ ,  $T_1$ , and  $T_2$  are geometric lengths.  $E$ ,  $C$ , and  $B$  represent the attenuation of radiation along the paths indicated.  $A$  and  $D$  represent the contribution to the observed single scattering radiance along the indicated segments of the line of sight,  $s$ .

In equation (17), all coupling between layers has been removed. It provides a suitable arena for the discussion of which measurements can be made and what assumptions are necessary to extract from the normalized single scattering intensity,  $4\pi R/F_0$ , the parameters of interest.



### Discussion of Measurements and Assumptions

We remark here that the RHS of (17) is a function of  $\sigma_n$ ,  $f(\phi_n)$  and  $\kappa_n$ . The determination of satisfactory values for these quantities will allow one to proceed to the next layer. But for an updating for the multiple scattering contribution by an iterative method (Section II), the total phase function  $f(\phi)$  must be known or assumed, not just  $f(\phi_n)$ , the value of  $f$  along the line of sight. Thus we are faced with the problem of forming an optimum set of measurements and assumptions which establish values for the three parameters in equation (17) and for the function  $f(\phi)$ . Of course, if polarization is taken into account,  $f(\phi)$  becomes a multiple-component object.

The ratio  $f_a \sigma_a / f_m \sigma_m$  in the definition (15) of  $f\sigma$  has certain general properties which can be utilized in deciding what observations or instrumentation should be employed for horizon studies. The aerosol phase function,  $f_a(\phi)$ , will always peak more in the forward ( $\phi=0$ ) direction than  $f_m(0)$ . Thus, if the detector is capable of looking near the sun, the ratio  $f_a/f_m$  amplifies by more than a factor of 10 the ratio of  $\sigma_a/\sigma_m$  and thus produces a more "aerosol sensitive" measurement. Such a measurement involves the use of a highly baffled instrument probably employing an external occulter to mask the optics from the direct rays of the sun. Such measurements are limited to times near spacecraft-twilight when the sun is near the horizon. In this mode, polarization effects in the single scattering approximation are minimal (van de Hulst, 1957). Thus, sensitivity to aerosols is gained at a cost of losing polarization information and

restricting observations to particular orbits and times therein. However, it is just these restricted orbits which may be used to measure the extinction simultaneously with the scattering. Since this mode already requires solar tracking to keep the detector eclipsed by an occulting disk, solar extinction measurements can be made at the time of sunset (sunrise). The external occulting disk itself can be used as a mount for the extinction sensor. In principle, the extinction measurement determines the monochromatic quantity  $\kappa(h)$  in equations (9 and 11). Furthermore, since this measurement would be made nearly simultaneously with that of the scattering radiance, the measured extinction occurs in the same vicinity of the atmosphere as that from which the radiance is measured. A satisfactory inversion of equation (17) for the value of  $\sigma(h)$  coupled with the extinction measurement of  $\kappa(h)$  would thus immediately yield the single scattering albedo of the aerosols. This albedo is of primary interest for the interpretation of the character of the aerosols. Furthermore, without such information, one must assume a value for  $\kappa(h)$  in order to make further progress in the solution of equation (17). With  $\kappa$  known, however, equation (17) contains only two unknown quantities,  $f(\phi_n)$  and  $\sigma(h)$ . Furthermore, by the use of an imaging detector or one which makes several simultaneous multispectral horizon scans, the properties of the function  $f(\phi, h_n)$  may be investigated in the near forward direction ( $1^\circ \leq \phi \leq 10^\circ$ ). In particular,  $df/f d\phi$  at constant  $h$  may be obtained directly from say a monochromatic photograph or angular ( $Az$ ) scan. Not only is such a quantity helpful in the analysis of the aerosols, but it also places measured limits on the

shape of the function  $f(\phi)$  which is needed in the iterative procedure of Section II for multiple scattering. Schemes which do not employ measurements near the sunward direction do not suffer the orbital restrictions of the forward method, and measurements near  $90^\circ$  increase the "sensitivity to polarization" for single scattering. However, the near-simultaneous measurement of extinction cannot be made independently, so that one must then assume values for  $\kappa(h)$ .

We assume here that all measurements are of a multispectral nature so that both  $f$  and  $\sigma$  are well represented over the visible spectrum. Gray et al. (1973) have calculated a large number of simulated atmospheres which show the effects of aerosol concentration, size distribution, and index of refraction on the resultant radiance profiles with polarization taken into account. Such studies are extremely valuable in tailoring a given experiment to a particular aerosol investigation. However, we wish to emphasize some elemental considerations at this point. First, of all, the equation of radiative transfer contains only the bulk quantities  $f(\phi, h)$ ,  $\sigma(h)$  and  $\kappa(h)$ . These quantities in turn depend upon an ensemble of sizes, shapes, and indices of refraction. If the values for  $f(\phi, h)$  (in general a multicomponent object),  $\sigma(h)$  and  $\kappa(h)$  could be ideally measured as a function of height, angle and wavelength, they would not necessarily determine uniquely the physical properties of aerosols. What they do provide are certain limits and constraints on the nature of the aerosols and a ready means of detecting the temporal changes in number and physical properties. The proper role of remote sensing is to invert from radiance measurements the monochromatic values of  $\kappa$ ,  $f(\phi)$  and  $\sigma$  with as little

appeal to the substructure of these quantities as possible. Certainly experiments should be designed using appropriate bandpasses, angular spread, and polarization bands in order to investigate specific areas of the substructure, but the inversion process for determining  $f$ ,  $\sigma$ , and  $\kappa$  should ideally strive to keep assumptions about the substructure to a minimum. If this is not done, the uncertainty in the choice of a size distribution and errors inherent in the usual assumptions of particle sphericity (Greenberg and Hong, 1973) and surface smoothness (Greenberg, Wang and Bangs, 1971) are inflicted upon the recovery of the bulk parameters.

## Methods of Solution

We now look at equation (17) in more detail. Two methods of solution will be discussed. The first method attempts to solve equation (17) simultaneously for both the scattering and extinction coefficients. It will be shown that this method is not satisfactory because of its failure to yield solutions in practical applications. The second method assumes the extinction is known from an independent measurement. The inversion of equation (17) then becomes straightforward, and a noise analysis shows the solution to be quite stable. Although the implications drawn from the investigation of these methods are of a general nature, we limit the exact calculations to a specific wavelength and geometry for which we have a future application. Furthermore, the main features of the inversion methods can most easily be demonstrated for the no aerosol case,  $\sigma_a = 0$ . In practice, this situation ( $t_a \sigma_a / t_m \sigma_m \ll 1$  in equation (15)) may be approached for wavelengths in the blue end of the spectrum but short of the ultraviolet ozone peak. Since  $\sigma_m$  is proportional to  $\lambda^{-4}$  and  $\sigma_a$  goes roughly like  $\lambda^\delta$  where  $\delta < 4$ , the ratio  $\sigma_a / \sigma_m$  decreases for smaller wavelengths. Thus, Gray et al. have shown that below 4000Å, the profiles are least sensitive to aerosols. We choose the wavelength region near 3600Å for our examples. The geometry is defined by the specification that  $A_z = 0$ ,  $SA = 104.05^\circ$  and  $a = 450$  km.

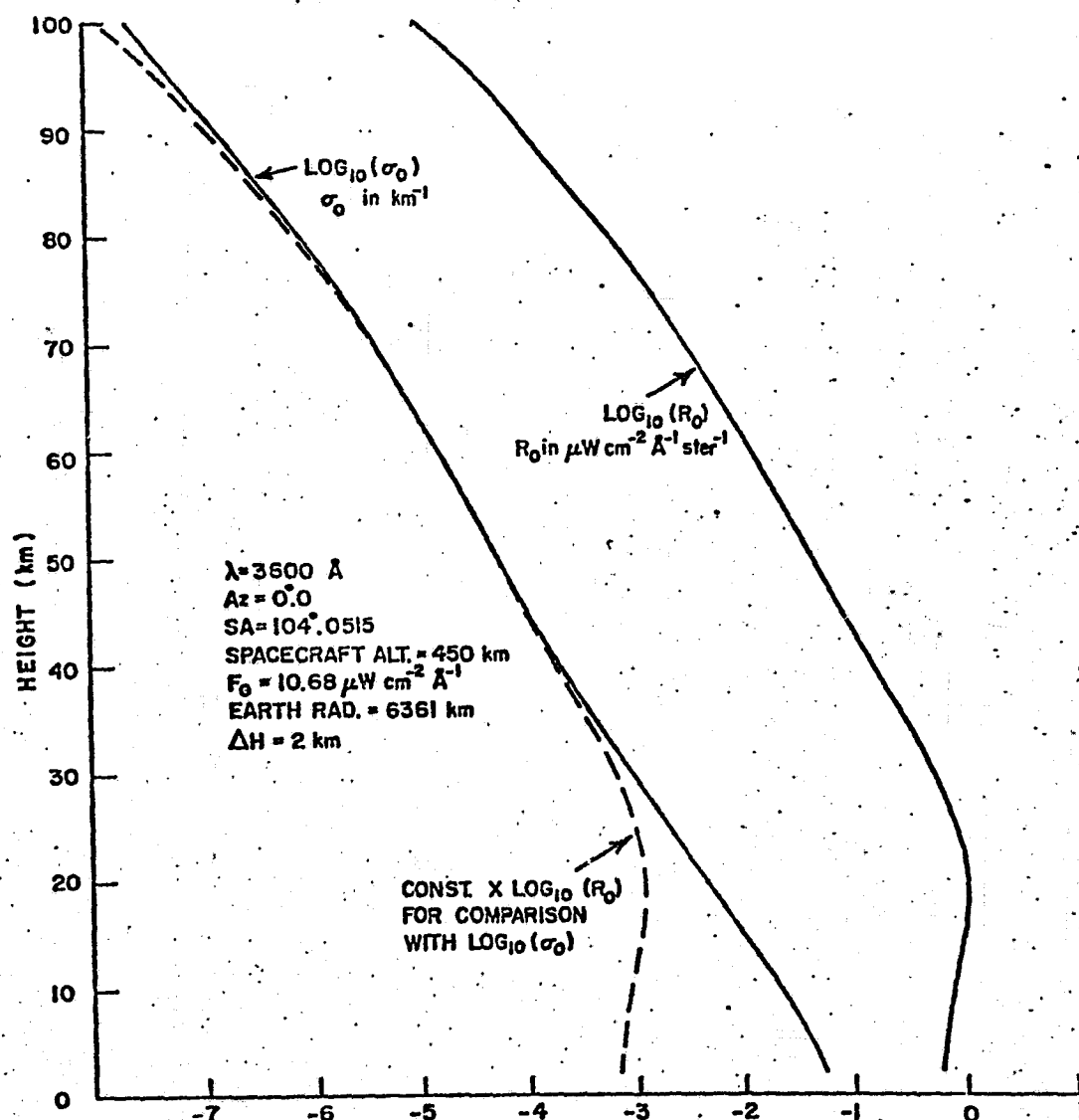
With the above assumptions, equation (17) takes the form

$$Q(s) = Ae^{-2\tau} + \tau [Be^{-b\tau} + Ce^{-c\tau}] \quad (19)$$

The  $\tau$  introduced here is the optical depth  $\tau = \sigma s$  where  $s$  is only half that part of the line of sight penetrating layer  $n$  as shown in Figure 4. For a particular line of sight  $s$  is given by the value of

$$O(s) = \left( \frac{R 16\pi}{F_0 3(1 + \cos^2 \phi_n)} - D \right) / E \quad (20)$$

and is assumed known since  $R$  is derived from measurement and  $D$  and  $E$  are contributions from overlying layers. For the top layer  $A=D=0$ ,  $E=B=C=1$ , and for the geometry assumed above,  $b=1.75$  and  $c=0.33$  irrespective of  $n$ , the layer under investigation. To understand the multi-valued nature of equation (19), we first directly calculate (given  $\sigma(h)$ ) the horizon radiance at  $3600\text{\AA}$  assuming each layer to be homogeneous and 2 km thick. The results of this calculation are shown in Figure 5 along with  $\sigma(h)$ . We then extract from the model the values of  $A$ ,  $B$ ,  $C$ ,  $b$ , and  $c$  for each layer  $h$ . For each 2 km layer, the function  $O(\tau)$  is generated. This function, computed for several selected layers, is shown in Figure 6. Each curve  $O(\tau)$  is parameterized by its tangent height (in km). The intersections of the dashed curve with the parameterized function  $O(\tau)$  represent the correct inverse solution of equation (19),  $\tau_0(h)$ , for each layer  $n$ . The curve  $O(\tau)$  for  $k=12$  km in Figure 6 illustrates the problem of root selection. The  $O(h=12)$  value of 0.498 has as its solution 3 values of  $\tau$  as indicated in the figure. Only the root indicated by the number 3 is identical to the value of  $\tau_0(12)$  found from the direct calculation of the radiances. In order to select the proper root, we used as an initial estimate of  $\tau_0(h)$  a quadrature extrapolation based on the 3 preceding intersection points. Thus, for example, the initial guess for



ORIGINAL PAGE IS  
OF POOR QUALITY

Fig. 5 The single scattering radiance profile,  $R_0(h)$ , calculated from a Rayleigh scattering atmosphere whose scattering coefficient,  $\sigma_0(h)$ , is also shown as a function of height. The shapes of the profiles are similar between 30 and 70 km.

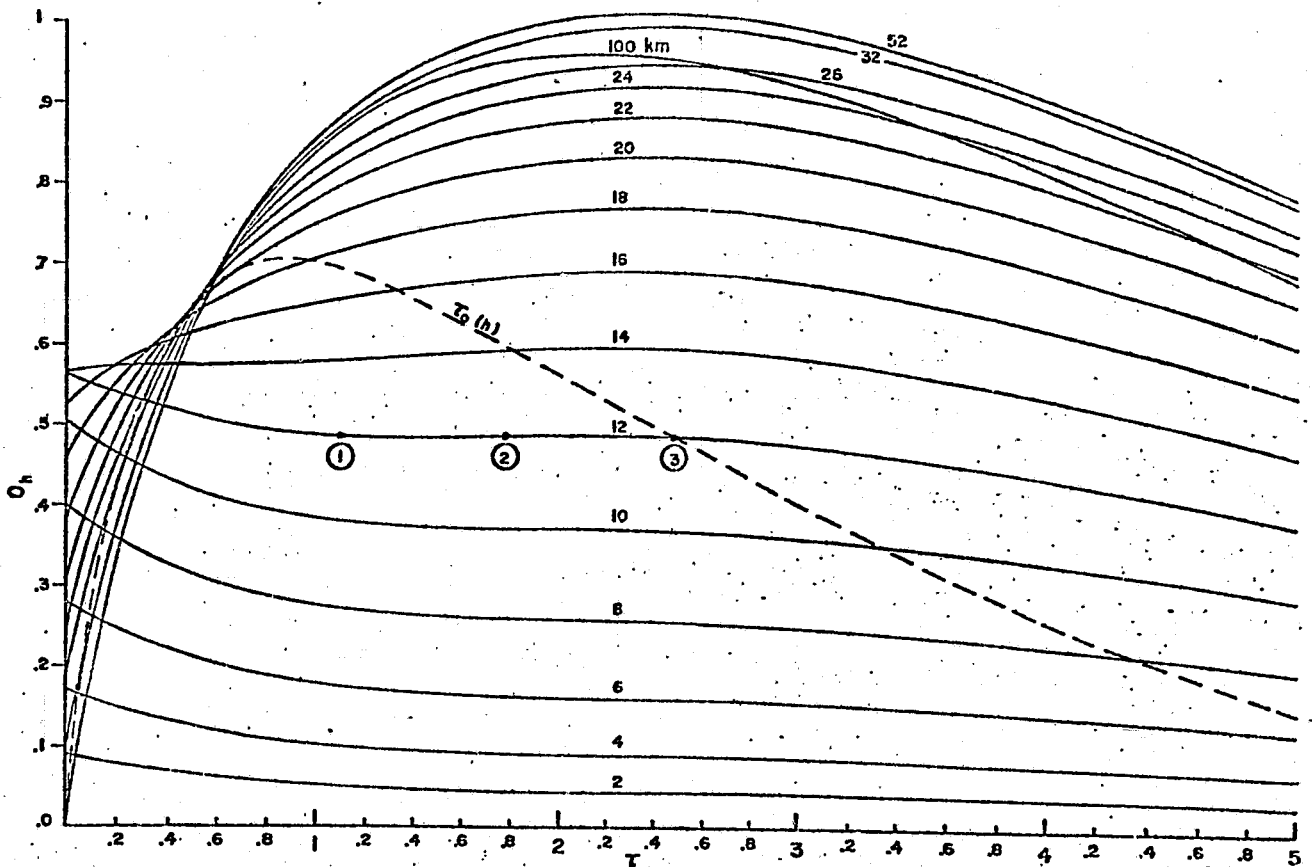


Fig. 6 The function  $O(\tau)$  given by equation (19) for selected values of the tangent height. At each height there exists from observations a value  $O_h$  from which  $\tau_0(h)$  is determined. The dashed curve shows the correct solution for  $\tau_0(h)$ . Care must be taken in the selection of the proper roots.  $O_{12}$  is satisfied not only by the proper root labeled 3 but also for values of  $\tau$  located at points 1 and 2.



$\tau(12)$  is determined by  $\tau(9)$ ,  $\tau(10)$ , and  $\tau(11)$ . Using this predictor scheme, we were able to invert the horizon radiance for  $\tau_0(h)$ .

The method outlined above was found to have a major disadvantage. The quantity  $O(s)$  defined by equation (20) is in general a linear function of  $R/(F_0 f)$ . In practice, this last expression is usually known only to within a constant factor  $C$  for several reasons. First, the absolute calibration of the instrument or the solar flux,  $F_0$ , may be known only within a factor for a given bandwidth and shape. Second, one may wish to include the effects of multiple scattering in the form  $C \times R$  as discussed in Section II. Finally, the value of the phase function  $f(\phi)$  may not be known absolutely. We point out here that from orbiting altitudes, the angle subtended by the limb and the 80 km tangent height of the atmosphere corresponds to less than  $2^\circ$ . In many cases  $f(\phi)$  can be assumed to change very slowly over this two degree interval and thus be considered an unknown constant in equation (20). Thus, for a number of reasons met in practice, we attempted the inversion of  $C \times R$  in the same manner as before. Figure 7 shows the results of the inversion for  $C = 1, 2$ , and  $0.5$ . For layers above 35 km, the results differ in a linear fashion as expected. For layers below 35 km ( $\tau = 0.1$ ), extinction effects, the exponentials in equation (19), become dominant. For the case  $C = 2$ , no solutions exist for layers below 30 km. For the case  $C = 0.5$ ,  $\tau$  has a maximum at 22 km which implies that the air density at this layer is greater than at the limb. Furthermore, for both these cases we constructed plots similar to Figure 6 (the case  $C = 1$ ). The plots verified that indeed the solutions shown in Figure 7 are the only continuous solutions. They reflect an instability around the  $C = 1$  solution as successively lower layers are inverted.

ORIGINAL PAGE IS  
OF POOR QUALITY

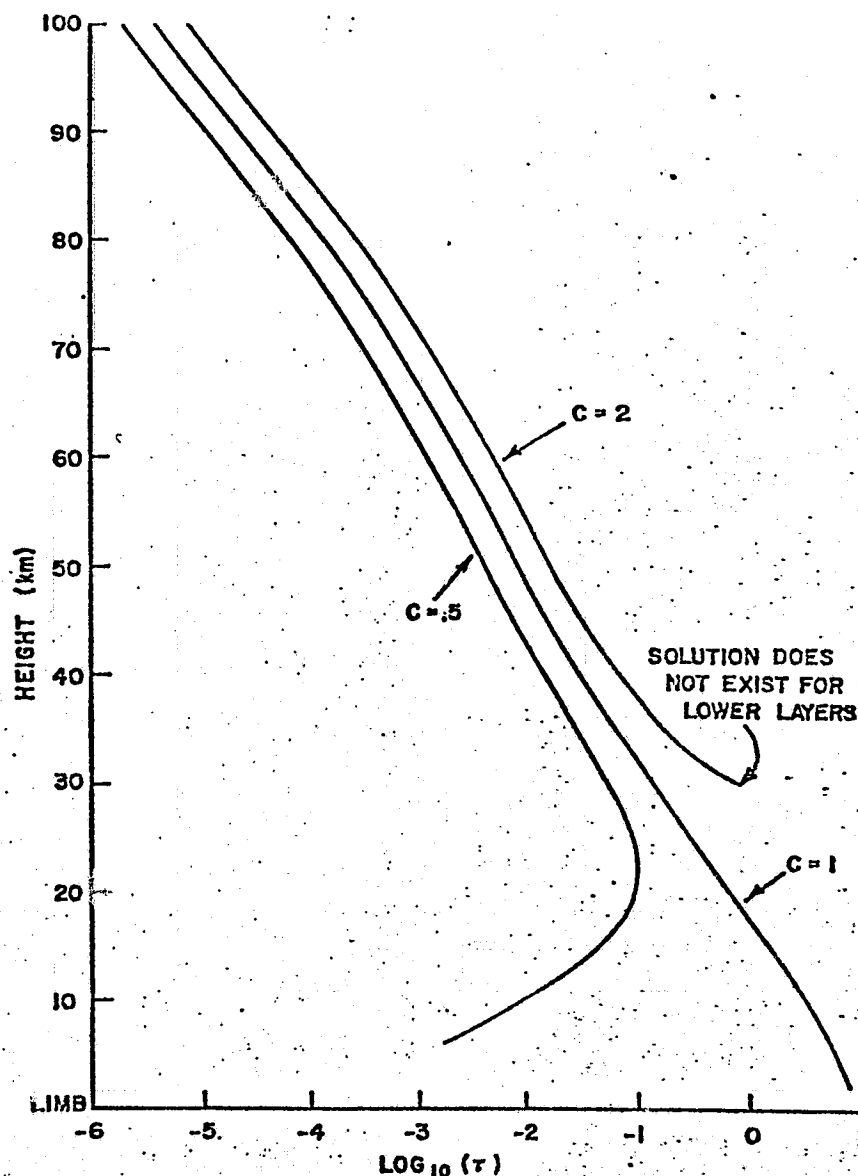


Fig. 7 The inversion of a horizon profile for  $\tau(h)$  by the first method described in the text. The curve  $C = 1$  corresponds to the recovery of the scattering coefficient,  $\sigma_0(h)$ , in Fig. 5. The two other inversions result when the observed radiance in Fig. 5 is multiplied by  $C$ . These two solutions yield unphysical results below 30 km.

This instability is not encountered if one assumes that the extinction (the exponentials in equation (19)) is known. Ideally the extinction coefficient,  $\kappa(h)$ , can be measured independently and nearly simultaneously by a solar extinction measurement as previously mentioned. Equation (19) then shows  $\tau$  in a linear relationship to known quantities, and the exponential instability shown in Figure 5 is avoided. This method, which we hereafter refer to as linear, is also useful in isolating the intrinsic geometrical stability of any direct inversion method for horizon profiles. The question may be stated as follows: To invert a given tangent layer, the effects of overlying layers are subtracted from observations. The inversion of the  $n^{\text{th}}$  layer depends in part on the precision of one's knowledge of the overlaying layers. If some "noise" exists in the overlying layers, does it damp out as one investigates the lower layers? To explore this geometrical propagation of errors, we have used the linear method to invert fifty simulated radiance scans,  $R(h)$ , each with a random noise normally distributed. The fifty scans are represented by

$$R(h) = R_0(h) (M(h) \pm SD(h))$$

where  $R_0(h)$  is the radiance of the standard model shown in Figure 5,  $M(h)$  is the normalized mean and  $SD$  is the standard deviation of the mean at height  $h$ . The values  $R/R_0$  were randomly chosen from a normal population with  $M(h) = 1$ ,  $SD(h) = 0.1$ . The functions  $M(h)$  and  $SD(h)$  are shown as dotted curves in Figure 8. The solid curves are the resulting values of the mean and standard deviation of the mean of the quantity  $\sigma(h)/\sigma_0(h)$  where  $\sigma_0$  is the scattering coefficient used in the standard model of Figure 5.

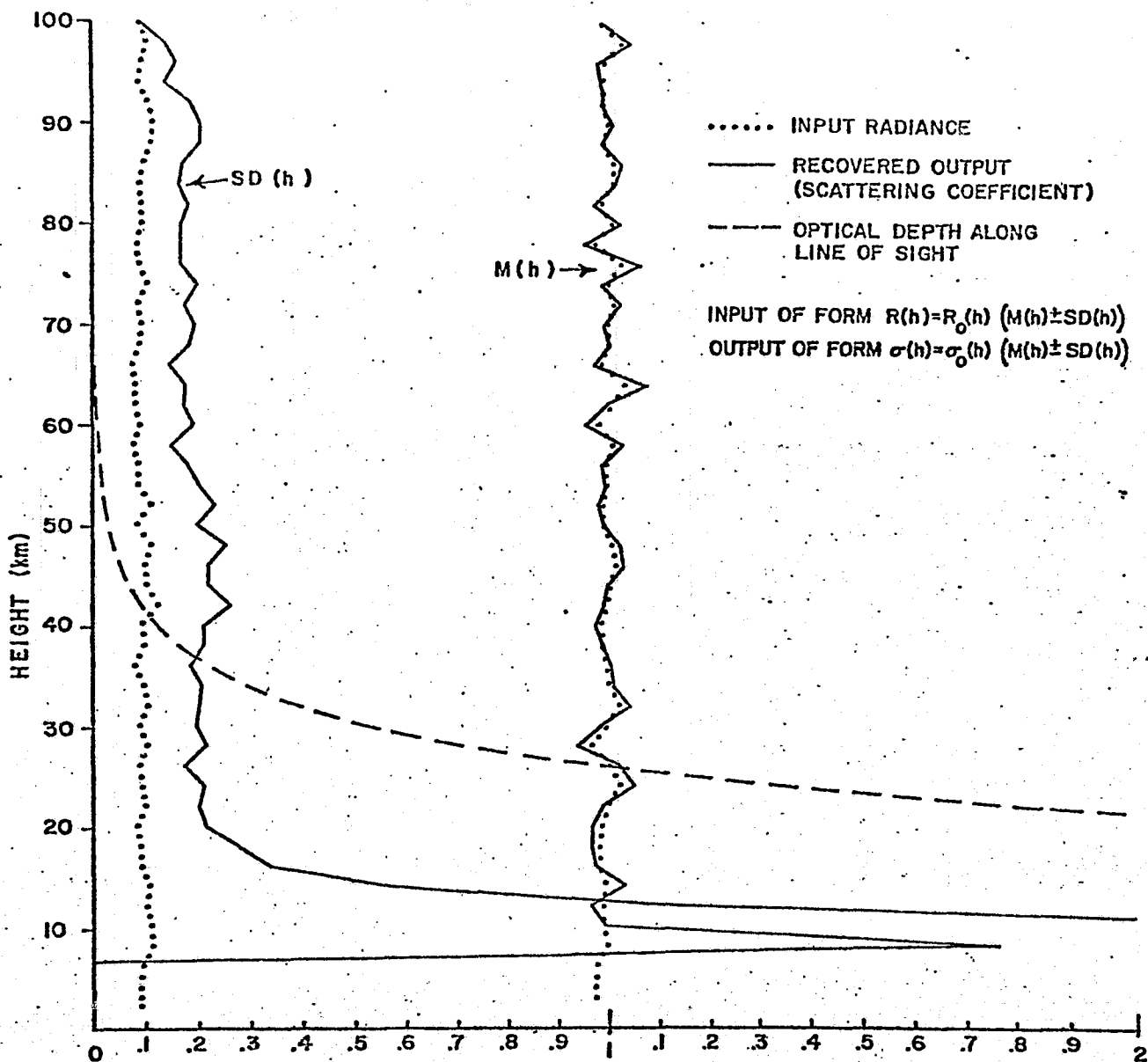


Fig. 3 A noise analysis of the linear method from 50 input radiance profiles. The normalized standard deviation, SD, in the recovered scattering coefficient is twice that of the input radiance down to 20 km.

The dashed curve is the total optical depth along the line of sight. The fact that the means of  $\sigma^{(h)}/\sigma_0^{(h)}$  and  $R(h)/R_0(h)$  correlate to a great extent shows that indeed it is the tangent layer which is the dominant source of the radiance along the line of sight, at least above 20 km. A quantitative measure of the resulting noise in  $\sigma^{(h)}/\sigma_0^{(h)}$  due to the noise in  $R(h)/R_0(h)$  is shown in the comparison of the standard deviations of the means shown in Figure 8. In general, a noise of 10% in the radiance values yields an uncertainty of 20% in the recovered scattering coefficient. Physically, this arises from the fact that along any particular line of sight, the ratio of  $2\tau$  (see Figure 4) to the total optical depth (the dashed curve Figure 8) is about  $\frac{1}{2}$ . Below 20 km, however, the emittance from the tangent layer is attenuated to the point that the observed radiance originates almost totally in the layers above 20 km. Thus, the recovery of information from the lower layers becomes increasingly less certain as is seen by the standard deviation of the mean of  $\sigma/\sigma_0$  in Figure 8. Of interest is the fact that the onset of this uncertainty is very abrupt at 20 km, and above this height, the inversion is extremely stable.

### Conclusion and Summary

The total scattering coefficient as a function of height can be recovered from a direct inversion of the single scattering horizon radiance provided 1) the sun is above the horizon and 2) an independent measurement of the extinction as a function of height is made. The inversion method is stable down to optical depths much greater than unity. The recovered scattering coefficient,  $\sigma(h)$ , has an uncertainty of about twice that of the input radiance,  $R(h)$ , and the relative values of  $\sigma(h)$  are independent of the zero point calibration of  $R(h)$ . Since the inversion of this problem is straightforward and requires little knowledge of the nature of the aerosols themselves, it should be explored in conjunction with iteration schemes to invert the full multiple-scattering problem.

The study of this limited inversion problem also provides an arena for the discussion of measuring techniques. The solar occulting method offers 1) high aerosol sensitivity since measurements are made in the particles' forward-scattering lobe and 2) an opportunity to make near-simultaneous extinction measurements, which, besides being of interest in themselves, make possible a more stable inversion (linear method) of the single-scattering inverse problem. The solar occulting method is restricted to use near times of space-craft twilight.

### Acknowledgements

This work was undertaken in preparation for the analysis of UV limb photographs taken from Skylab under NASA Contract NAS9-12539.

## References

Collins, G. D., Blattner, W. G., Wells, M. B., and Horak, Applied Optics, 11, 2684-2696, 1972.

Gray, C. R., Malchow, H. L., Merritt, D. C., and Var, E. R., Joint Conference on Sensing of Environmental Pollutants, Palo Alto Calif., 1971.

Gray, C. R., Malchow, H. L., Merritt, D. C., Var, E. R., and Whitney, C. K., NASA Contractor Report - CR-112311, 1973.

Greenberg, J. M. and Hong, S. S., Planets, Stars and Nebulae Studied with Photopolarimetry, Gehrels, T. ed., University of Arizona Press, Tucson, 107-134, 1974.

Greenberg, J. M., Wang, R. T., and Bangs, L., Nature, 230, 110-112, 1971.

Huist, H. C. van de, Light Scattering by Small Particles, John Wiley and Sons, New York, 1957.

Kondratyev, K. Ya., Volynov, B. V., Galtsev, A. P., Smoktiy, O. I., and Khrunov, E. V., Applied Optics, 10, 2521-2533, 1971.

Mateer, C. L., Dave, I. V., Dunkelman, L., and Evans, D. C., "Evidence of an Upper Stratospheric Dust Layer in a Satellite Twilight Color Photograph", NCAR ms. 465, 1967.

Minin, N. and Sobolev, V. V., Cosmic Research, 2, 529-537, 1964.

Pepin, T. J., Rosen, J. M., Hofmann, D. J., and Kroening, J. L., International Conference on the Environmental Impact of Aerospace Operations in the High Atmosphere, Denver, AIAA Paper, 73-521, 1973.

Smoktiy, O. I., Izvestiya, Atmospheric and Oceanic Physics, 5, 25-31, 1969.

Volz, F. E., Bull. Am. Meterol. Soc., 52, 996-998, 1971.



ATMOSPHERIC AEROSOLS: RESULTS OF A  
SOLAR OCCULTATION TECHNIQUE FROM SKYLAB

Frank Giovane, Donald W. Schuerman

and

J. Mayo Greenberg

Dudley Observatory

and

The State University of New York at Albany

Albany, New York

Revised: \_\_\_\_\_

## Abstract

A simple coronagraph was modified for use aboard Skylab to photograph the earth's horizon just before spacecraft twilight as a device to monitor the aerosol component of the earth's atmosphere above the tropopause. This coronagraph technique allows one to investigate these high altitude aerosols from a uniquely favorable position--in the particles' forward-scattering cone. The method is thus 10 to 100 times more sensitive than daylight horizon scans made when the sun is well above the horizon. An eight month observing program using seven narrow-band filters was planned. Due to a multitude of spacecraft and equipment mishaps, including the loss of access to the solar-airlock, only one reducible photograph was obtained on a late November (1973) EVA. This particular picture was taken through a  $250\text{\AA}$  bandwidth filter centered on  $3600\text{\AA}$ . Since aerosol layering is detected as an enhancement of radiation above the Rayleigh background, this wavelength region, although free from the spectral influence of ozone, has a relatively high background level compared to longer wavelengths. Even at this high background level, the coronagraph picture provides evidence which is, if not conclusive of, at least consistent with an aerosol layer peaking at  $48 \pm 1$  km. The region photographed was centered on  $26^{\circ}5\text{E}$  longitude,  $63^{\circ}0\text{S}$  latitude. This first observation at high southern latitudes suggests the global nature of the layer.

## Introduction

Inferences of an atmospheric dust layer near 50 km have been reported by many investigators using a variety of techniques. Early LIDAR measurements by Volz and Goody (1962) suggested the possible existence of a layer near this altitude, and, more recently, Clemesha and Nakamura (1972) report LIDAR observations of a 50 km aerosol layer persisting for a few months. Rossler's (1968) rocket observations of diffused skylight also indicated an aerosol layering. Using this rocket data, Elliott (1971) showed that, by making allowance for these aerosols, ozone scale heights as determined by topside sounding could be brought into better agreement with the scale heights measured by other methods. Visual sightings and photographs of a layering phenomena by astronauts aboard Gemini IV have been reported by Mateer, Dave, Dunkelman and Evans (1968). Horizon limb scanning techniques and reduction methods have been developed by the group at Draper Laboratory who have recently published (Cunnold, Gray, and Merritt, 1973) results of horizon scans made from the X-15 high altitude aircraft. One of these scans (at 5800Å) is reported to show the aerosol layering at 50 km. The 20 km layer is also detected at longer wavelengths. The scattering angle in these measurements was about  $120^\circ$ .

In an attempt to investigate the existence of this layer on a global basis, we modified an already existing Skylab airlock coronagraph (i.e. a solar occulter) to take narrow band photographs of the earth's limb just prior to spacecraft twilight. The geometry, nomenclature, and theory appropriate to these observations are described by Schuerman,

Giovane, and Greenberg (1975, referred to hereafter as Paper I). The aerosol component of the atmosphere in this type of horizon radiance measurement is seen as an enhancement of the atmospheric radiance above that predicted by a purely molecular model of the atmosphere. The forward scattering properties of the stratospheric aerosols causes this enhancement to reach a maximum as the scattering (atmosphere-observer-sun) angle becomes as small as possible. For this reason, a solar occulter, on purely geometric grounds, yields a far greater sensitivity to aerosols than measurements made at larger scattering angles. For the characteristic phase function given by Connold et al. (1973), our instrument is a factor of 100 times more sensitive than measurements made at scattering angles greater than  $90^{\circ}$ .

A series of vehicle and on-board equipment failures severely curtailed the original observing program of 300 narrow band photographs to be taken over a period of eight months. The partial loss of the Skylab heat shield immediately after launch and the subsequent erection of a "parasol" on the solar side of the spacecraft prevented the deployment of the coronagraph via the solar-airlock. All observations were then limited to EVA's (extra vehicular activities) on the final Skylab mission.

Several modifications were required to allow the coronagraph to function outside the vehicle. Among these modifications was a shutter speed extension knob, provided by NASA for use with the coronagraph, so that a suited astronaut could change the shutter speed with his gloved hand. On the first EVA, the extension knob became

disengaged from the camera before the full spectral coverage of the atmosphere was completed. However, a photograph centered at  $3600\text{\AA}$  was obtained. On a subsequent EVA, thirty-six pictures of the limb with seven narrow-band filters were taken. Post-recovery development proved all of these frames to be severely out-of-focus. By examining both our data and that of other investigators employing the same camera, we were able to pinpoint the cause of failure to be due to the absence of the camera pressure plate which maintains the film in the focal plane.

The loss of the data in the visible portion of the spectrum was extremely disappointing because the light scattered by the Rayleigh component of the atmosphere (against which the light scattered by the aerosols must be measured) decreases by the fourth power of the wavelength. Thus, the red end of the spectrum is the most sensitive to aerosols. In spite of this loss, the  $3600\text{\AA}$  photograph is of interest because, even at this short wavelength, it yields supporting evidence for a dust layer peaking near 48 km. It also demonstrates the sensitivity of the solar occulting technique, since such a layer would never be visible at this wavelength for horizon scattering measurements not made near the forward direction. Finally, while most other references to the 50 km dust layer refer to the northern hemisphere, this observation was made at a latitude of  $63^{\circ}\text{S}$ , which suggests the global nature of the phenomenon.

The presumed aerosol layering is discernable as a gentle rise above the smoothed signal amounting to a maximum value of about 9% at 48 km. Since this value is near the limit of detectability, a thorough description of both the instrument and the data reduction is presented in the following sections. The discussion is limited to the narrow-band wavelength region centered on  $3600\text{\AA}$ .

### Coronagraph

Newkirk and Bohlin (1963) suggested the design of a coronagraph for satellite and balloon observation that utilized an external multiple disk occulter to achieve high stray light rejection, an improvement on Evans' (1948) original external disk coronagraph. Newkirk and Eddy (1964) flew such a solar occulter with multiple disks and an internal Lyot occulter on a balloon to study the light scattering by particles and molecules in the upper atmosphere, thereby demonstrating the advantage of such a device for atmospheric monitoring. G. Bonner (1972) of the Johnson Space Center, Houston, developed a similar solar occultation device, but without the Lyot occulter, to monitor the particle contamination about the Skylab vehicle for the Skylab T025 experiment. This solar occulter consequently became known as the T025 coronagraph. It utilized three external disks to occult the sun, and although it is not capable of achieving as high a rejection of stray light as Newkirk's or Evans' coronagraph, it was a much simpler instrument. Since it was made to be manually deployed from the solar airlock of the Skylab orbital workshop (OWS), this simplicity was necessary. The occulting disk, being retractable into the main coronagraph housing for stowage, was extended in use by means of a 100 cm long detachable boom. A simple detector system, utilizing a roll film camera in this original design, was used to make non-filtered photographs of particles in the environs of the spacecraft.

The T025 coronagraph was later modified by us to allow the use of narrow-band interference filters and polaroids. The roll film camera

was replaced by a 35 mm Nikon with a pentaprism view finder to provide reflex viewing of the field. This later modification also allowed the use of a UV transmitting lens which was flight qualified and available to fit the Skylab Nikon cameras. Subsequent modifications were necessary so that the coronagraph could be used for EVA's. A supporting bracket enabled the T025 instrument to be attached to a supporting strut of the ATM. This allowed an astronaut to stand just outside the EVA hatch to make observations. A red alignment filter was inserted into the occulting disk to assist the astronauts in pointing the coronagraph to an accuracy of 0.25 degrees. Thermal insulation was incorporated into the EVA package to prevent the battery operated electric Nikon camera from getting too cold. Enlarged controls enabled a gloved astronaut to operate the camera. Dulling of the occulting disk's edges was required to prevent possible damage to the astronaut's space suit or umbilical from these blade like structures.

The final configuration of the T025 Coronagraph as launched on the last Skylab mission is illustrated in Fig. 1. The coronagraph in this final form functioned well according to Pogue, Gibson, Carr (1974) on its 4 EVA's. The only failures were in the Nikon camera as previously noted. The coronagraph measures 28 x 28 x 24 cm in the stowed configuration and has a mass of 8.2 kg. In the deployed condition the 13.3 cm diameter occulting disk subtends approximately 7.0 degrees, well over-occulting the sun and placing the coronagraph optics completely within the disk's penumbra. The field of view is limited by the canister baffle to approximately 25.7 degrees.



The optical system is simple. It is composed of a view window (a vestige of when an air seal between the OWS and space was required), narrow-band interference filters, lens, and photographic detector. The 7.0 cm diameter view window was made of 1.2 cm thick Suprasil (Amersil, Inc., Hillside, New Jersey), a low fluorescence UV transmitting glass. To facilitate rapid filter changing, the filters were contained in trays holding four filters each. The filter trays were inserted into a filter tray slide located in front of the camera lens. This tray slide utilized a light sealing detent system to position the filters and seal out stray light. The  $3600\text{\AA}$  filter, manufactured by Corion Instrument Corp., with a central wavelength of  $3560\text{\AA}$  at  $7^\circ$  angle of incidence and a half power bandwidth of  $270\text{\AA}$ , was blocked outside of the passband (defined as the 10% of peak transmission bandwidth). The solar spectral radiance distribution between  $1800\text{\AA}$  and  $7000\text{\AA}$ , convoluted with the filter transmission, results in the total power transmitted in the passband exceeding the power transmitted outside the passband by a factor of over 50. The  $3600\text{\AA}$  filter, which was epoxy cemented, showed little significant internal scattering (ghosting) and did not show any significant deterioration over the course of its use.

The lens, a 27 mm aperture Nikon UV 12 element achromat of 55 mm focal length, was developed by Nippon Kogaku, Inc., Japan, for the Skylab S063 UV Airglow Horizon Photographic Experiment and was fixed focused at infinity. This lens' 81% transmission, its resolution of greater than 55 line pairs/mm at  $3600\text{\AA}$ , and its availability as flight qualified hardware recommended its use. It was mounted to the coronagraph canister by

an adapter which screwed into the filter thread of the lens. A sleeve fitting to the canister allowed easy removal of the camera-adapter for stowage. The lens, because of its multiple-element construction, had a significant amount of internal scatter when illuminated near its edge.

The camera used with the 27 mm lens was a motor driven Nikon F2 Photomic. Although essential for EVA operation, the motor driven Nikon required thermal protection for its battery and motor, and it transported the photographic film at a high speed which resulted in some cases in emulsion cracking and static discharge marks.

The film, 35 mm Kodak Tri-X Aerographic (2403) ester base with ram jet backing, was processed to achieve optimum latitude, speed, and resolution. The resulting D-Log E curve is illustrated in Figure 2. Although the background fog level of the film, due to the 2.1 rad of radiation experienced in space, is high (density = 0.8), the usable latitude nonetheless exceeded  $10^3$ . The flight film was calibrated both before and after flight with absolute sensitometric step wedges and was processed with film strips containing reciprocity and spectral sensitometric calibration wedges.

### System Response and Conversion to Absolute Radiance

The overall response function of the instrumental system when used with the 3600Å filter is illustrated in Figure 3. This function is the convolution of the view window, UV lens, and 3600Å filter transmissions,  $T_w(\lambda)$ ,  $T_L(\lambda)$ , and  $T_F(\lambda)$ , respectively, with the effective film spectral sensitivity factor,  $\sigma'(\lambda)$ , and the spectral radiance distribution of the atmosphere,  $B_A(\lambda)$ . The value of  $B_A(\lambda)$  over the short interval of the system response was taken equivalent to the solar radiance distribution. The effective film spectral sensitivity factor is defined in terms of the relative spectral sensitivity,  $\sigma(\lambda)$ , as measured from the sensitometric step wedge by:

$$\sigma'(\lambda) = \sigma(\lambda) \frac{\int B_S(\lambda) d\lambda}{\int \sigma(\lambda) B_S(\lambda) d\lambda} \quad (1)$$

where  $B_S(\lambda)$  is the spectral distribution of the 5500 K color irradiance used to calibrate the film and from which our D-Log E relationship was derived.

Additionally, we can derive an effective system bandwidth,  $\Delta\lambda$ , which can be considered as an interval over which the system's transmission and the film's spectral sensitivity factor can be taken as one, and the radiance spectral distribution normalized to the radiance at the central wavelength of the system. This can be represented for the 3600Å filter by

$$\sigma'(\lambda) = \frac{\int B_A(\lambda) \sigma'(\lambda) T(\lambda) d\lambda}{B(3600)} = 64.5 \quad (2)$$

where  $T(\lambda) = T_w(\lambda) T_L(\lambda) T_F(\lambda)$ .

The density corresponding to an area of the film,  $i$ , is related to the energy,  $E_i$ , incident on that area through the D-Log E relationship. The value of  $E_i$  is converted to the radiance of the corresponding spatial area of the radiation source,  $R_i$ , by taking into account: the exposure time,  $t$ ; the film reciprocity,  $p(t)$ ; the lens focal length to aperture ratio  $f/a$ ; the vignetting function,  $V(\rho)$ ; background signal level,  $E_b(\rho, \theta)$ ; and the effective system bandwidth,  $\Delta\lambda$ . This conversion is given by

$$R_i = \frac{4}{\pi} \left( \frac{f}{a} \right)^2 \frac{E_i - E_b(\rho_i, \theta_i)}{t p(t) V(\rho_i)} \quad (3)$$

where  $\rho_i$  and  $\theta_i$  are radial and azimuthal angles, respectively, of the area  $i$ .

This numerically reduces to

$$R_i = 1.47 \frac{(E_i - E_b(\rho_i, \theta_i))}{V(\rho_i)}$$

for the 3600Å observation which was taken at  $f/a=2$  and  $t = 0.0619$  sec.

### Background Signal Level

The background signal resulting from stray light in the coronagraph system is dependent on the position  $\rho, \theta$  in the field. Several factors associated with the EVA observations of the earth's atmosphere increased this background level. The dulling of the occulting disk edges and direct earth light entering the coronagraph are obvious examples. Reflections of sun light from the ATM housing, from supporting struts and cables, and from the astronaut operating the coronagraph also contributed. Since the coronagraph was constructed to prevent scatter only from direct sun light, few baffles existed to prevent indirect light from entering the system and scattering. In addition, limitations inherent in EVA operation restrict the pointing precision of the coronagraph to about  $\frac{1}{4}$  of a degree. The sun was consequently off center which resulted in a reduction of the effectiveness of the occulting disks. The net increase in stray light was found to be about 15 times greater than that predicted by laboratory measurements on the unmodified coronagraph. This increased the ratio of background radiance to average solar disk radiance at  $3600\text{\AA}$  (rejection factor,  $G$ ) to a minimum of  $1.02 \times 10^{-8}$  at 7.1 degrees from the optical axis.

The determination of  $E_b$  as a function of  $\rho, \theta$  could not be determined from the limited amount of returned data. However, by assuming axial symmetry, a radial dependence for  $E_b$  was approximated as shown in Figure 4. There  $E_b$  has been normalized to the solar value.

This relationship was obtained from areas of the film near the earth's atmosphere but above the 100 km layer. At this altitude, the atmosphere should produce no detectable signal.

### Errors Associated with Absolute Radiance Determination

The error associated with the determination of the absolute radiance is dependent on the uncertainty of the terms in equation 3. The degree of uncertainty for each of these terms is not precisely known, but rough estimates can be made. The background signal  $E_b(\rho, \theta)$  is a principal contributor to the error only for very low signal levels. The uncertainties in the determination of  $E_i$  and its associated reciprocity function  $p(t)$  are more complex.  $E_i$  and  $p(t)$  are based on several factors including: the calibration of the sensitometer, the accuracy of the microdensitometer, the goodness of the polynomial fit to the D-Log E curve, and the representativeness of the calibration film stepwedges (which was placed on the film before and after launch). An estimate, based on various tests, indicates that this uncertainty does not exceed 25% for the determination of  $E_i$  in the linear region of the D-Log E curve. Major uncertainties also exist in the value of  $t$  which was determined from pre-launch calibration of the shutter speed. Based on measurements of the solar disk present in some of the other EVA photographs, this uncertainty should not exceed 20%. The uncertainty in  $\Delta\lambda$  can amount to 20% and is due almost entirely to inaccuracies in the calibration of the spectral response of the film rather than to the lens and filter transmissions which are well known. The uncertainty in  $V()$  is relatively small, and probably does not exceed 10%. The error associated with  $f/a$  is due to the difference between the nominal setting of the lens iris stop and the actual value of aperture. This difference was incorporated into the value of  $T_L$  and is therefore accounted for.

Therefore, the total systematic error in the determination of the absolute value of  $R_i$  should roughly be less than 40%.



## Reduction

The photograph of the earth's horizon at  $3600\text{\AA}$  is shown in Fig. 5. The earth is seen as the well exposed portion of the frame near the bottom. The extension boom supporting the occulting disk is the light area near the top of the frame. On the left is an insert of a microdensitometer raster which clearly defines contours of equal density. The geometry used in this reduction is defined in Paper I. The position of the sun behind the occulting disk is known (from pictures taken a short time earlier without the  $3600\text{\AA}$  filter) to within a minute of arc, and the vertical direction is defined by the axis of the symmetry of the limb contours. One degree of arc in this photograph corresponds to about 40 km near the earth's limb. Nine slices of the atmosphere perpendicular to the limb were selected for detailed investigation. The nine areas include a center slice (not shown), the regions labeled 1 through 4 in the figure, and four similar cuts (not shown) on the right side of the axis of symmetry. Each cut differs from the adjacent one by about  $1^\circ$  in scattering angle, ranging from  $5.93^\circ$  for the center slice to  $9.93^\circ$  for the slice numbered 1 in the figure. (The angles mentioned here refer to the angles from the sun to the 40 km layer of the atmosphere within each slice.) All geometric factors, which include the camera plate scale, the spacecraft orbit, the time at which the picture was taken, and the position of the axis of symmetry, were known to a precision which allows the limb of the earth to be located within  $\pm 1$  km.

A Spec - Scan 3000S microdensitometer with a square aperture corresponding to  $1.44 \times 10^{-6} \text{ deg}^2$  on the photograph was used to raster scan the film and digitally record its density. Initial attempts to directly convert the density of individual pixils to energy incident on the film were not successful as individual values of the measured density occasionally exceeded the range of the D - Log E relationship. This problem was particularly severe at high density levels near saturation of the D - Log E curve. To overcome this problem, we synthesized a larger scanning aperture by converting the density to opacity and averaging the opacity of about 160 pixils. The synthesized aperture corresponds to a horizontal layer of the atmosphere about 1 km thick and 40 km wide. Thus, the slice labeled 1 in Fig. 5 consists of about 150 apertures, each aperture as wide as the slice, stacked on top of one another and identified by their height above (below) the limb. Each aperture has an average opacity and standard deviation about the mean. These mean opacities and their uncertainties were then converted back to density and then to incident energies ( $E_i$ 's) and finally to incident radiances ( $R_i$ 's) via equation 3.

As a first approximation to separating the background from the atmospheric signal, a constant value of  $E_b$  was found for each of the nine cuts up through atmosphere by averaging the radiances of the apertures between 100 and 130 km. Each background was subtracted from all the radiance values within its respective cut. Because of the stray-light problems mentioned in the previous section, it was felt that further attempts to separate the signal from the background by using positionally

dependent values of  $E_p$  would be presumptuous.

An intercomparison of radiance vs height plots for each of the nine cuts showed all curves to be identical within the noise limits established from pixel averaging. We show in Fig. 6 the results of combining all nine plots. The horizontal bars at each height show the standard deviation of the mean radiance. Thus, the value of the mean radiance and its uncertainty as obtained from about 1400 pixels is shown for each height in 1 km increments. The placement of the observational curve on the absolute abscissa scale is accurate to 40% as discussed in the previous section. Also presented is the profile predicted from single-scattering theory. The profile presented here is for clean air based on the mean U. S. standard atmosphere (1962). The shift between the two curves is primarily due to multiple scattering effects as discussed by Gray, Malchow, Merritt, Var and Whitney (1973). A more detailed comparison can be seen in Fig. 7 where the observed data is normalized to the single-scattering profile. The dots represent the one sigma uncertainty levels. This noise is largest in the 20 km region because the D - Log E curve nearly saturates at these high density levels. Some of the uplift of the curve near 70 km reflects the background-level problem mentioned earlier. Of greatest interest is the readily detectable hump-like feature centered at 48 km and apparently extending from 45 to 54 km. This feature occurs where the signal to noise is relatively very good ( $\geq 25$ ), and over a range of about 9 km it is persistently higher than a smoothed atmospheric profile. Many of the points comprising this feature are 2 to 5 sigma removed from a smoothed curve.

We cannot explain the hump as being instrumental in nature. Studies of the diffuse background in other portions of the film always show the background-level to be a small, smoothly varying function incapable of producing such a hump. In order to insure that the hump-like feature was not the result of a large spurious effect in a small region of the film, the nine slices were combined into three sets representing the central, left, and right-hand portions of the atmosphere. Each set appears to equally contribute (within the noise limits) to the phenomenon throughout the 45 to 54 km layers. This means that this small contribution of increased light has the shape of the horizon. In a series of laboratory tests using simulated horizons, we have been totally unable to produce a stray or scattered light effect in the instrument which conforms to the shape of the horizon.

Since normalization of the curve in Fig. 6 is dependent upon the density profile assumed in the single scattering calculation, we next examined the effect that a different density profile would have on the hump. (The background-level problem mentioned earlier prevents us from attempting the inversions for the density profile as developed in Paper I.) The picture was taken on November 22, 1973. The limb in the center of the picture has geocentric coordinates of  $26^{\circ}5'E$ ,  $63^{\circ}0'S$ . Because of the lack of information on atmospheric structure at high southern latitudes, we renormalized the observations to a single-scattering model based on the density profile of the standard U.S. atmosphere (1966)  $60^{\circ}N$ , July. The result of this renormalization is shown in Fig. 8. Although the general shape of the curve changed somewhat, the hump remains an

identifiable feature. Without additional wavelength information, we cannot absolutely rule out the possibility of a density deviation from the standard atmospheres which would give rise to such a hump. A 10% density increase centered over the 9 km region is required. From the general trend of errors discussed in the U. S. Standard Atmosphere Supplements, 1966, such a deviation seems unlikely.

Finally, the work of Gray et al, (1973) shows no indication of multiple-scattering being responsible for this hump at this wavelength.

### Conclusion

We presently believe the hump provides additional evidence for an aerosol layer peaking at  $48 \pm 1$  km. The layer appears to be about 10 km thick. At an average scattering angle of about  $8^\circ$ , the hump appears as an 8% to 10% enhancement above the smoothed atmospheric radiance. An otherwise perfectly clean atmosphere would require a concentration of roughly  $0.01 \text{ cm}^{-3}$  particles of radius  $0.1 \mu\text{m}$  to yield such an effect. This number is consistent with inputs used in recent model calculations (for example, McClathey, Fenn, and Selby, 1972). for a relatively clean atmosphere.

While the lack of information at longer wavelengths prevents any detailed analysis of the nature of the aerosols (including the absolute certainty of the existence of the layer), the present data provides evidence for the global nature of the layer since this is the first observation made at extreme southern latitudes. The power of the daylight occulting method is also demonstrated. Even against the high Rayleigh background encountered at  $3600\text{\AA}$ , the aerosol's forward-scattering properties make the coronagraph technique an extremely sensitive method of remote aerosol detection. At longer wavelengths, with the molecular scattering dropping off like  $\lambda^{-4}$ , we would expect the signature of the high aerosol layer to be many times that of the 8% to 10% level found in this investigation. On the other hand, it is doubtful whether this layer could be detected at all (at any wavelength) from horizon scans made at appreciably larger scattering angles.

## References

- Bonner, G., Private communication, 1972.
- Clemesha, B. R., and Nakamura, Y., Dust in the upper atmosphere, Nature, 237, 328-329, 1972.
- Cunnold, D. M., Gray, C. R., and Merritt, D. C., Stratospheric aerosol layer detection, J. Geophys. Res., 78, 920-931, 1973.
- Elliott, D. D., Effect of a high altitude (50 km) aerosol layer on topside ozone sounding, Space Res., 11, 857-861, 1971.
- Evans, J. W., A photometer for measurement of sky brightness near the sun, J. Opt. Soc. Am., 38, 1083-1085, 1948.
- Gray, C. R., Malchow, H. L., Merritt, D. C., Var, E. R., and Whitney, C. K., Aerosol physical properties from satellite horizon inversion, NASA CR-112711, National Aeronautics and Space Administration, Washington, D. C., 1973.
- Mateer, C. L., Dave, I. V., Dunkelman, L., and Evans, D. C., Twilight colors seen from space, NCAR Quart., 20, National Center for Atmospheric Research, Boulder, Colorado, 1968.
- McClathey, R. A., Fenn, R. W., and Selby, J. E., Optical properties of the atmosphere, 3rd ed., AFCRL-72-0497, Air Force Cambridge Research Laboratories, Bedford, Mass., 1972.
- Newkirk, G. Jr., and Bohlin, D., Reduction of scattered light in the coronagraph, Appl. Opt., 2, 131-140, 1963.
- Newkirk, G. Jr., and Eddy, J. A., Light scattering by particles in the upper atmosphere, J. Atmos. Sci., 21, 35-60, 1964.
- Pogue, W. R., Skylab 1/4 corollary experiments debriefing, JSC-08814, National Aeronautics and Space Administration, March 4, 1974.
- Rossler, F., The aerosol layer in the stratosphere, Space Res., 8, 633-636, 1968.
- U. S. Standard Atmosphere, 1962, Washington, D. C., U. S. Government Printing Office.
- U. S. Standard Atmosphere Supplements, 1966, Washington, D. C., U. S. Government Printing Office.
- Volz, F. E., and Goody, R. M., The intensity of the twilight and upper atmospheric dust, J. Atmos. Sci., 19, 385-406, 1962.

## Figure Captions

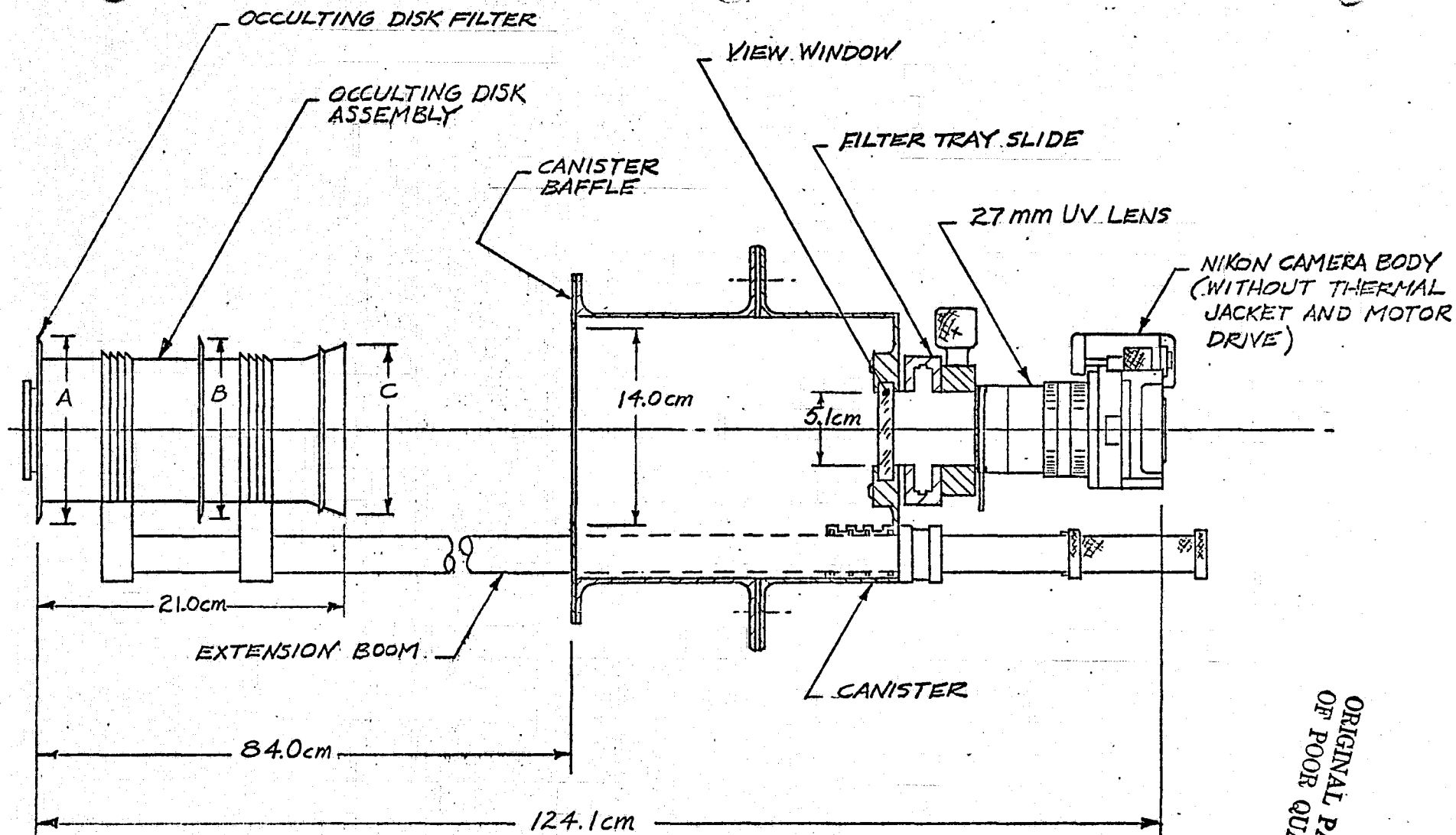
- Fig. 1 The T025 coronagraph in its deployed configuration. The three external disks A, B, and C are used to occult the sun and reduce defracted light. The coronagraph optics are located so that they lie completely within the penumbra of the disks when the coronagraph axis is aligned with the sun's direction.
- Fig. 2 The D-Log E curve fitted to the prelaunch sensitometric step wedge of the flight Tri-X Aerographic Film.
- Fig. 3 The total system spectral response with the  $3600\text{\AA}$  filter.
- Fig. 4 The Coronagraph system (with  $3600\text{\AA}$  filter) rejection factor vs. angular distance from frame center. This determination utilized areas of the film near but above the earth's atmosphere to obtain the background level. It is normalized to the unocculted solar image to obtain the rejection factor,  $G$ . The frame center is defined by the known position of the sun behind the occulting disk.
- Fig. 5 The earth's limb at  $3600\text{\AA}$  as viewed through the coronagraph. The insert on the left is a coarse microdensitometer tracing which highlights contours of equal density. The numbered strips show four of the nine areas selected for detailed analysis. The width of each strip corresponds to about 40 km at the earth's limb. A structural member of the spacecraft can be seen in the upper right-hand corner.
- Fig. 6 The combined observations of nine selected areas with statistical error (one standard deviation) bars. A single-scattering profile, using the mean U. S. standard atmosphere, is also presented. Most of the shift between the two curves is attributable to multiple scattering. The systematic error in the absolute calibration of the observations (affecting only the placement of the data curve along the abscissa) is less than 40% in R.



Figure Captions - continued

Fig. 7 The data contained in Fig. 6 but normalized to the single-scattering profile. Each pair of dots represent the standard deviation of the mean from about 1400 pupils. The broad hump-like feature centered on 48 km is interpreted as being due to aerosols.

Fig. 8 The effect of normalizing the observations to a different single-scattering profile. The feature at 48 km remains prominent despite the change in the general shape of the curve.



DIMENSION	DIA. (cm)
A	13.3
B	12.7
C	12.0

Fig. 1

ORIGINAL PAGE IS  
OF POOR QUALITY

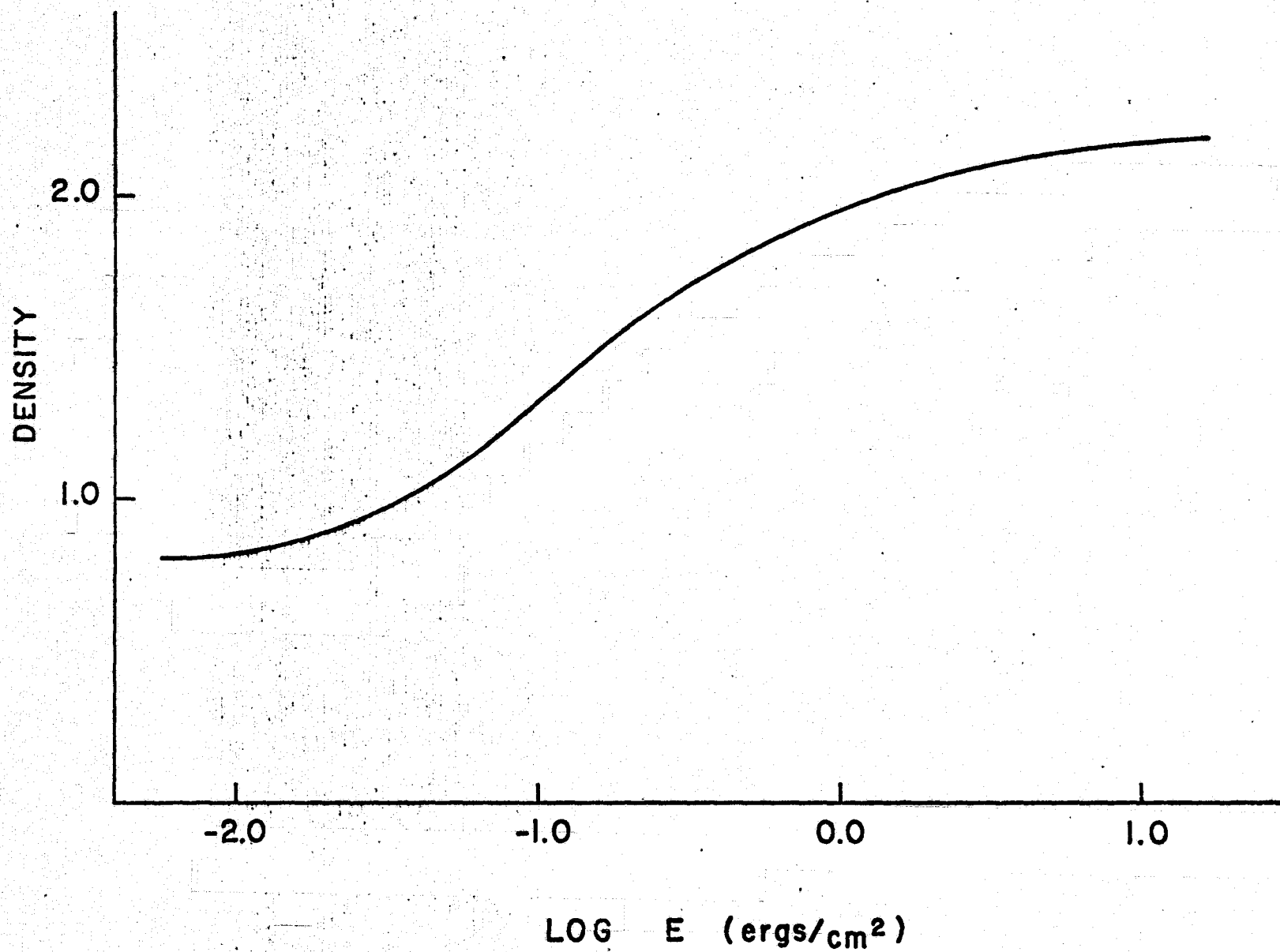


Fig. 2

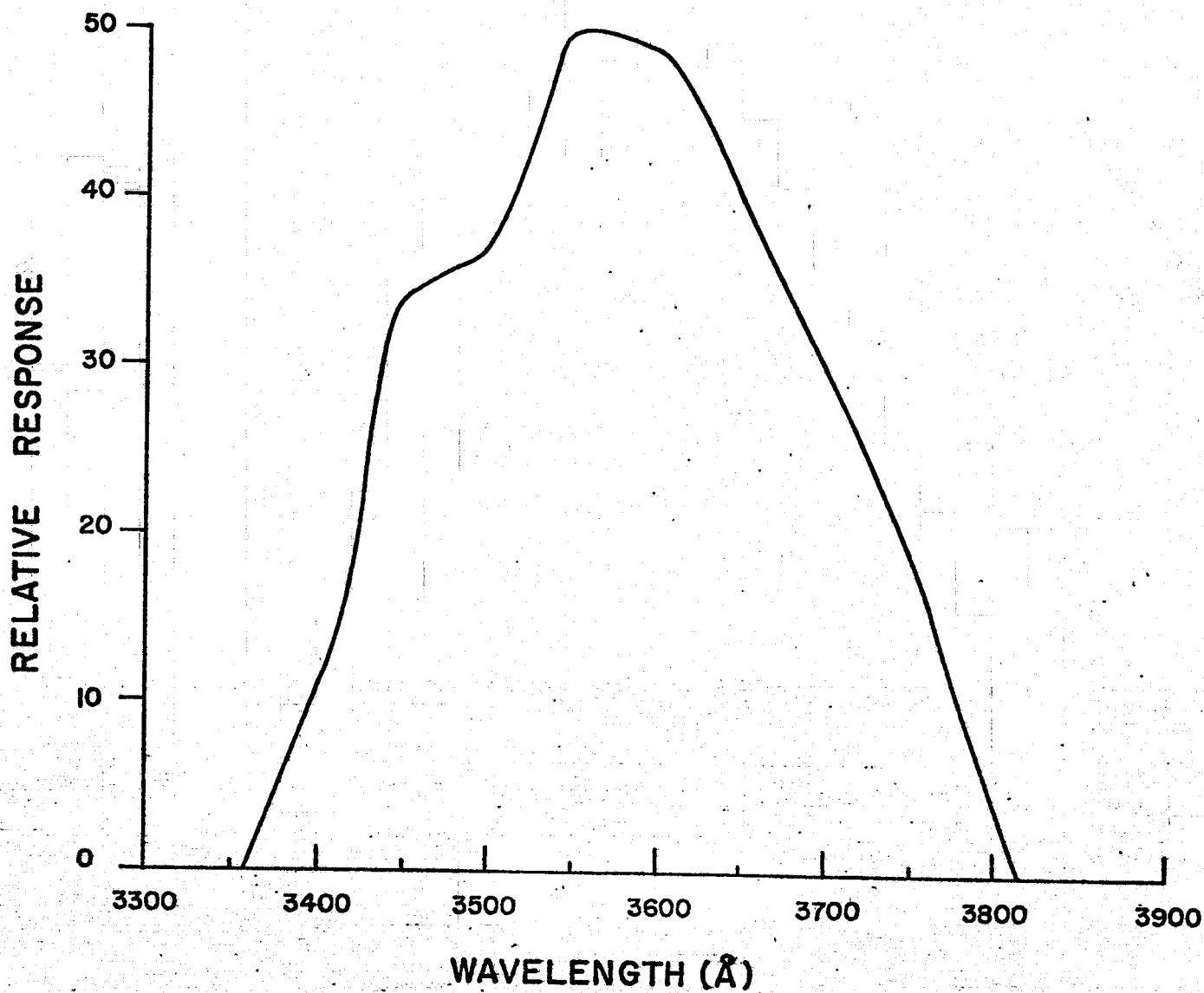


Fig. 3

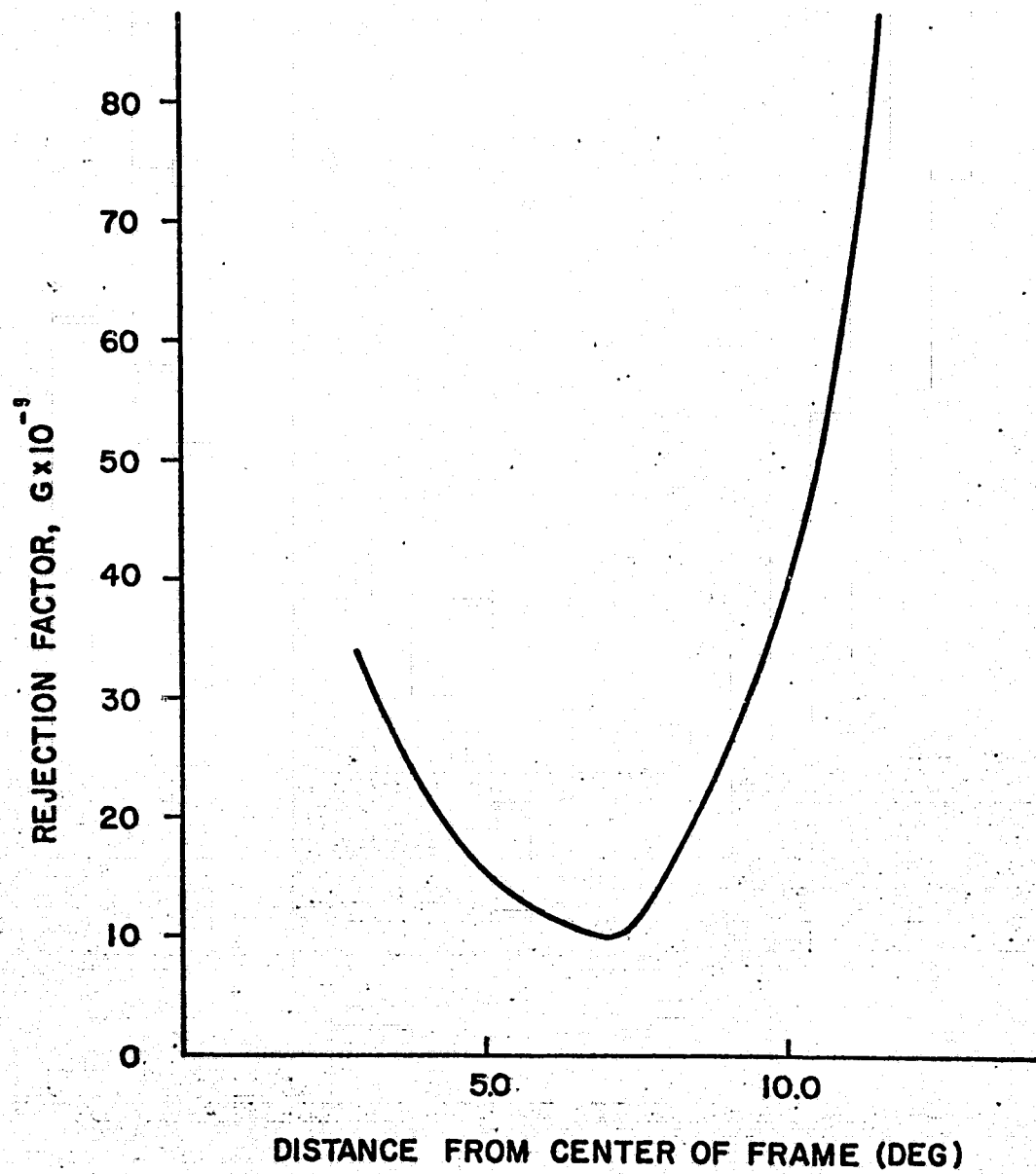
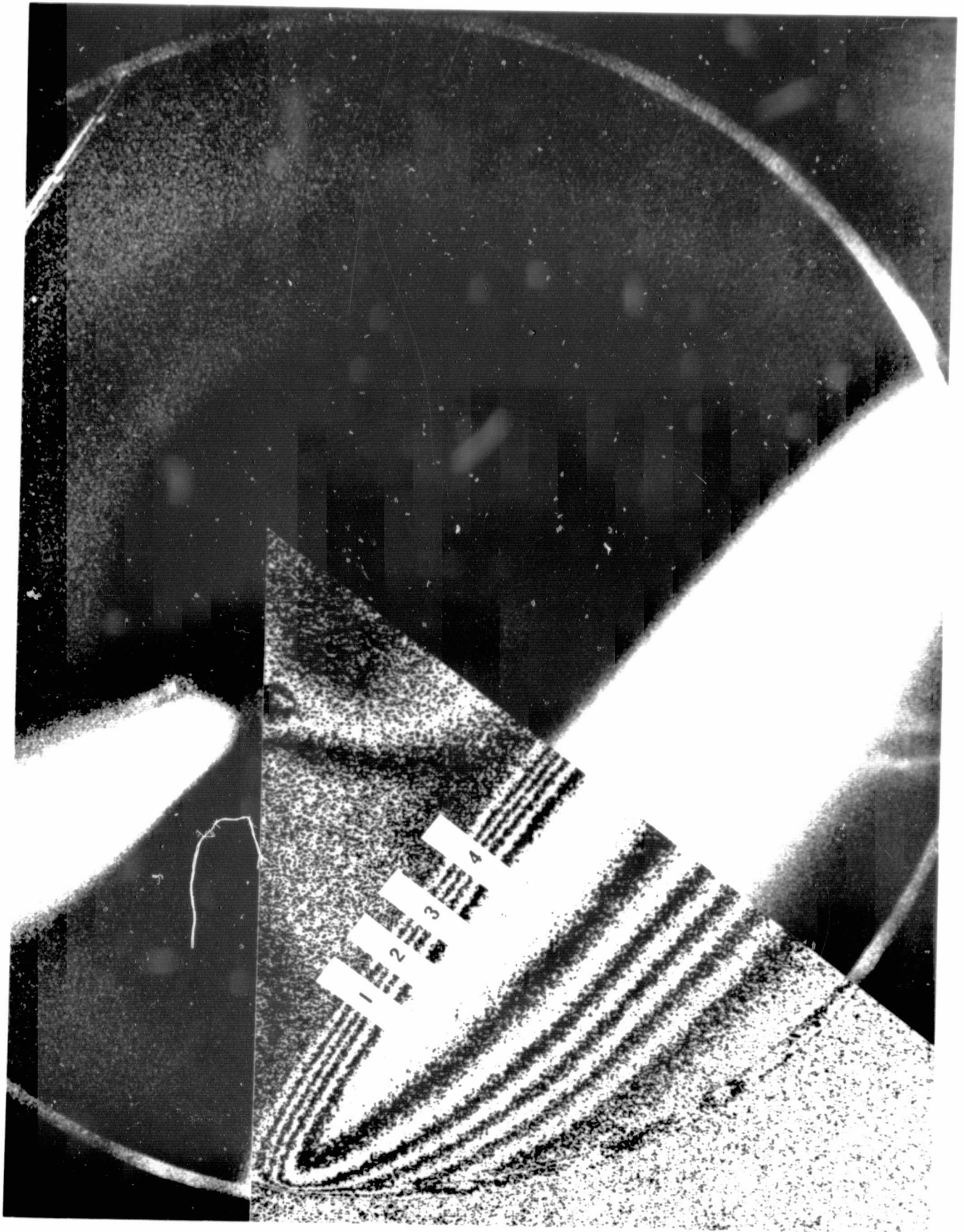


Fig. 4

ORIGINAL PAGE IS  
OF POOR QUALITY



ORIGINAL PAGE IS  
OF POOR QUALITY

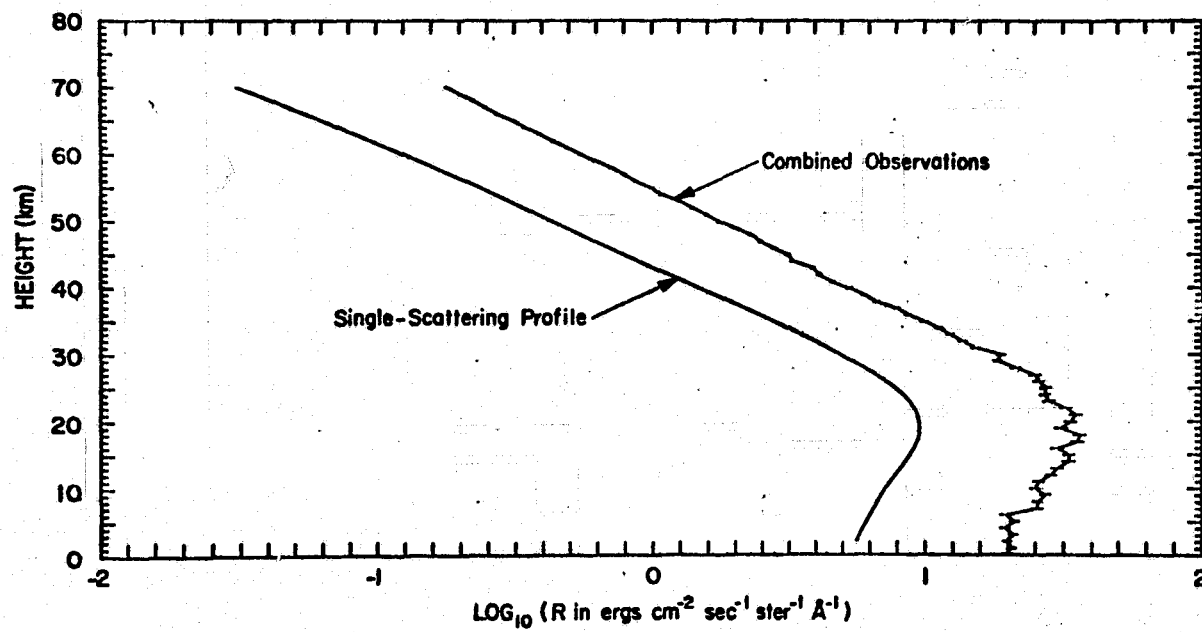


Fig. 6

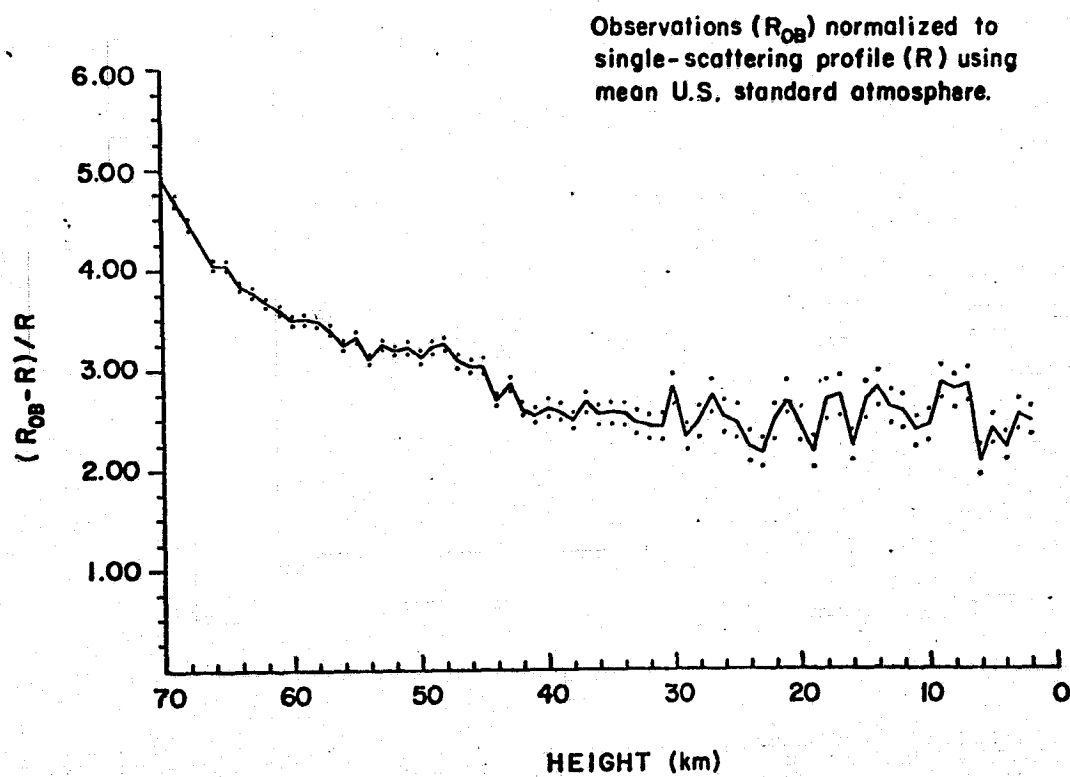


Fig. 7



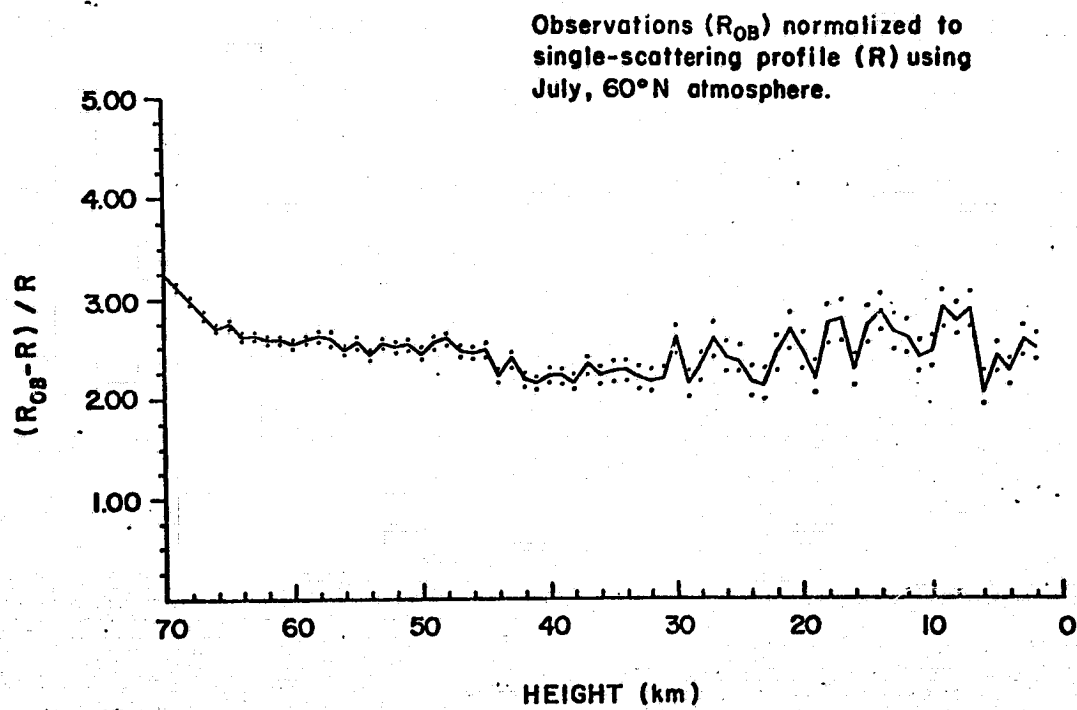


Fig. 8

## VII MICROWAVE LABORATORY

### Microwave Scattering Laboratory

The Microwave Scattering Laboratory (MSL), a subdivision of the Laboratory for Particle Scattering occupies a 75' x 40' x 14.5' section of a thermally controlled, vibrationally isolated building on the grounds of the Dudley Observatory. In this facility, problems involving the scattering of visual light by micron and submicron particles are scaled to the region of microwave radiation so that scattering targets of the order of centimeters can be machined and fabricated. Figure 1 shows part of the interior of the large anechoic chamber in which the scattering measurements are made. Bi-static antennas are used for the transmission and reception of incident and scattered signals. Both forward scattering and angular distribution measurements can be made. For backscattering measurements, a mono-static antenna is used for both transmitting and receiving. A unique design of continuous-wave cancellation allows the radiation in the forward scattering cone of a target to be separated from the background radiation of the transmitter so that small scattering angles can be investigated. The target is supported by thin nylon threads which control the particle orientation with respect to the incident wave. The polarization of both the transmitting and receiving antennas can be varied continuously and independently through the use of rotary waveguide joints. A stable, precise antenna sweep mechanism and associated circuitry has been constructed to expedite angular-distribution measurements. The chamber also houses the necessary microwave and electronic circuitry for data display, and storage. A number of computer programs and a teletype

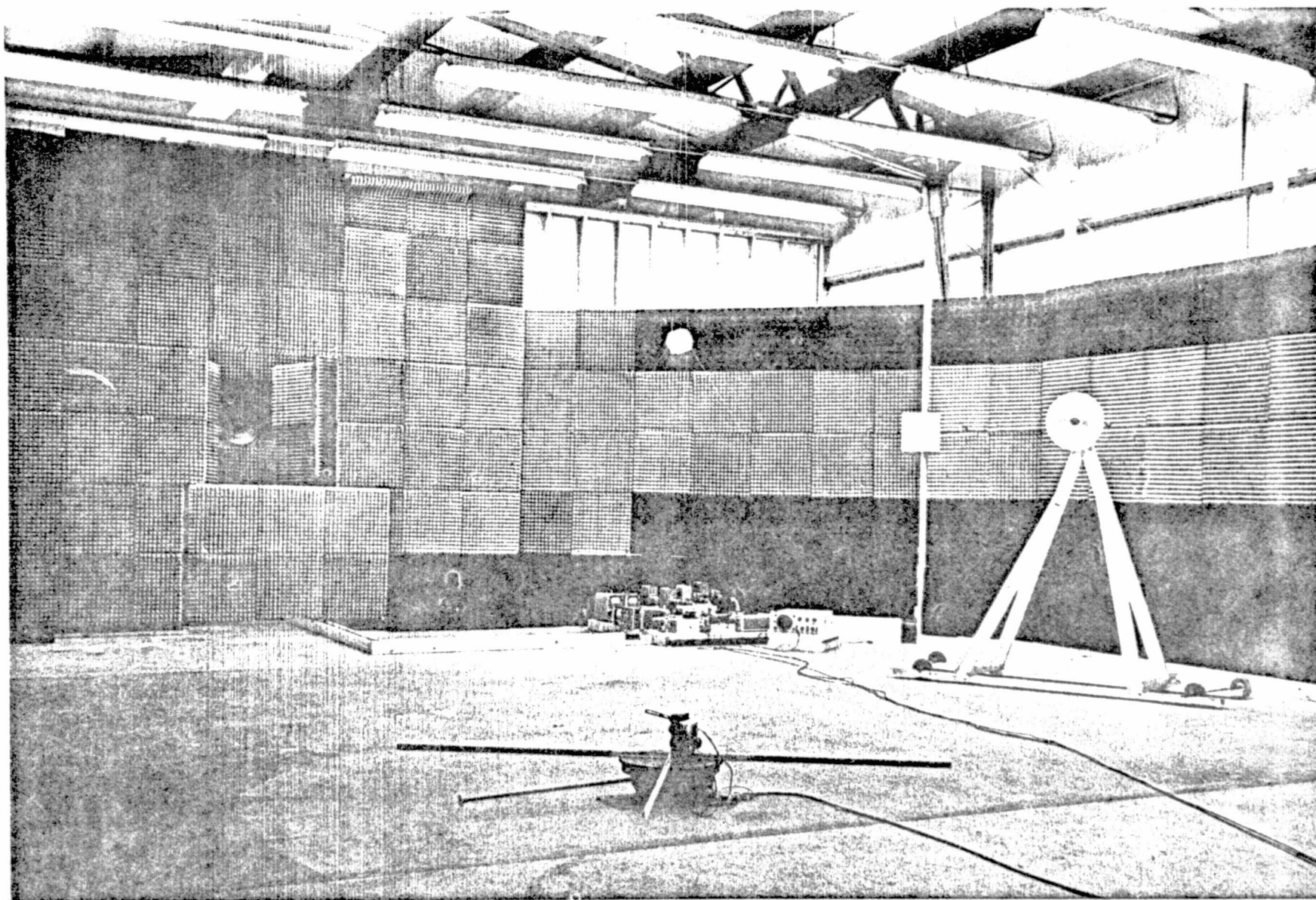


Fig. 1      Microwave Scattering Laboratory  
in the Laboratory for Particle Scattering  
at Dudley Observatory

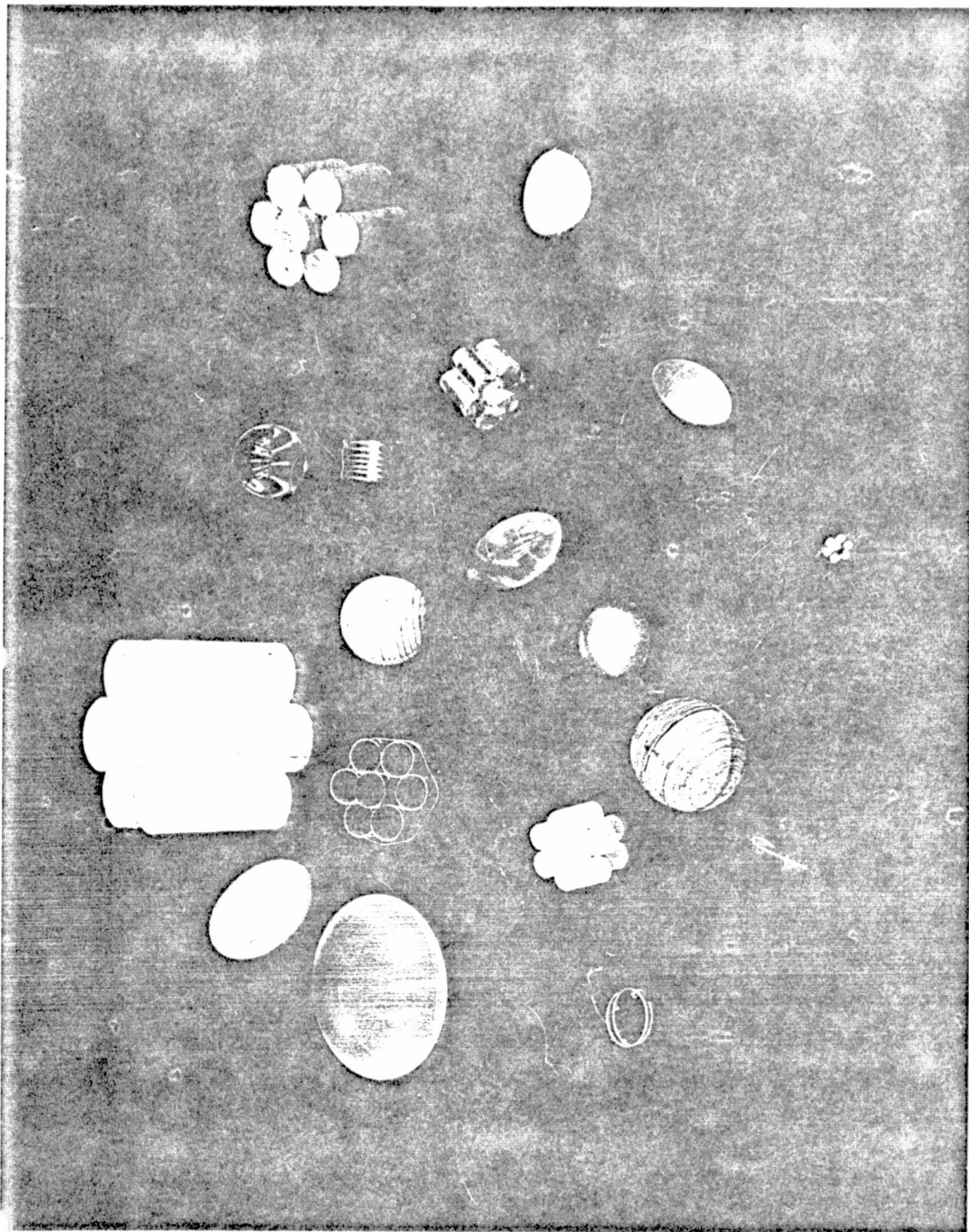


Fig. 2 Non-Spherical Targets (one half true size)

terminal to an UNIVAC 1110 computer facilitate the calibration of the system, data reduction, and wave front examinations.

Typical targets whose scattering properties have been determined are shown in Figure 2. Particles of arbitrary shape can be investigated by machining or molding equivalently shaped targets. The target material is selected by requiring it to have, in the microwave region, the same properties (dielectric constant and conductivity) that the particle to be investigated has in the visible wavelength region. By controlling the density of soft expandable plastics like polystyrene, any of a wide variety of indices of refraction can be duplicated in a casting. The absorptivity is controlled by the proper admixing of conducting inclusions such as carbon. Hundreds of such targets have been systematically manufactured. The constantly expanding market of castable chemical liquids provides an almost unlimited range of optical properties for target simulation.

The laboratory also contains the facilities to measure precisely the refractive index of target material. Both the real and imaginary parts of the index are measured via the waveguide-slotted-line method of Roberts and Von Hippel.

The following paper contains the results of an investigation of non-isotropic spheres. This project was continued under the T025 contract because of its importance in interpreting light-scattering effects observed in comets and atmospheric aerosols.

# PRELIMINARY

## SCATTERING BY SPHERES WITH NONISOTROPIC REFRACTIVE INDICES

R. T. Wang and J. M. Greenberg

Dudley Observatory

and

The State University of New York at Albany

Albany, New York

Received: \_\_\_\_\_



## Scattering by Spheres with Nonisotropic Refractive Indices

R. T. Wang and J. M. Greenberg

## Abstract

Some results of experimental studies on microwave scattering by artificially constructed axially symmetric spheres with anisotropic refractive indices are presented. An approximation using Mie Theory for spheres with appropriate orientation dependent indices of refraction, is shown to provide a good explanation of the observed dependence of the complex forward scattering amplitudes on target orientation.



Introduction

Despite the long history of single-particle electromagnetic scattering studies by a number of people working in a wide range of disciplines, little is known about the problem of scattering by anisotropic spherical particles whose sizes are of the order of the wavelength  $\lambda$  of the radiation. Aside from the difficulty involved in a theoretical approach alone, there are few experimental methods which may be used to obtain any systematic results. It is the purpose of this paper to report some experimental results using the microwave analog technique (Lind et al. 1965). We shall also describe a theoretical approximation for the subtle change in the forward-scattering amplitude and phase as the orientation of the target is varied.

Some Symmetry Relations and the  
Theoretical Basis for the Scattering Measurement

We shall generally follow the notations of van de Hulst (1957) to describe the various scattering quantities. The elements of the scattering amplitude matrix  $\tilde{S}$ , all dimensionless complex numbers, relate the complex amplitude of the incident wave  $\vec{E}_0 = \begin{pmatrix} E_{|0} \\ E_{r0} \end{pmatrix}$  and the scattered wave  $\vec{E} = \begin{pmatrix} E_{|} \\ E_{r} \end{pmatrix}$  in the following way:

$$\vec{E} = \frac{\exp(-ikr+ikz)}{ikr} \tilde{S} \cdot \vec{E}_0 = \frac{\exp(-ikr+ikz)}{ikr} \begin{pmatrix} S_2 & S_3 \\ S_4 & S_1 \end{pmatrix} \begin{pmatrix} E_{|0} \\ E_{r0} \end{pmatrix} \quad (1)$$

where  $k = 2\pi/\lambda$  and the time factor  $e^{i\omega t}$  is omitted. Suffixes  $|$  and  $r$  denote the components of the electric field parallel and perpendicular to the scattering plane, which is formed by the incident ray and a scattered ray passing through the observation point  $P$  at a large distance  $r$  from the scatterer (cf. Fig. 1). In Fig. 1 the  $YZ$  plane is chosen to be the scattering plane and  $\vec{E}_0$  is polarized along the  $X$ -axis (i.e.,  $E_{|0}=0$ ). In this case only the elements  $S_1$  and  $S_3$  are needed. They are proportional respectively to the components of the complex amplitudes of the scattered wave parallel and perpendicular to the incident polarization.

For forward scattering the optical theorem (van de Hulst, 1957) relates the extinction cross section  $C_{EXT}$  to  $S_1$  by:

$$C_{EXT} = \frac{4\pi}{k^2} \operatorname{Re} \{ S_1 \} \quad (2)$$

In this case, additional useful mathematical symmetry relations for an

axially symmetric particle are given by (Wang, 1968; Greenberg et al. 1963):

$$S_1(\chi, \psi) = S_{\chi E} \cos^2 \psi + S_{\chi H} \sin^2 \psi \quad (3)$$

$$S_3(\chi, \psi) = (S_{\chi H} - S_{\chi E}) \cos \psi \sin \psi$$

where  $S_1(\chi, \psi)$  and  $S_3(\chi, \psi)$  are the complex amplitudes corresponding to the arbitrary angle  $(\chi, \psi)$  as shown in Fig. 1, and where  $S_{\chi E}$  and  $S_{\chi H}$  are the complex forward scattering amplitudes when the symmetry axis is in the K-E and K-H plane respectively and is tilted by an angle  $\chi$  from the incident direction  $\vec{K}_0$ . The extinction cross section  $C_{\chi\psi}$  is therefore, from (2) and (3):

$$C_{\chi\psi} = C_{\chi E} \cos^2 \psi + C_{\chi H} \sin^2 \psi \quad (4)$$

Furthermore, from the first of Eqs. (3), we have:

$$S_1(\chi, \psi) = S_{\chi E} + (S_{\chi H} - S_{\chi E}) \sin^2 \psi \quad (5)$$

According to Equ. (5), the tip of  $S_1(\chi, \psi)$  in the complex Gaussian plane should trace a straight line when  $\chi$  is fixed and  $\psi$  is varied. The experimental technique enables us to plot  $S_1(\chi, \psi)$  as a function of  $(\chi, \psi)$  with an X - Y recorder. Thus, as  $(\chi, \psi)$  is rapidly changed by a target-orienting mechanism, Equ. (5) provides a quick check on the homogeneity of the scatterer and/or the accuracy of orienting the target in the radiation field.

### Sample Preparation and Refractive-Index Determination

The fact that a medium composed of alternate fine layers of different dielectric properties exhibits anisotropic refractive index with respect to the polarization direction of the electromagnetic field has been known for some time (Born and Wolf 1965) and has been used in the construction of polarizers, filters etc., in the field of optics. This work was motivated by the study of the extinction and polarization of light by graphite particles in interstellar space (Wickramasinghe et al. 1965). We constructed artificial media for microwave simulation possessing a graphite-like structure (Soule, et al. 1959).

Rytov (1955) has discussed the propagation of electromagnetic waves in a medium composed of two alternatively repeating layers of thickness  $d_1$  and  $d_2$ , dielectric constants  $\epsilon_1$  and  $\epsilon_2$ . He showed that if the layer period  $d = d_1 + d_2$  is sufficiently thin that

$$kd |m|_{\max} \ll 1 \quad (6)$$

then the entire medium behaves like a uniaxially anisotropic one with respect to the propagating wave polarization. Here  $|m|_{\max}$  is the maximum absolute value of refractive index over all possible directions of the medium. In this limit, the effective dielectric constants  $\bar{\epsilon}$  and  $\tilde{\epsilon}$  when the wave polarization is parallel and perpendicular to the layer planes respectively are:

$$\begin{aligned} \bar{\epsilon} &= \frac{\epsilon_1 d_1 + \epsilon_2 d_2}{d_1 + d_2} \\ \tilde{\epsilon} &= \frac{\epsilon_1 \epsilon_2 d}{\epsilon_1 d_2 + \epsilon_2 d_1} \end{aligned} \quad (7)$$

Identical results may be obtained in the static field case (Born et al. 1965). Rytov also discusses modifications to Equ. (7) when Equ. (6) is not satisfied. Independently, Collin (1958) published similar theoretical work.

After a number of trials, guided by the above considerations, we obtained measurements of samples with two different degrees of anisotropy in which condition Equ. (6) applies. Other types of anisotropy, which give highly interesting but complex scattering patterns, will be discussed in later publications.

Three targets in the size range:

$$2.58 \leq x = ka \leq 5.68 \quad a = \text{radius} \quad (8)$$

were constructed for each type of anisotropy. The principal refractive indices  $m_K$ ,  $m_E$  and  $m_H$  for the symmetry axis parallel to  $\vec{K}_0$ ,  $\vec{E}_0$  and  $\vec{H}_0$  of the incident wave respectively, were measured for each group applying the waveguide-slotted-line technique of Roberts-Von Hippel (1946) and using the X-band waveguide samples constructed from the duplicates of the target media and orientation configurations.

The first group of anisotropic media is a stack of seismograph recording paper, which consists of layers of royal gray paper, carbon film and paraffin. Application of heat and pressure bond these layers together. Since this medium is difficult to machine, each layer was scissor-cut according to the desired final shape prior to the bonding.

Anisotropic media of the second group were prepared from alternate layers of expanded polystyrene and a conducting paper called teledelto. Layered spherical metallic molds were used to form the expanded homogeneous polystyrene layers of uniform thickness, and one sheet of teledelto was inserted between each layer to introduce the anisotropy. The results of the dielectric measurements are presented in Table 1. The product spheres and their waveguide samples are also shown in Picture 1.

Table 1 DIELECTRIC-MEASUREMENT DATA

Group Number	Layer Number	Layer Material	Layer Thickness	Density of Medium	Measured Data \ Sample Orientation	H	E	K
I	1	Carbon Paper +	.0072 cm	1.051 grams/c.c.	Dielectric Constant $\epsilon$	3.26-i.36	2.32-i.087	3.04-i.24
	2	Carbon Paper +	.0072 cm		Refractive Index $m$	1.80-i.10	1.52-i.029	1.74-i.067
II	1	Teledelto *	.018 cm	0.500 grams/c.c.	Dielectric Constant $\epsilon$	1.89-i.42	1.63-i.012	1.91-i.38
	2	Dylite	.31 cm		Refractive Index $m$	1.38-i.15	1.28-i.0048	1.39-i.14

+ Seismograph Recording Paper, R.P.I., Troy, N.Y.

\* Lectronic Research Lab. AN/APA-23 Item 14, Stock #60303-1 (1968)

Polar Plots of the Complex Forward-Scattering Amplitudes and  
Comparison with the Theoretical Approximation

Experimental X-Y recorder plots of the complex forward-scattering amplitudes are reproduced in Figs. 2-a, -b, -c and Figs. 3-a, -b, -c for each target of Group I and Group II anisotropy (see Table 1). The vector drawn from the origin of this P-Q plot to each mark along the solid lines is the Cartesian Representation of  $S_1(\chi, \psi)$  at each orientation angle  $(\chi, \psi)$  and, in particular, K, E and H denote respectively the cases in which the symmetry axis is parallel to  $\vec{K}_0$ ,  $\vec{E}_0$  and  $\vec{H}_0$  of the incident wave.

The fact that the experimental line from E to H is straight is both a confirmation of the symmetry relation, Equation (5), and an indication of the accuracy of the experiment.

The region bounded by  $\delta S_E$  is the error limit of  $S_1(\pi/2, 0)$  due to target inhomogeneity and inaccuracy of the orientation technique as the scatterer is rotated around its symmetry axis held parallel to  $\vec{E}_0$ .

$\vec{S}_{std}$  denotes the vector representing the forward-scattering amplitude  $|S_1| = 13.57$  and phase shift  $\phi(0^\circ) = 43.8^\circ$  of a standard sphere during the same experimental run for coordinate calibration.

Projection of the  $S_1(\chi, \psi)$  vector on the Q-axis gives the extinction efficiency of the scatterer with orientation  $(\chi, \psi)$ , while the tilt of  $S_1(\chi, \psi)$  from the P-axis gives the phase shift at that orientation.



In this paper, we extend the Mie Theory to spheres of non-isotropic refractive indices, by applying the rigorous Mie solution (van de Hulst 1957) at each target orientation  $\chi$ , with an effective index of refraction  $m_\chi$  given by:

$$\frac{1}{\epsilon_\chi} = \frac{\cos^2\chi}{\epsilon_K} + \frac{\sin^2\chi}{\epsilon_F} \quad (9)$$

$$m_\chi^2 = \epsilon_\chi$$

where  $\epsilon_\chi$  and  $\epsilon_K$  are dielectric constants at orientation  $\chi$  and K, and  $\epsilon_F$  stands for either  $\epsilon_E$  or  $\epsilon_H$  depending on whether the symmetry axis is swept in the K-E plane or K-H plane. Equations (9) are derived as in crystal optics (Born et al. 1965). All  $\epsilon_K$ ,  $\epsilon_E$ ,  $\epsilon_H$  values are based on the measured ones in Table 1.

The evaluation of the forward-scattering quantities then follows the standard Mie calculation (van de Hulst 1957; Kerker 1969). The theoretical results are shown in Figs. 2-a, -b, -c and Figs. 3-a, -b, -c as dotted lines, and in particular, points  $K_M$ ,  $E_M$  and  $H_M$  refer to the results when the symmetry axis is parallel to  $\vec{K}_0$ ,  $\vec{E}_0$  and  $\vec{H}_0$  respectively.

The orientation dependence of the extinction efficiency  $Q_{EXT}$  for the smallest target with  $x = 2.58$  of Group I Anisotropy is plotted vs orientation  $\chi$  in Fig. 4, as deduced from experiment, Rayleigh approximation (van de Hulst 1957) and the effective-refractive-index approximation. As expected the total cross section based on the Rayleigh prediction are already much too large for this moderately small target. Furthermore, for K-H

rotation the Rayleigh approximation gives the opposite orientation dependence; whereas the new approximation is quite good.

The  $\chi$  dependence of  $Q_{KE}/Q_{KH}$  (the ratio of  $Q_{EXT}$  when the symmetry axis is in the K-E plane to that in the K-H plane) is shown in Figs. 5-a, -b, -c for Group I Anisotropy and in Figs. 6-a, -b, -c for Group II. These figures give the general picture of the orientation dependence of polarization of light by these particles. Here also, the Rayleigh approximation overestimates the polarization and fails to explain the subtle effect of orientation changes. Mie theory based on the effective refractive index gives a fairly close match.

When the symmetry axis of the particle is swept in the K-H plane, the  $S_1$  vector has smaller (but complex) variation relative to those when swept in the K-E plane. As compared to the P-Q plots by shape-anisotropic particles such as spheroids (Lind et al. 1965), we notice that these refractive-index-anisotropic particles show a marked difference in the orientation dependence of the polarization by extinction.

### Summary and Remarks

Summarizing the findings of this investigation, we state:

The microwave technique is capable of measuring forward-scattering to high precision, especially when temperature, physical dimensions and electronic conditions are stable.

The idea of artificially constructing nonisotropic target media using fine-layered composite structures is straightforward except that attention has to be paid to the layer thicknesses, and to the stability and machinability of the layer materials.

Mie Theory prediction using an effective refractive index at each target orientation is a good approximation for anisotropic spheres in the forward-scattering studies. When the symmetry axis is parallel to the polarization for which case the most precise refractive-index determination is possible, the agreement between experiment and theory is excellent. The agreement progressively degrades as one goes toward other principal orientations.

Crude angular distribution and back-scattering studies on some of these spheres were made, but due to mechanical and other difficulties, agreement between experiment and theory could only be qualitatively determined. These studies will be continued in an improved laboratory which is currently under construction.

Acknowledgement

This work has been supported by the National Science Foundation (GR-27085) and the National Aeronautics and Space Administration (NCR-33-011-043 and NAS 9-12539).

### References

1. Lind, A. C., Wang, R. T. and Greenberg, J. M., Appl. Optics, 4, p. 1555, 1965.
2. van de Hulst, H. C., "Light Scattering by Small Particles", John Wiley, 1957.
3. Wang, R. T., Ph.D. Thesis, R. P. I., Troy, N.Y., 1968.
4. Greenberg, J. M., Lind, A. C., Wang, R. T. and Libello, L. F., I.C.E.S., Pergamon Press, p. 123, 1963.
5. Born, M. and Wolf, E., "Principles of Optics", Pergamon Press, 1965.
6. Wickramasinghe, N. C. and Guillaume, C., Nature, 207, p. 366, 1965.
7. Soule, D. E. and McClure, J. Phys. Chem. Solids, Pergamon Press, (GB) 8, p. 29, 1959.
8. Rytov, S. M., J. Exper. Theoret. Phys., USSR, 29, p. 605, 1955.  
(English translation: Soviet Physics JETP, 2, p. 466, 1956)
9. Collin, R. E., Ire Trans. Microwave Th. and Tech., MTT-6, p. 203, 1958.
10. Roberts, S. and Von Hippel, A., J. Appl. Phys., 17, p. 610, 1946.
11. Kerker, M., "The Scattering of Light and Other Electromagnetic Radiation", Academic Press, 1969.

### Figure Captions

Fig. 1 Diagram of angular coordinates ( $\chi, \psi$ ) specifying the orientation of the symmetry axis of a layered spherical scatterer with respect to the direction of propagation  $\vec{k}_0$ , the direction of polarization  $\vec{E}_0$  and the magnetic vector  $\vec{H}_0$  of the incident radiation.

Figs. 2-a, 2-b, and 2-c Experimental polar plots and theoretical prediction of the complex forward-scattering amplitudes for spheres of Group I Anisotropy.

Figs. 3-a, 3-b, and 3-c Experimental polar plots and theoretical prediction of the complex forward-scattering amplitudes for spheres of Group II Anisotropy.

Fig. 4 Plots of extinction efficiencies  $Q_{EXT}$  vs orientation angle  $\chi$  as deduced from experiment, Rayleigh approximation and Mie Theory with effective refractive indices.

Figs. 5-a, 5-b and 5-c Plots of  $Q_{KE}/Q_{KH}$ , the ratio of extinction efficiencies when the particle symmetry axis is in the K-E plane and the K-H plane respectively, against the orientation angle  $\chi$ , for spheres of Group I Anisotropy.

Figure Captions - continued

Figs. 6-a, 6-b and 6-c      Plots of  $Q_{KE}/Q_{KH}$ , the ratio of extinction efficiencies when the particle symmetry axis is in the K-E plane and the K-H plane respectively, against the orientation angle  $\chi$ , for spheres of Group II Anisotropy.

Picture 1      Picture of anisotropic spheres (background) and their waveguide samples for refractive-index determination (foreground). The left-hand members are of the Group I Anisotropy, and the right-hand side are for the Group II Anisotropy.

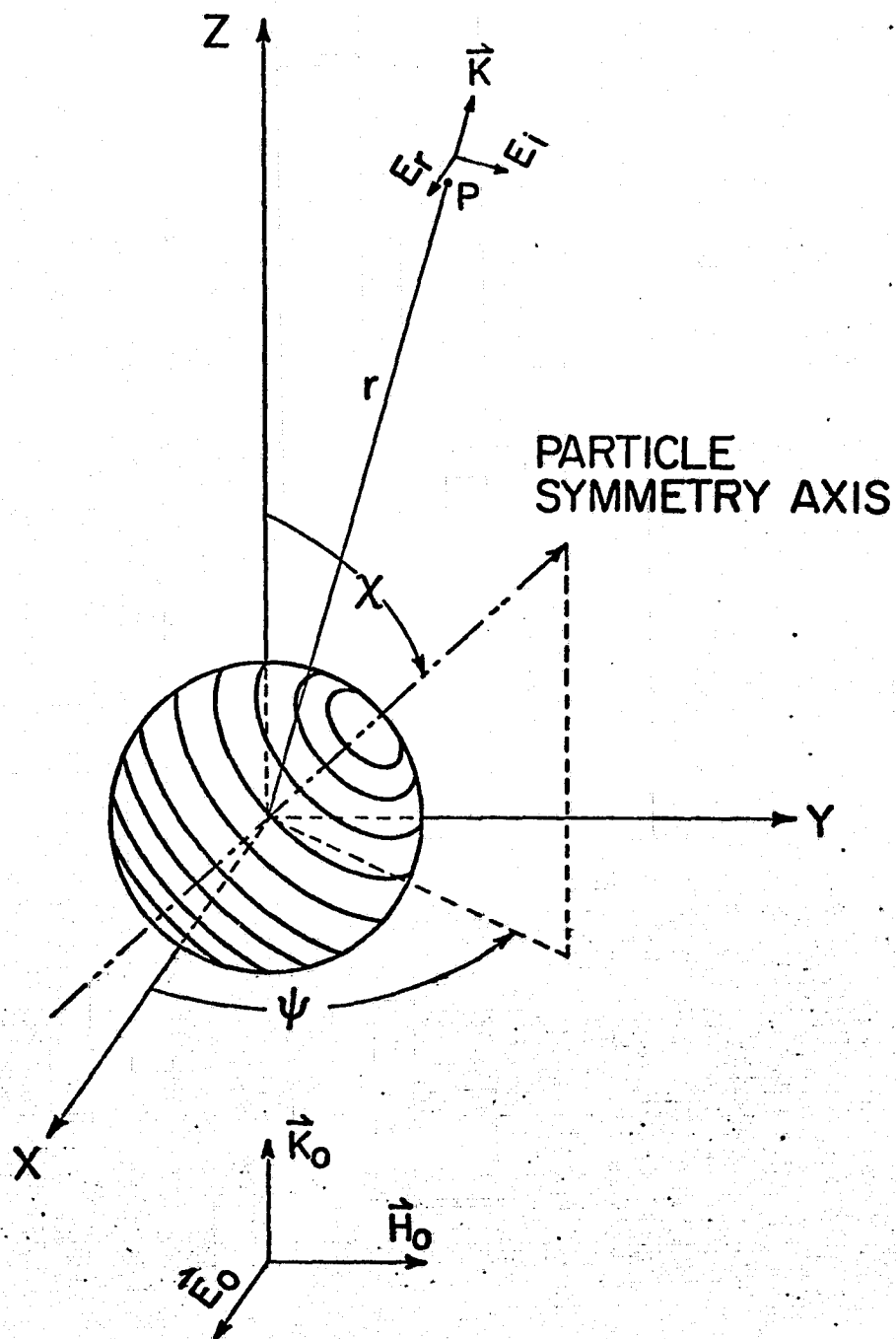
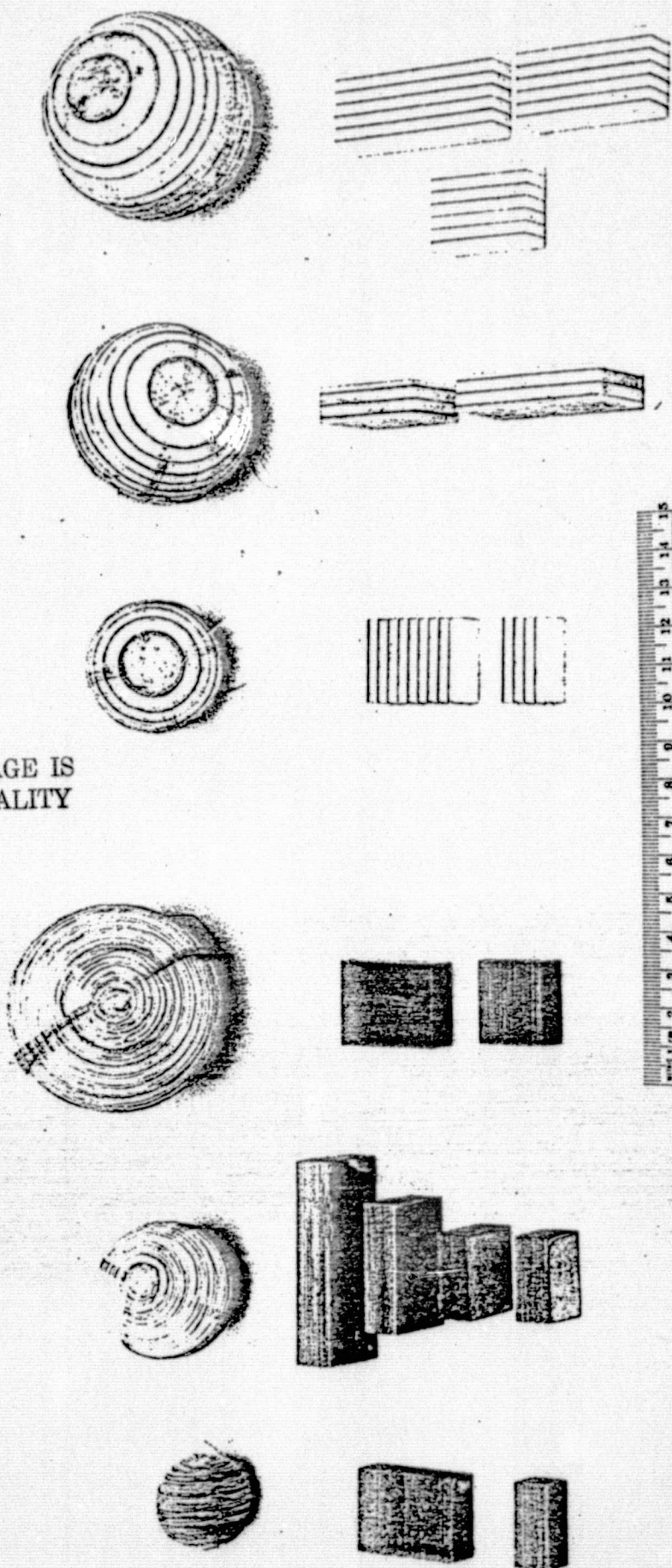


Fig. 1



ORIGINAL PAGE IS  
OF POOR QUALITY



Picture 1

$x = 3.69$   
Group I

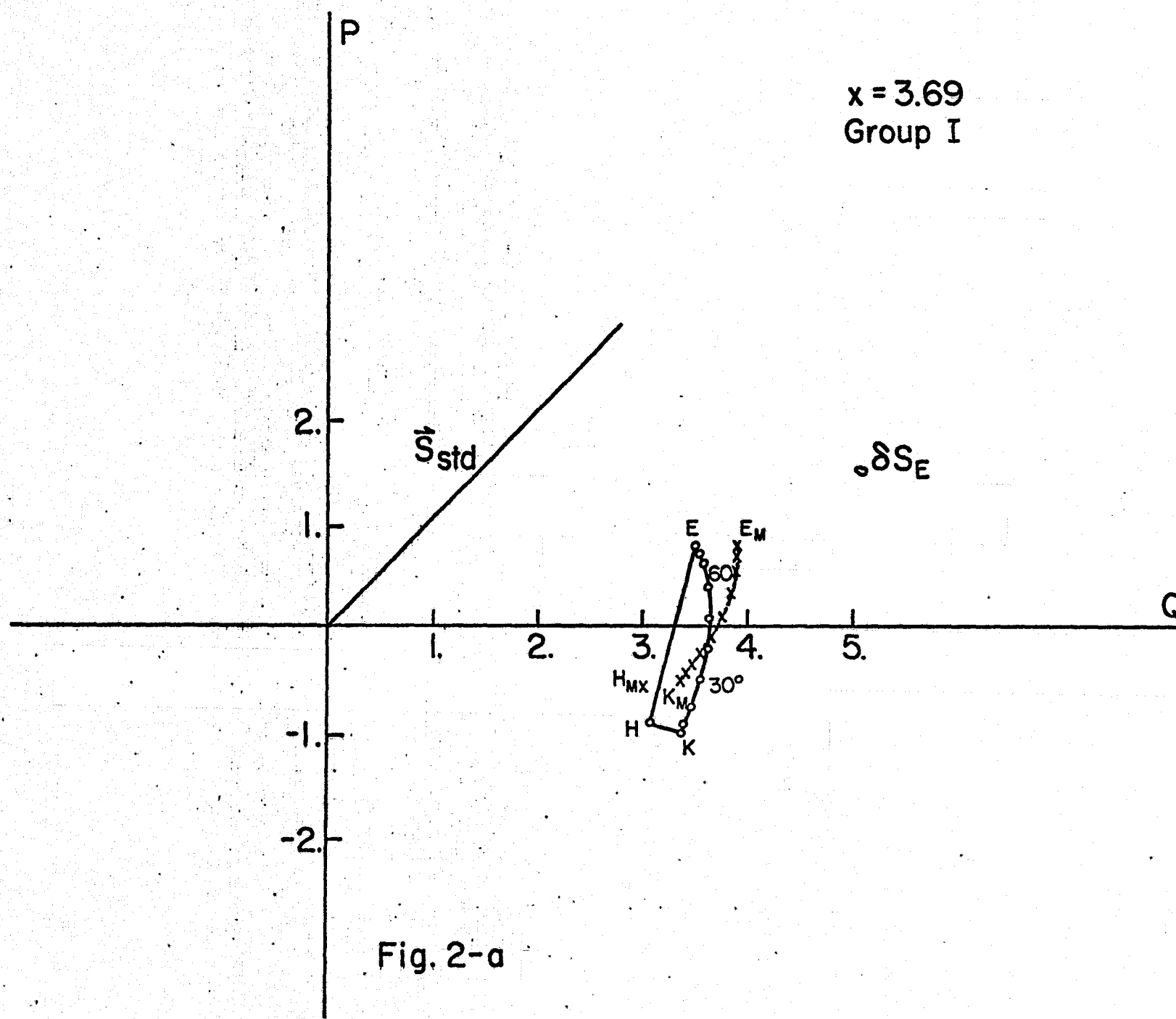
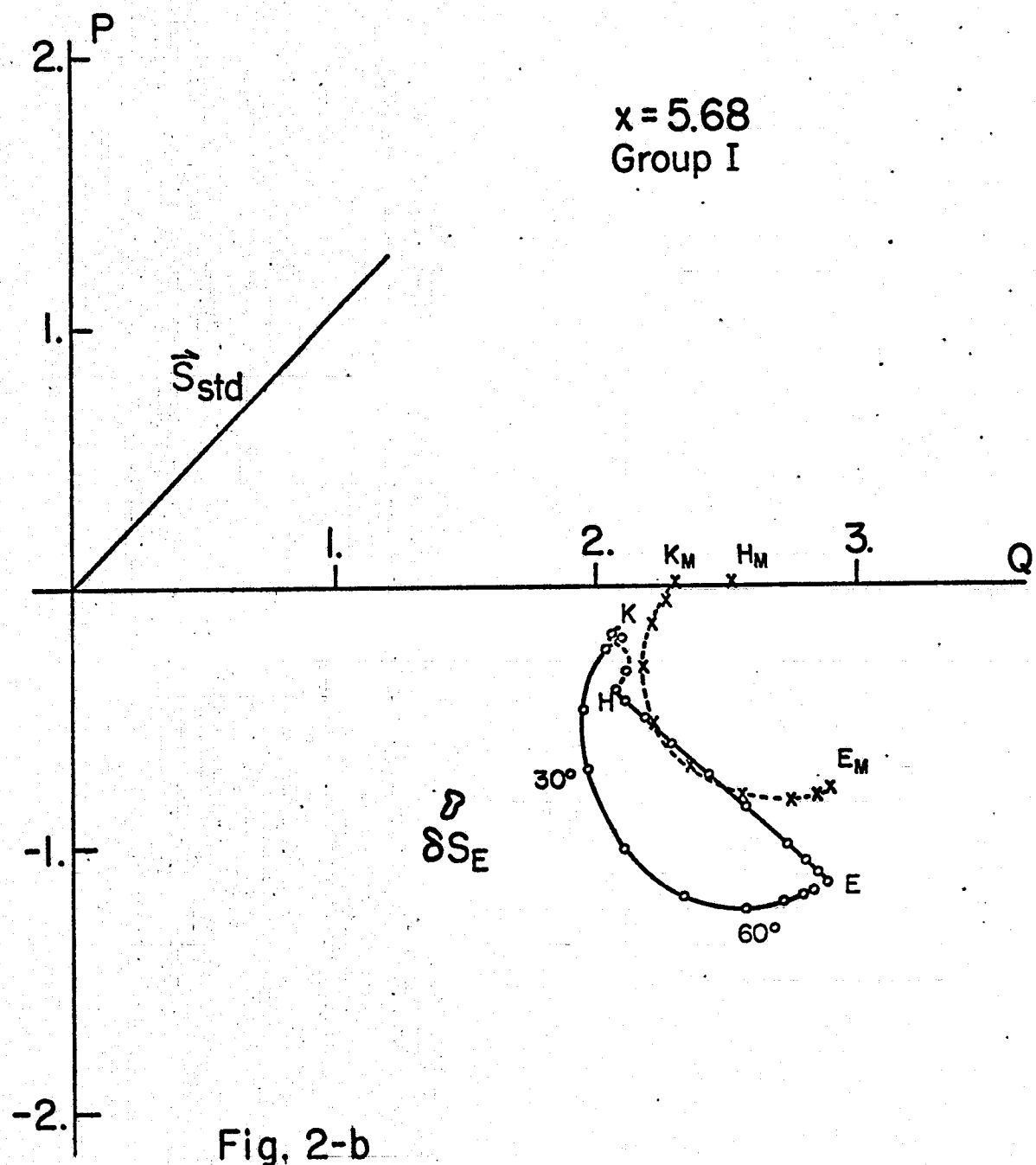


Fig. 2-a



$x = 5.68$   
 Group I

Fig. 2-b

ORIGINAL PAGE IS  
OF POOR QUALITY

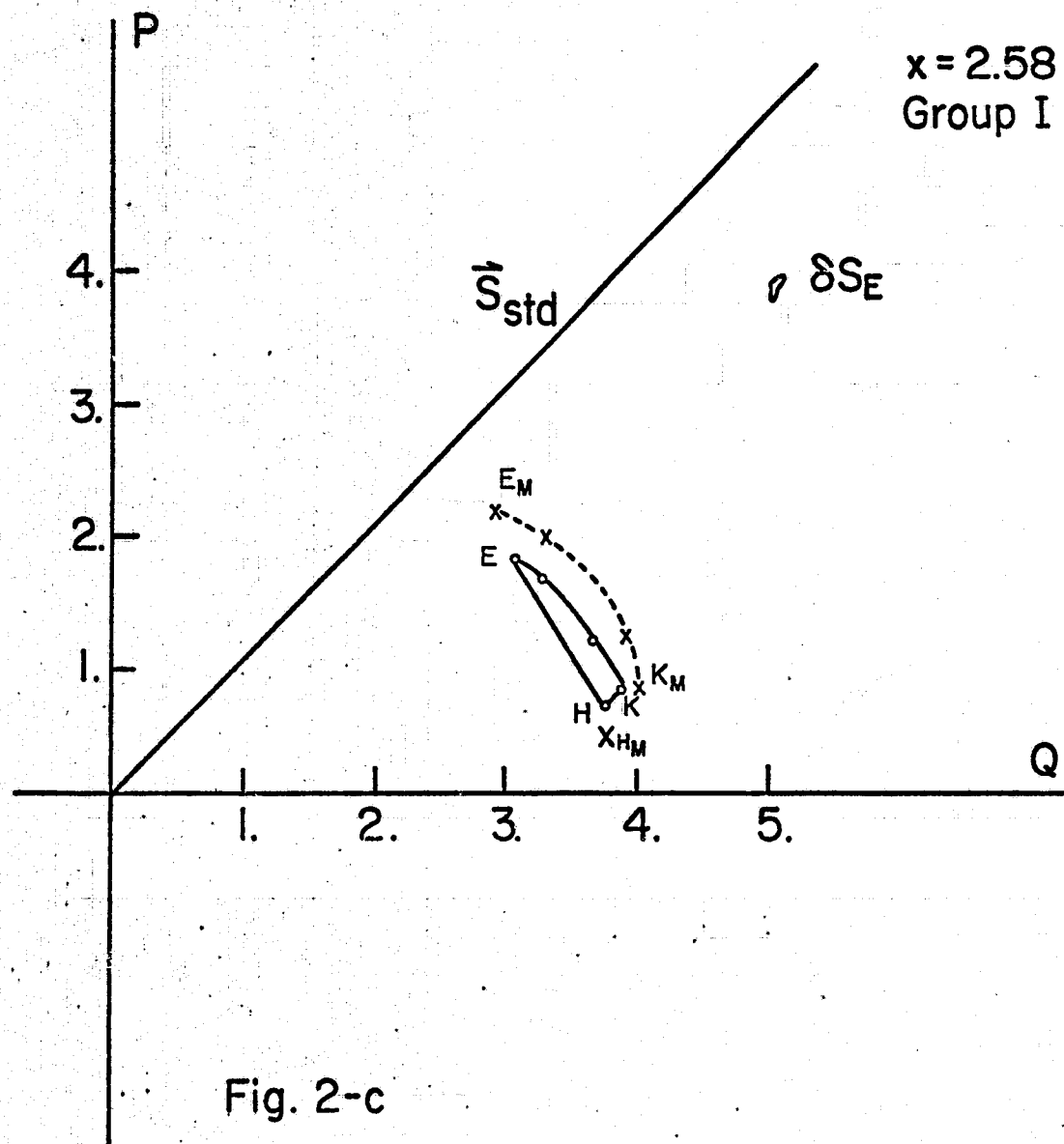
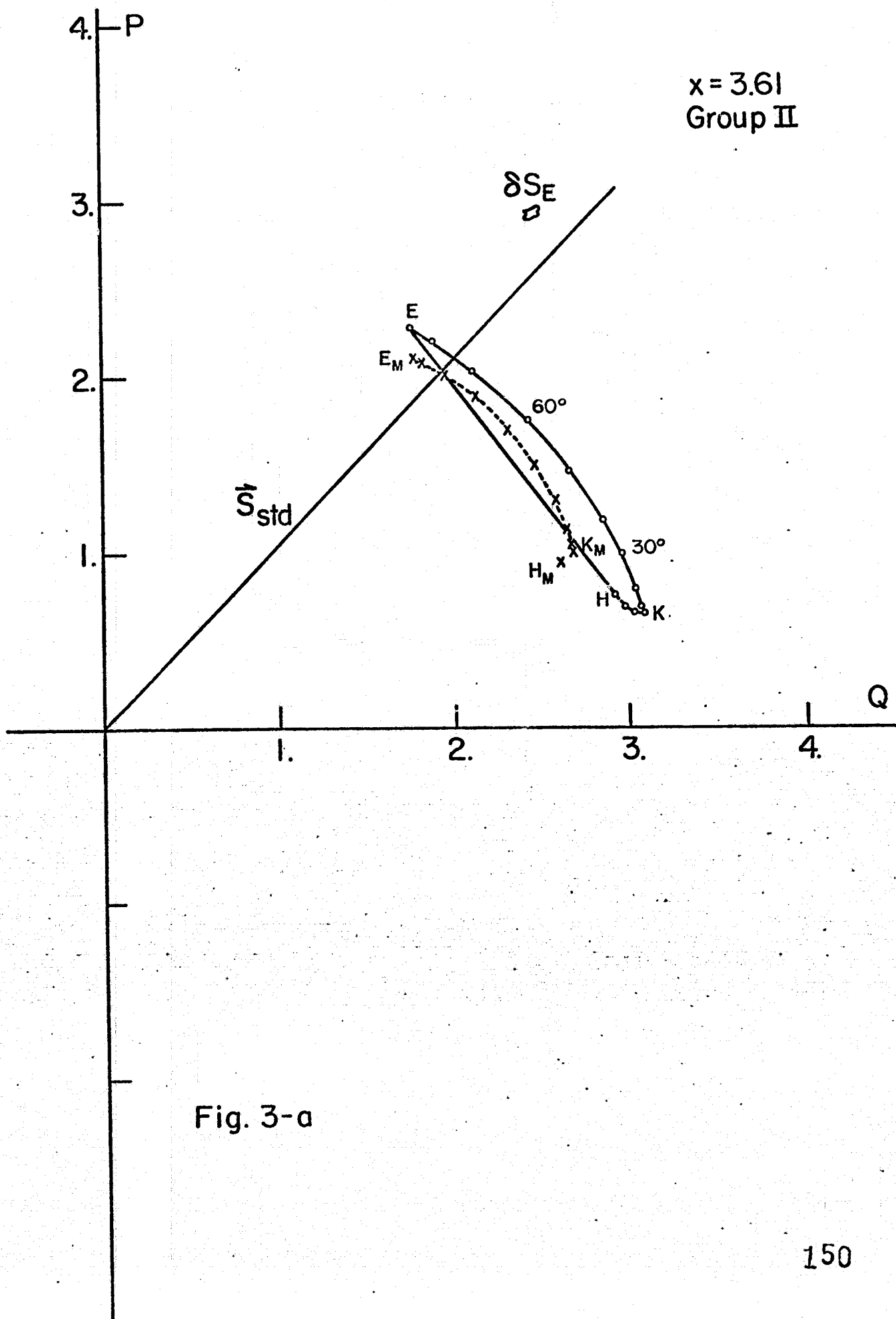


Fig. 2-c



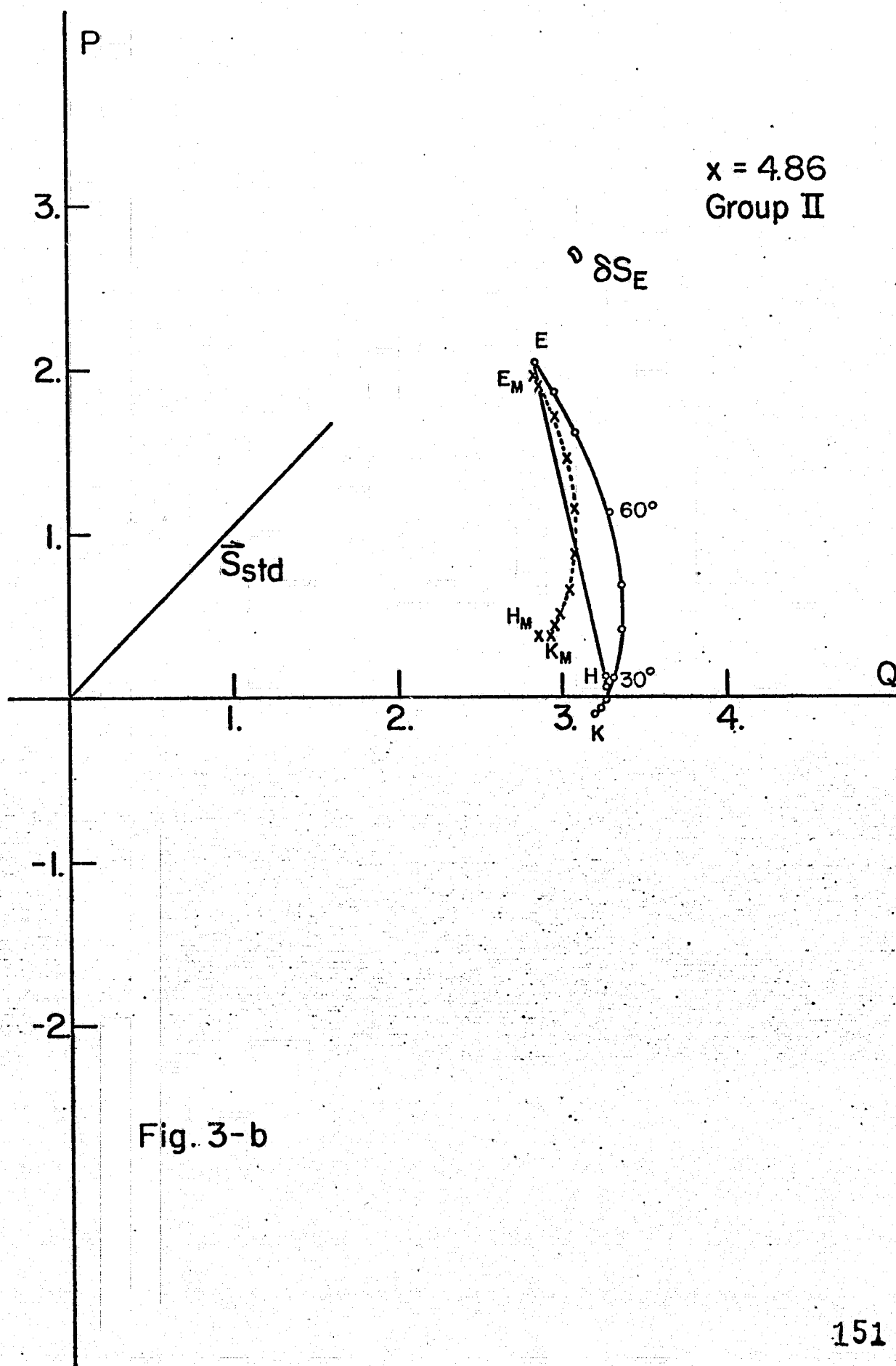
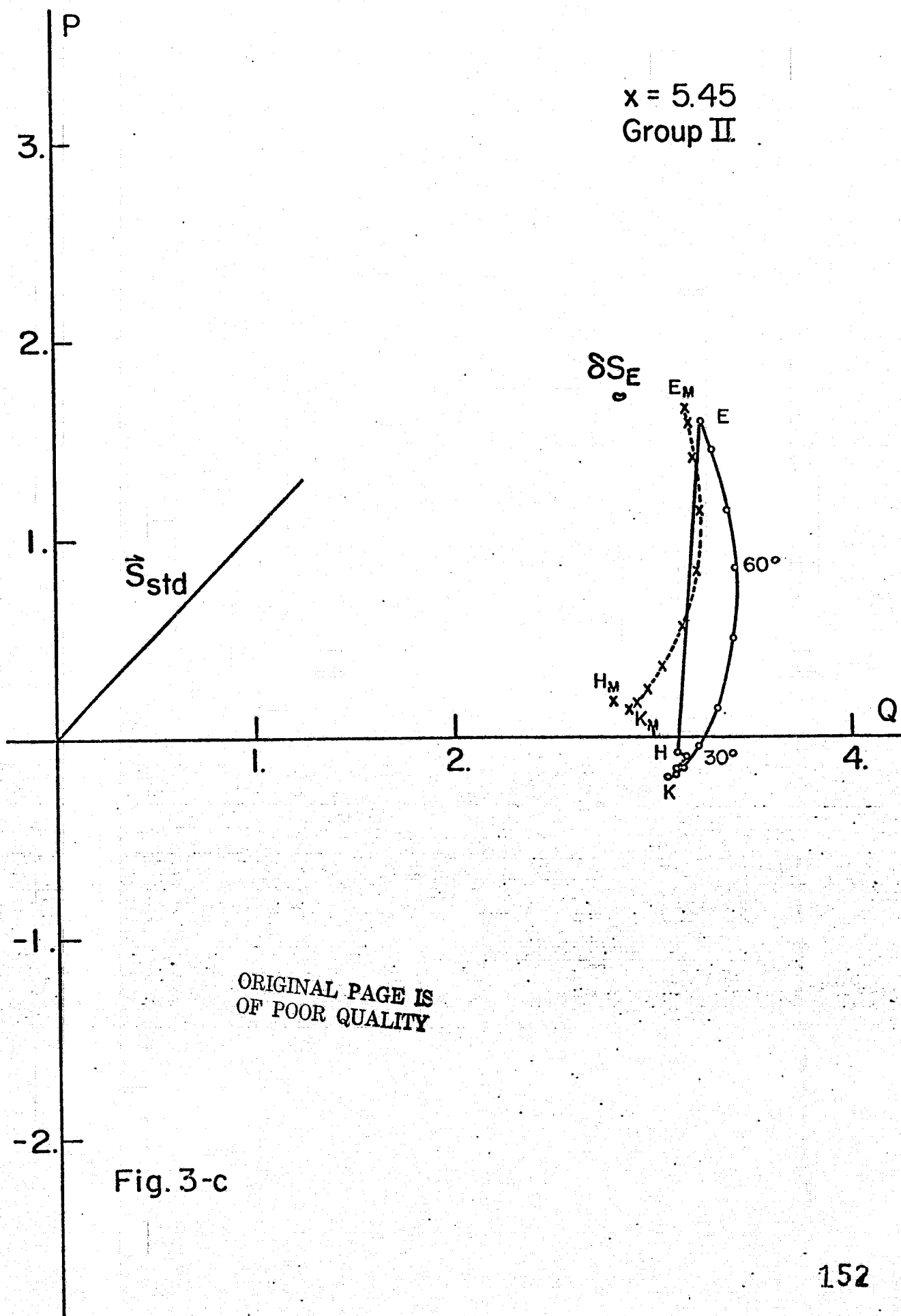


Fig. 3-b



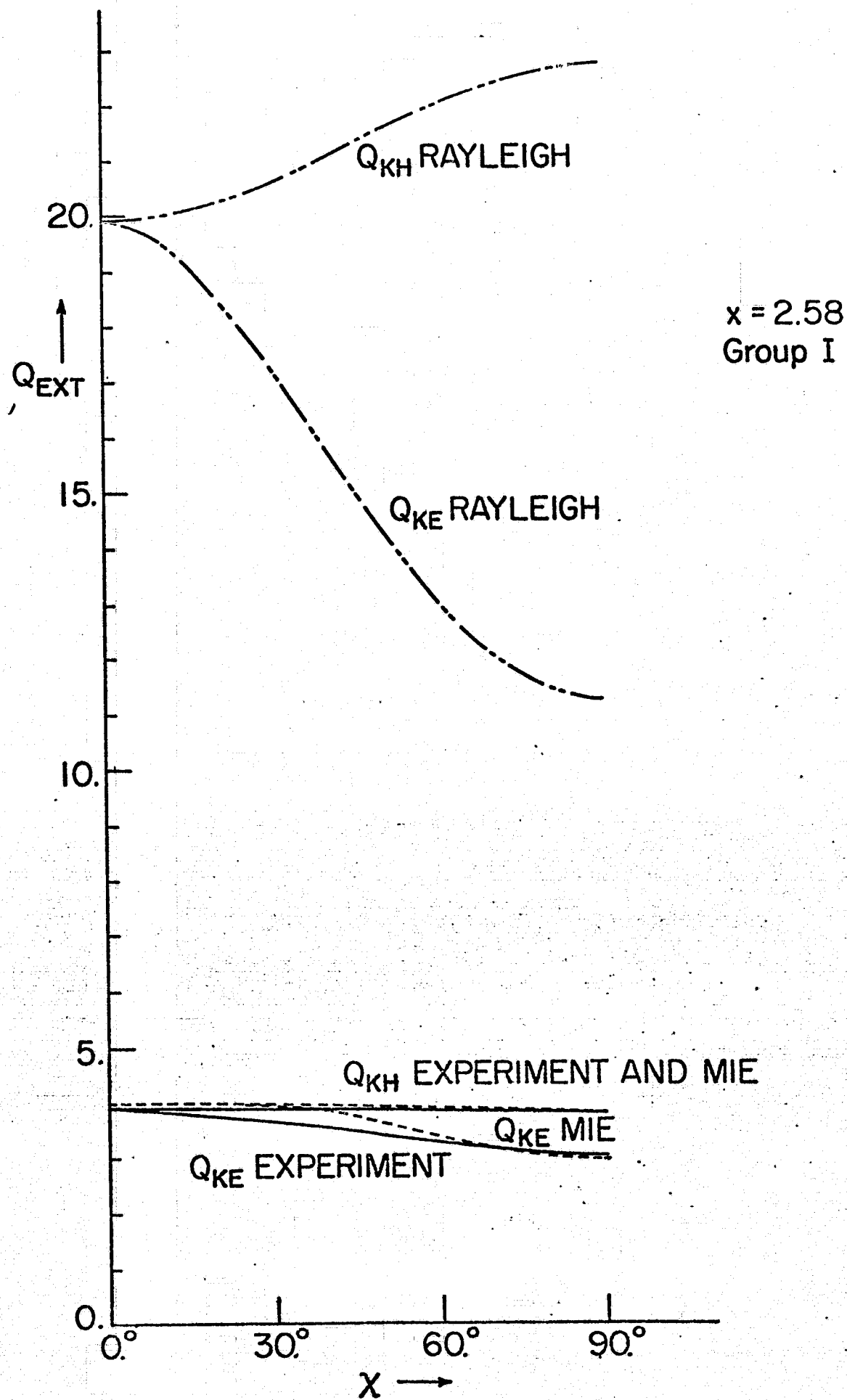


Fig. 4



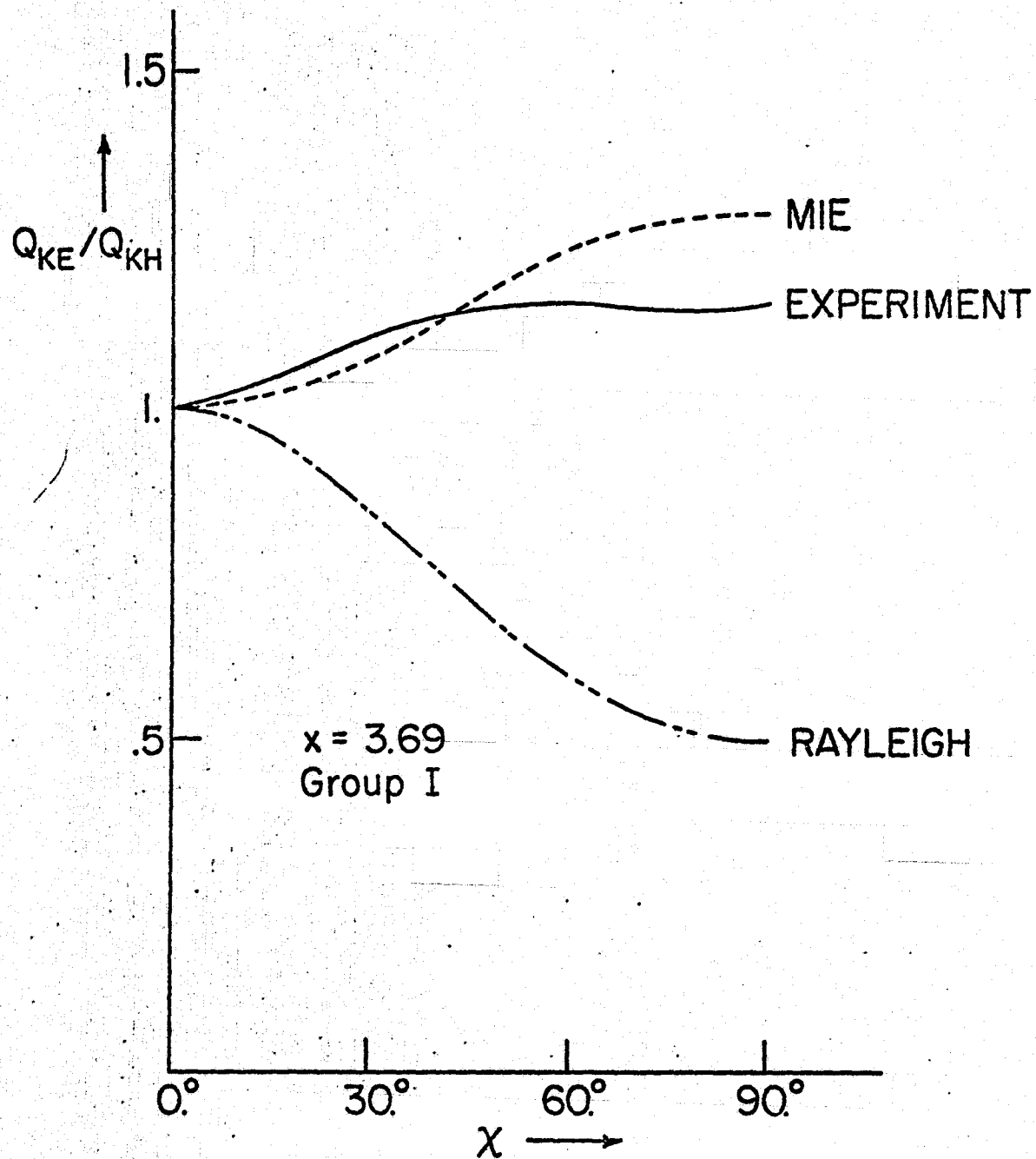


Fig. 5-a

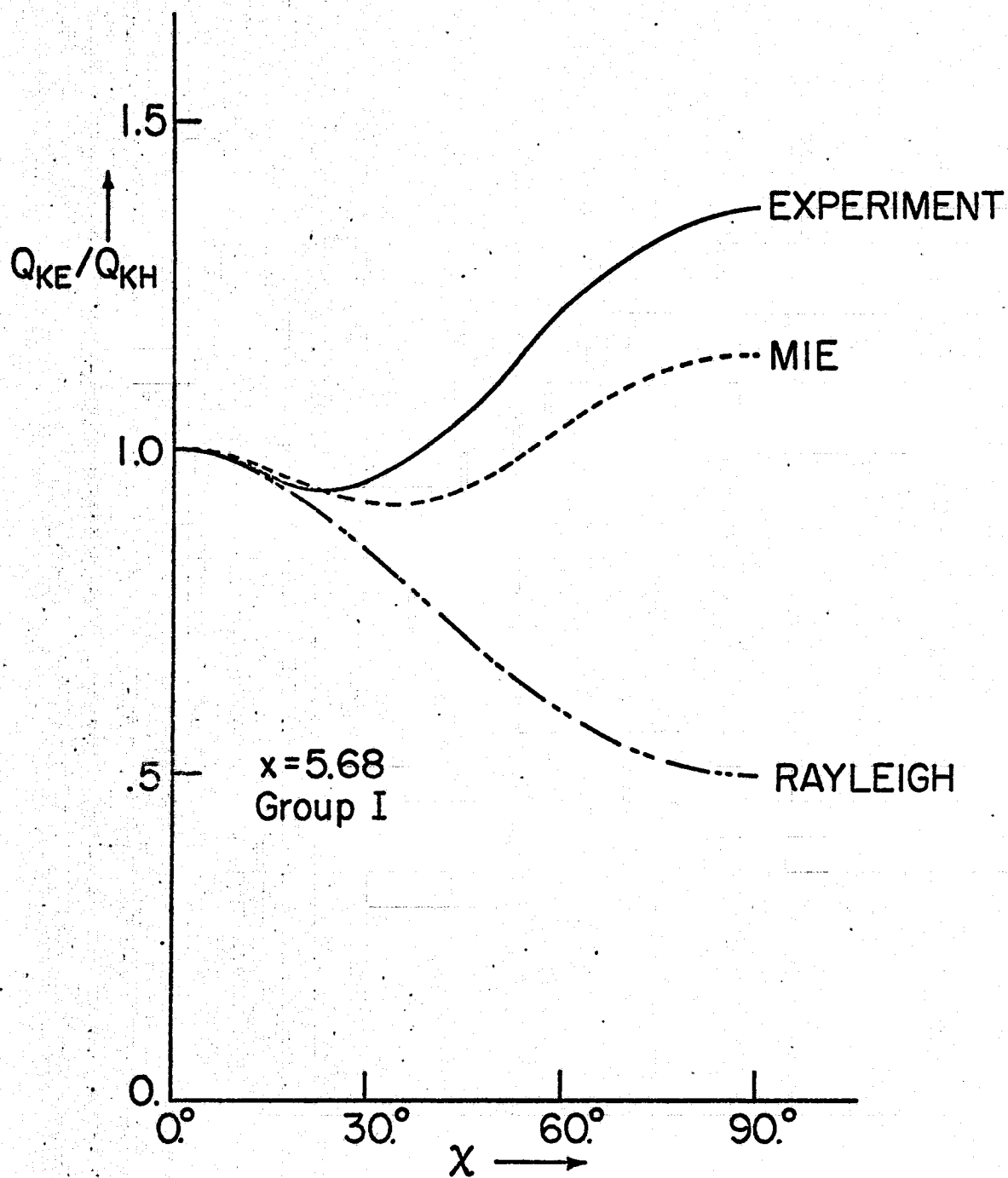


Fig. 5-b

ORIGINAL PAGE IS  
OF POOR QUALITY

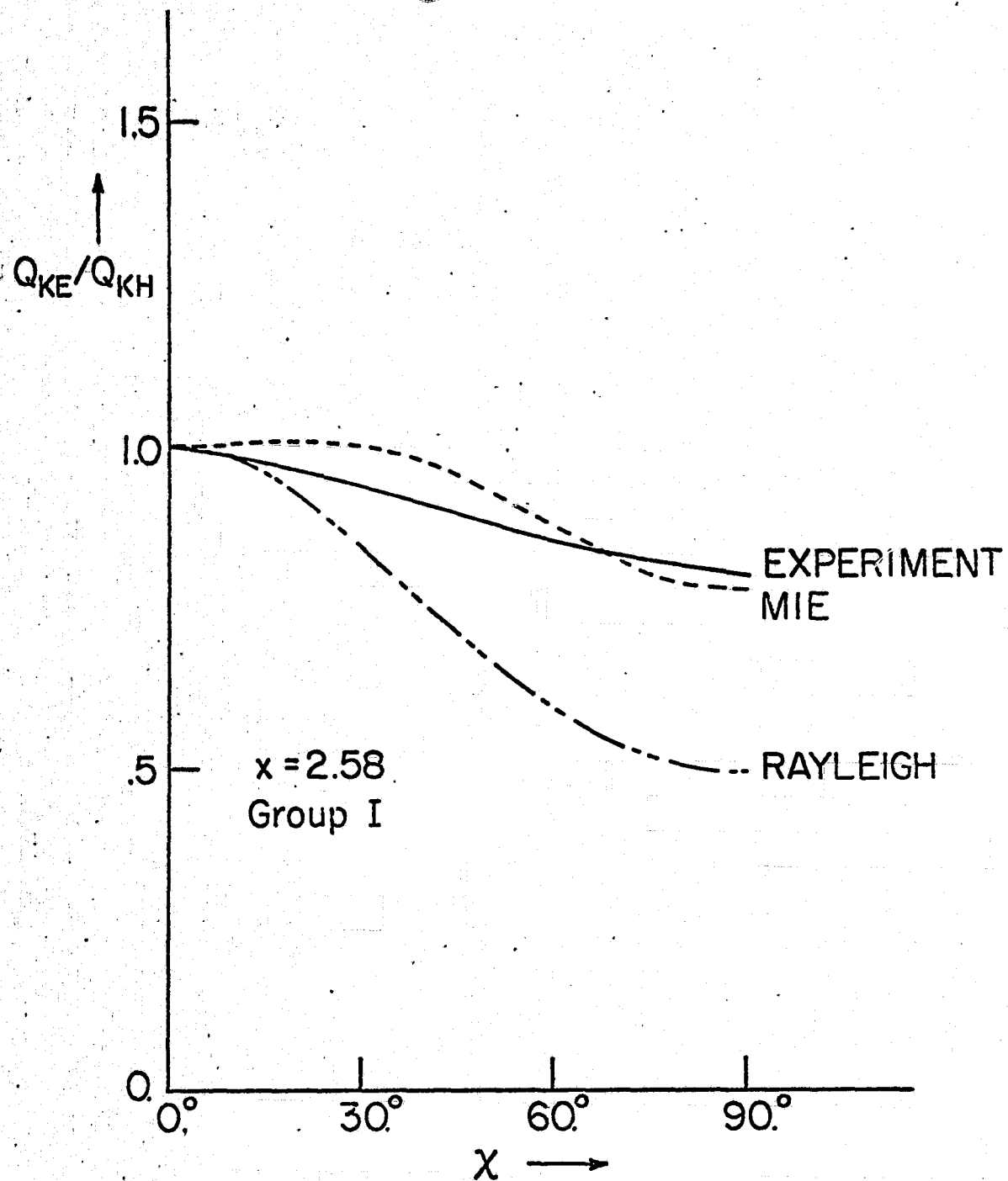


Fig. 5-c

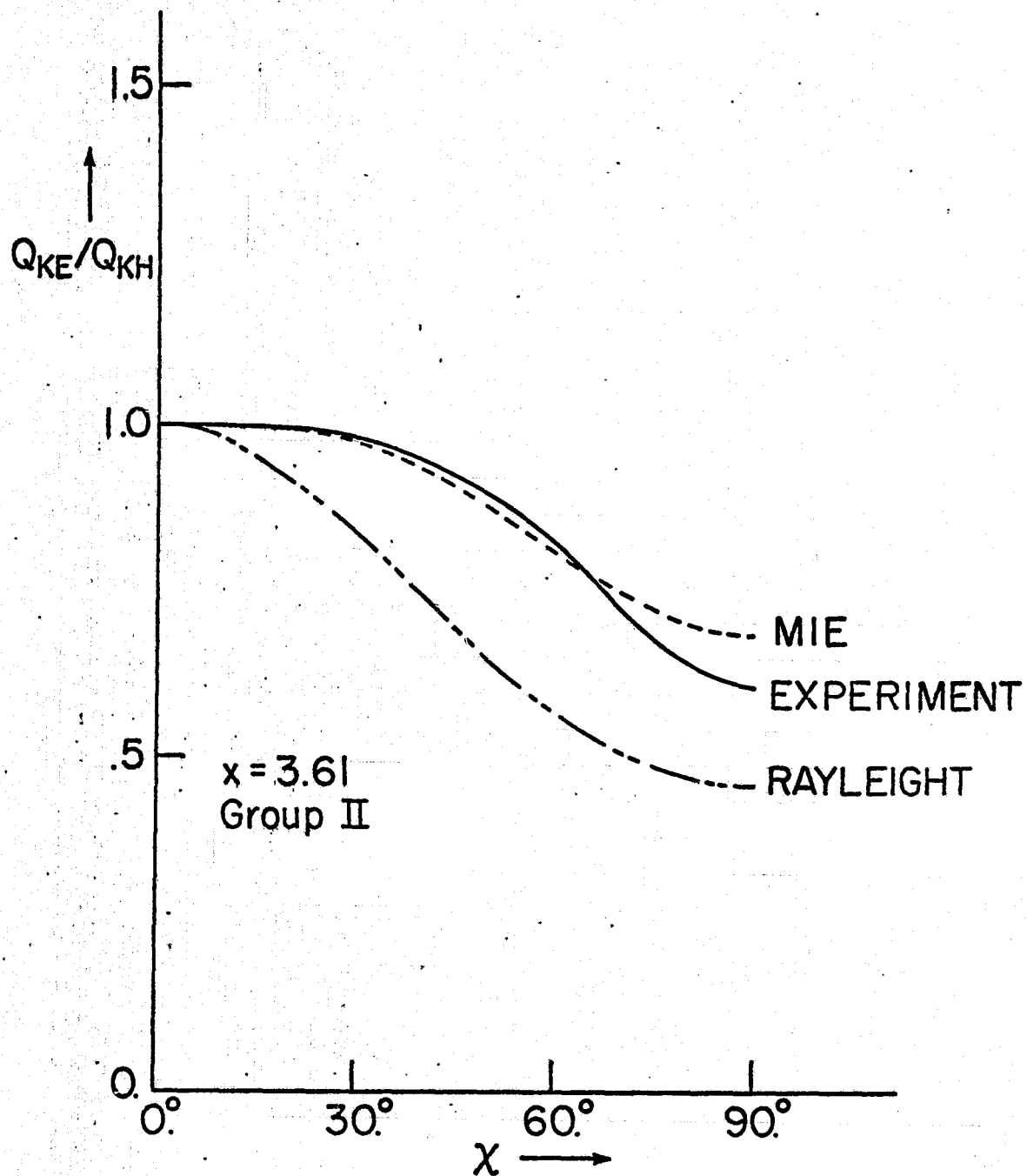


Fig. 6-a

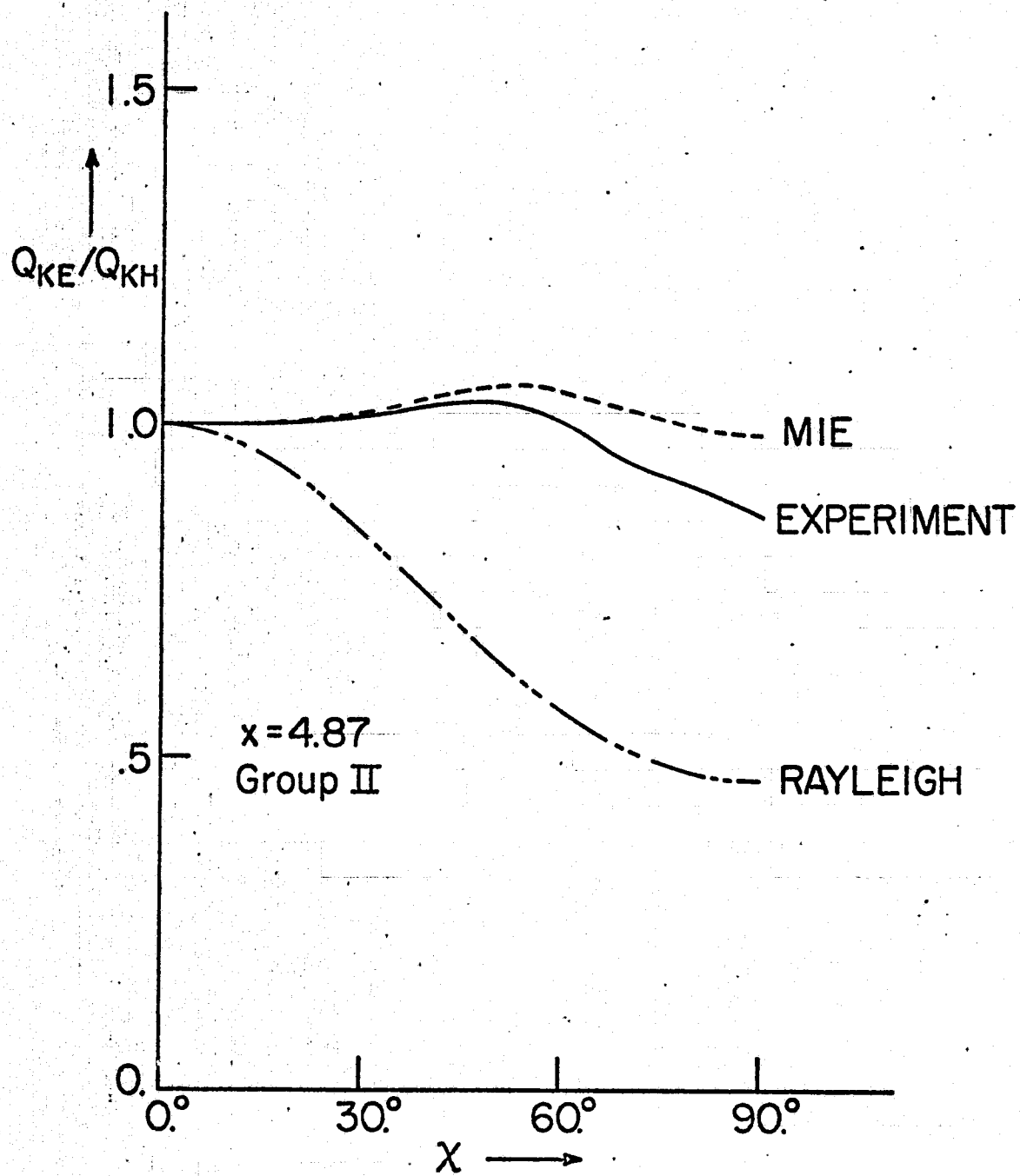


Fig. 6-b

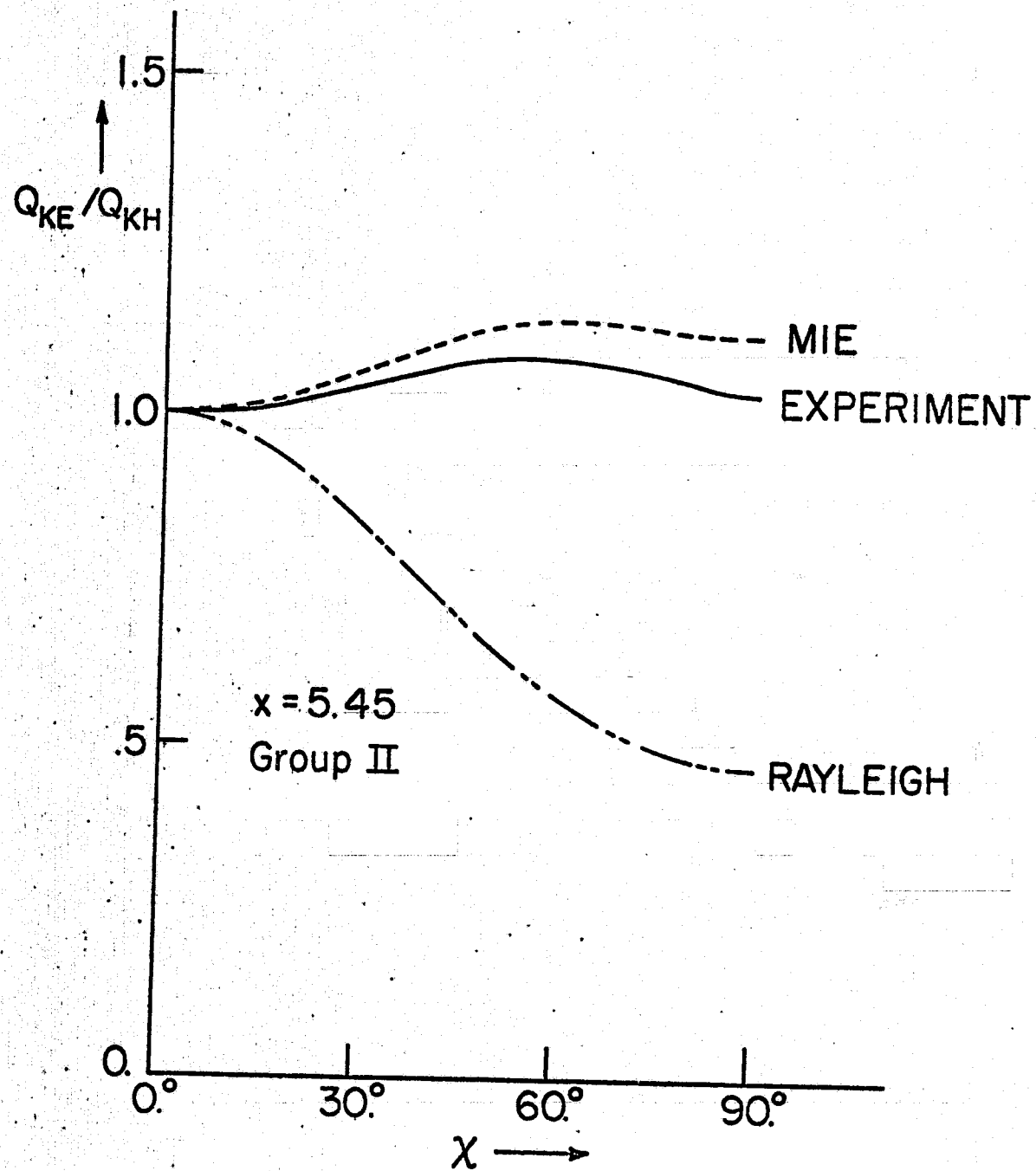


Fig. 6-c

## VIII SUPPORTING LABORATORY TESTS

## Table of Contents

### Supporting Laboratory Tests

	Page
Facility Description, Coronagraph and Optical Laboratory. . . . .	162
High Altitude Observatory (HAO) Tests . . . . .	163
Development of Resolution Testing Procedures. . . . .	164
Resolution Testing/Film Selection . . . . .	166
Flight Filter Resolution. . . . .	171
Ultraviolet Filter Light Leak Tests . . . . .	173
Neutral Density Filter Tests. . . . .	177
Interference Filter Calibration Tests . . . . .	178
Optimum Development . . . . .	179
EVA Vibration Simulation. . . . .	180
Kohoutek Flight Filter Resolution . . . . .	182
Refractive Index Tests. . . . .	184
Filter Photography Tests. . . . .	185
Occulting Disk Filter Tests . . . . .	186
Point Source Tests. . . . .	187
S052 Point Source Defocus Simulation. . . . .	189
Camera and Lens Historical Background . . . . .	190
Plate Scale Tests . . . . .	191
UV Lens Transmission Determination. . . . .	192
Defocus Simulation. . . . .	194
Lens/Filter Scatter Tests . . . . .	195
Vignetting Tests. . . . .	196
Sensitometer Design and Calibration . . . . .	197
Extension of Sensitometer Wedge Latitude. . . . .	199
Sensitometry Deterioration . . . . .	200
Vacuum Effect on Sensitometry . . . . .	201
Microdensitometer . . . . .	202
Diffuse Density Calibration . . . . .	204
Rejection Ratio Determination, Flight Film. . . . .	205
Image Restoration . . . . .	206



### Facilities Description, Coronagraph and Optical Laboratory

In order to provide an area for particle analysis and data reduction, the Laboratory for Particle Scattering was constructed in early 1973. The laboratory is a 41' x 100' x 16' high metal building, electrically heated and air conditioned, and located on the grounds of Dudley Observatory. Enclosed within the building is the Coronagraph and Optical Test Laboratory. The Coronagraph Test Laboratory houses a 25 foot vacuum tunnel with a one solar constant xenon arc source for space simulation testing of the T025 coronagraph. The optical section houses a radiometric area and contains extensive spectroscopic instrumentation. The photographic section houses a photographic darkroom facility and photographic instrumentation. The data reduction area includes a 10 x 15 foot laminar flow clean room which houses a Joyce-Loebl digitized isodensitometer. This instrument was used to digitize the T025 photographic data for subsequent computer analysis through our terminal access to a UNIVAC 1110 computer.

### High Altitude Observatory (HAO) Tests

Extensive testing was conducted at the HAO Coronagraph Test Facility in Boulder, Colorado during the first half of 1972 to determine the rejection ratio of the instrument, to test and select baffle designs for the coronagraph, to reduce our selection of film types, to gather preliminary data on airborne particle density counts, to determine the optimum interior spacecraft lighting for T025 operation, and to further define numerous additional experimental parameters. The Coronagraph Test Facility consisted of a 250 foot long, baffled vacuum chamber with an external steerable mirror to collimate the solar beam axially through the chamber.

As a result of these tests, the rejection ratio of the instrument, without baffle, was determined to be  $2.5 \times 10^{-9}$ . The addition of a circular baffle improved the rejection ratio to  $2.0 \times 10^{-9}$ .

### Development of Resolution Testing Procedures

In order to establish a standard uniform procedure for photographic resolution testing, several resolution testing boards were constructed. The standard resolution board is 32" x 48" in size and consists of a number of standard Air Force resolution targets (W. & L. E. Gurley, Troy, N.Y.) as shown in Fig. 1a, on a black background. The targets are spaced over the entire surface of the board in order to obtain complete coverage in the field of view. The normal set-up consists of the camera placed along a line normal and through the center of the resolution board and at a distance from the board to allow the field of view of the lens to span the entire surface of the board. Illumination is provided by light bulbs positioned  $45^{\circ}$  away and on both sides of the camera. Two smaller, portable resolution boards were similarly constructed for convenient transportation. Numerous tests were conducted with each of the resolution boards to determine the camera-to-board distance and illumination levels required for proper exposure with a variety of films. We decided not to use the Fourier MTF method for resolution testing due to the difficulty and time consumption required for preparation.

A Sayce resolution target, as shown in Fig. 1b, was used particularly to test and calibrate the resolution of the Joyce-Loebl isodensitometer and to optimize the data reduction capability of the machine.

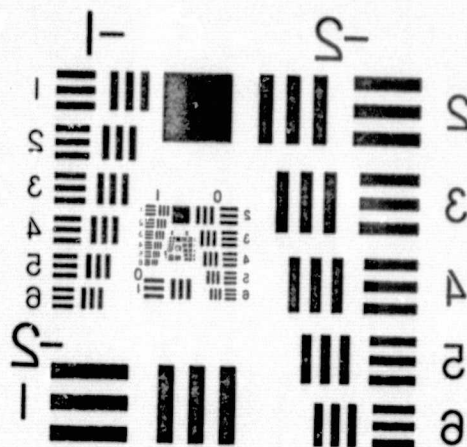
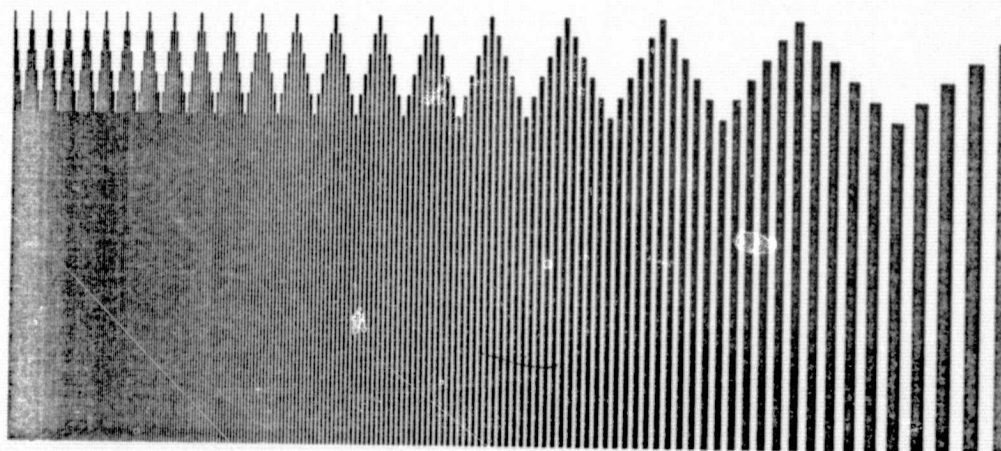


Fig. 1a Standard Air Force Resolution Target

ORIGINAL PAGE IS  
OF POOR QUALITY



GURLEY, TROY, N. Y.

SAYCE TARGET

Fig. 1b Sayce Resolution Target

### Resolution Testing/Film Selection

Resolution tests were conducted with Kodak Aerographic Tri-X 2403, Kodak 2485 High Speed Recording Film and Kodak Panatomic-X films to determine the resolution of each film with no filter, a  $6000\text{\AA}$  and a  $5000\text{\AA}$  central bandpass interference filter. This data was required for the selection of flight films.

A summary of the results is provided in Figs. 2, 3, and 4. All resolution data provided in these figures is for the center of the frame measured. Similarly shaped resolution curves were generated for other positions in the field, although generally at a poorer resolution.

Tri-X 2403 was selected as optimum for our requirements due to its superior resolution characteristics and relatively high speed. The additional speed obtained with the 2485 film was more than offset by its poor resolution and extreme graininess. Based on those observations, a higher signal to noise (S/N) results with the Tri-X 2403 except for the lowest illuminance levels. However, taking into account the high radiation levels anticipated in Skylab, it was expected that even for the lower illuminance levels, the S/N level should be higher for Tri-X 2403. The eventual Skylab results have confirmed this.

Resolution tests were conducted with Kodak Aerographic Tri-X 2403 and Kodak Spectroscopic IIao films to compare relative speed and resolution. This spectroscopic film was of interest to us due to its lack of red sensitivity which would improve the blocking of system when using ultraviolet

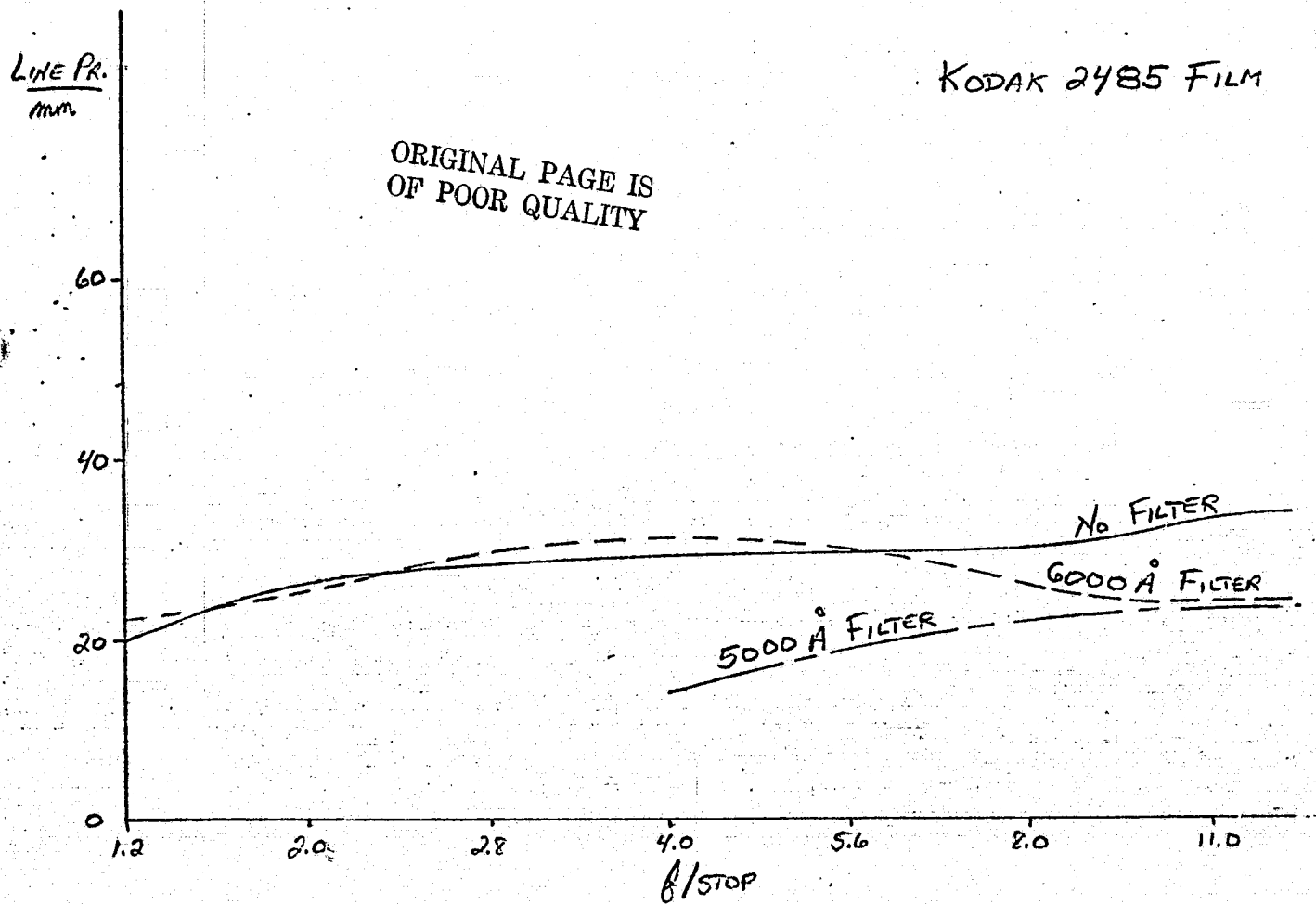


FIG. 2

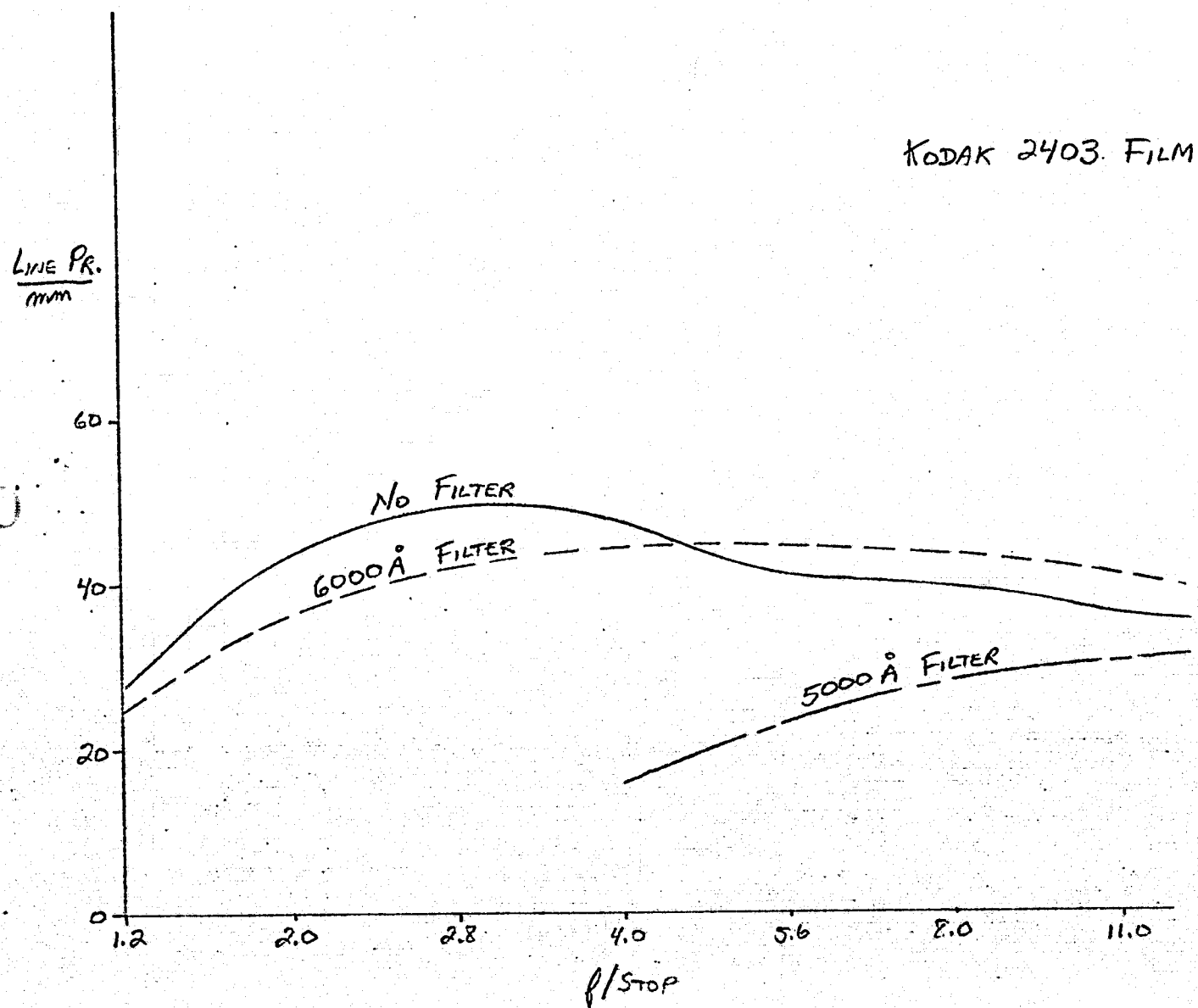
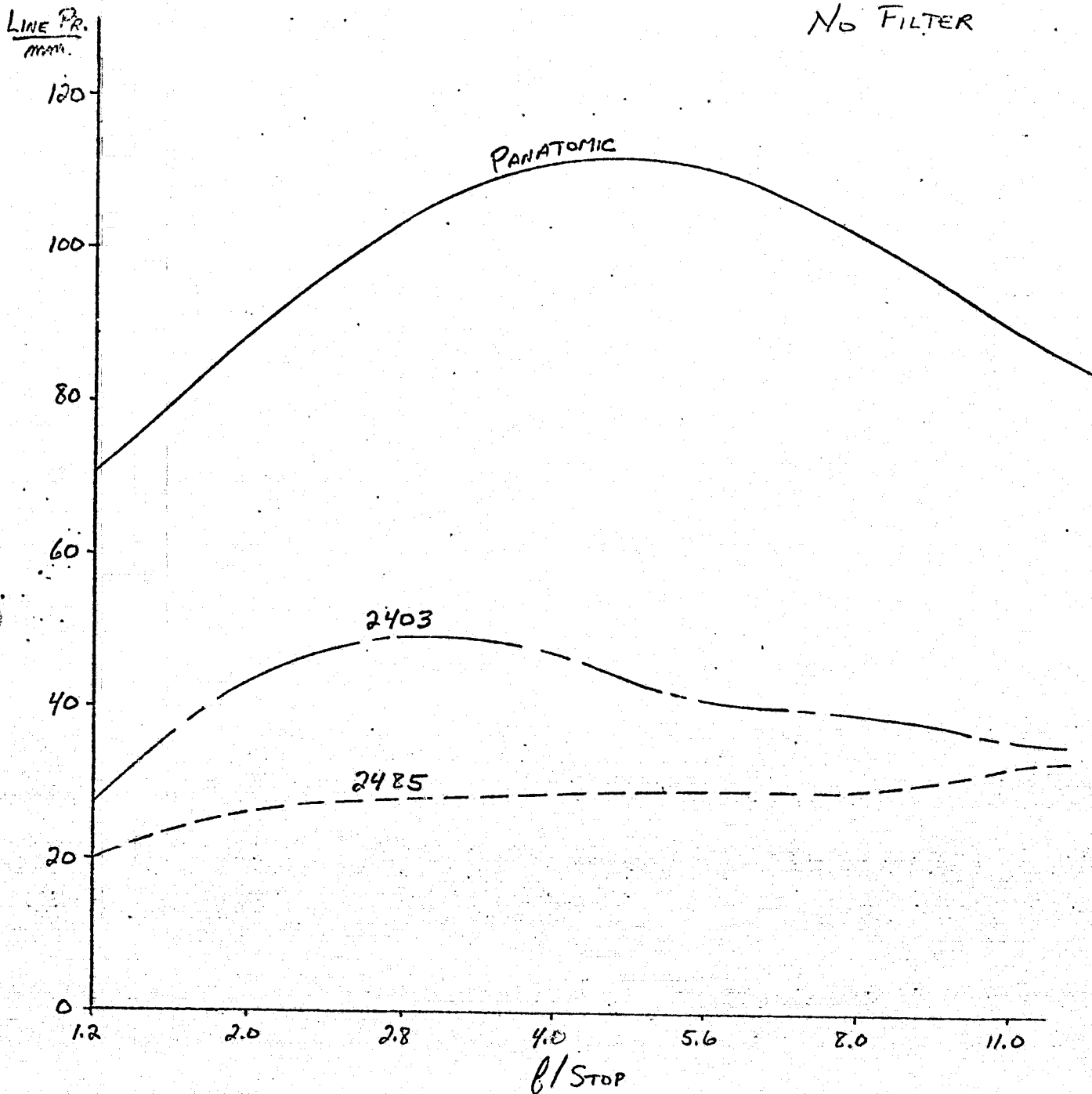


FIG. 3



ORIGINAL PAGE IS  
OF POOR QUALITY

FIG. 4



Resolution Testing/Film Selection - continued

filters. Kodak IIao was found to be, however, two stops slower for exposure in the 0.1 sec range, and, as it was slightly poorer in resolution than Tri-X 2403, we decided that Kodak IIao was not acceptable.

### Flight Filter Resolution

Resolution tests were conducted with the three P.I. ultraviolet filters ( $2450\text{\AA}$ ,  $2800\text{\AA}$ ,  $3600\text{\AA}$ ) and Kodak 2403 and 2485 films and the 27 mm, f/2.0 flight-type UV lens on loan from Dr. Packer of NRL (as we did not receive our UV lens until the SL-1 launch). A summary of the results is given in Table 1. Although the results presented are for the center of the field at f/2.0, resolution data was obtained over the entire field of view of the lens and at the full range of aperture settings (f/2.0 - f/16).

During these tests, it appeared that the  $2450\text{\AA}$  and  $2800\text{\AA}$  filters had excessive red leaks beyond specifications. Consequently, we photographed a target illuminated by a xenon arc source, of known spectral distribution, both directly and through crown glass, which would cut off nearly all radiation short of  $3300\text{\AA}$ . Subsequent calculation of the amount of red leak proved conclusively that the manufacturer's specifications were not met.

Table 1

Flight Filter Resolution (P.I. set)

27 mm UV lens, K1 adapter, f/2.0, center of field

<u>Filter</u> <u>Central Wavelength (Å)</u>	<u>Resolution (line pairs/mm)</u>	
	<u>Kodak 2403</u>	<u>Kodak 2485</u>
None	20	8
2450	32	20
2800	56	14
3600	20	10

### Ultraviolet Filter Light Leak Tests

Photographic tests with the 2450<sup>0</sup>Å ultraviolet filter indicated that an extensive amount of radiation outside the bandpass was being transmitted. Since such a condition would adversely affect the experiment, a thorough examination of the problem was necessitated. Since Martin Marietta Corp. (MMC), responsible for the acquisition of the filters, had failed to test the filters for blocking, spectral transmission tests using a Jarrell Ash .25 meter Ebert Monochromator were conducted. An in passband to out of passband ratio of 1.60 was determined which proved conclusively that the filter was not scientifically usable. Consequently, a satisfactory replacement filter was acquired from Baird Atomic, Inc. and hand carried to KSC for installation.

This problem was primarily caused by Martin Marietta failing to hold the filter manufacturer to tight specifications. As a result, when filters were procured for Comet Kohoutek observations, we were careful to generate comprehensive and detailed specification sheets to assure the proper manufacture of the filters. An example of our specification sheets is presented in Table 2.

3940 Filter DO-3940

1. All measurements are to be based on parallel light  $7^\circ$  from normal incidence.
  - Central wavelength,  $\lambda_c$  3945Å  $\pm 5$
  - Transmittance ( $T_{max}$ ) at peak wavelength shall be greater than 17%
  - The half power band width (HPBW) shall be 20Å  $\pm 5$
  - Bandwidth at 10% of  $T_{max}$  shall be between 1.6 and 2.4 times HPBW.
  - Bandwidth at 1% of  $T_{max}$  shall be less than 4 times the HPBW.
  - Bandwidth at 0.1% of  $T_{max}$  shall be less than 7.5 times the HPBW.
  - Bandwidth at 0.01% of  $T_{max}$  shall be less than 15 times the HPBW.
  - Index of refraction must be greater than 1.8

Transmission outside the passband shall be less than 0.01%. Outside the passband is defined here as the region between  $(3940 + 8 \times \text{HPBW})\text{\AA}$  and  $6900\text{\AA}$ , and the region between  $2300\text{\AA}$  and  $(3945 - 8 \times \text{HPBW})\text{\AA}$ .

2. Spectral transmission curves for  $7^\circ$  from normal incidence shall be provided between 2000 and 7000Å with full scale of 100%, 10%, 1%, 0.1% and 0.01% transmission.
3. The index of refraction of each filter shall be provided.
4. Filter shall be edge marked with part number DO-3940 and serial number (i.e. 04, 05, 06)
5. No visible striae shall be present.

Filter shall not be degraded optically or structurally by long term exposure to temperature between  $-40^\circ\text{F}$  and  $+160^\circ\text{F}$ , and to humidity between 0 and 100% RH.

Filter shall not be degraded by repeated vacuum cycles.

Filter shall be of epoxy laminated construction.

Table 2.

Laboratory for Particle Scattering  
Dudley Observatory  
100 Fuller Road  
Albany, New York 12205

Spec. Sheet 3940b  
Page two of three  
August 29, 1973

6. Diameter  $2.10 \pm 0.03$  inches  
Usable area shall exceed 1.95 inches in diameter.  
Thickness shall be less than  $3/16$  inches.  
Filter edges shall be chamfered. The chamfer shall extend a minimum 0.020 inches into the edge of the filter
7. The filter must meet all specifications over any  $1/4$  inch diameter, or larger area, anywhere on the filter.
8. Delivery must be made on or before 9 October 1973 at suppliers facility in Waltham, Mass. The supplier will notify the Laboratory for Particle Scattering, Dudley Observatory at least 48 hours before delivery is to be made.

Failure of the supplier to deliver on the above date will result in the automatic cancellation of the purchase order for this filter.

9. QUALITY ASSURANCE

CERTIFICATION OF COMPLIANCE required, referencing D. O. Purchase Order #1611 indicating that all hardware is as ordered and that all items are manufactured to normal quality standards. "THE GOVERNMENT HAS THE RIGHT TO INSPECT ANY OR ALL OF THE WORK INCLUDED IN THIS ORDER AT THE SUPPLIERS PLANT."

FOR USE IN MANNED SPACE FLIGHT PROGRAM, MANUFACTURING AND WORKMANSHIP HIGHEST QUALITY STANDARDS ARE ESSENTIAL IN ORDER TO INSURE RELIABILITY.

IF YOU ARE ABLE TO SUPPLY THE DESIRED ITEMS WITH A QUALITY WHICH IS HIGHER THAN THAT OF THE ITEM OFFERED OR PROPOSED, YOU ARE REQUESTED TO BRING THIS FACT TO THE IMMEDIATE ATTENTION OF THE PURCHASER.

Table 2 - continued

QUALITY ASSURANCE

As minimum the following controls are required:

A. Procurement Controls -

- (1) Contractor is responsible for the adequacy and quality of all purchased articles and materials.
- (2) Purchased raw material used shall be accompanied by chemical and/or physical test results.
- (3) Age control and life limited products shall be adequately marked. Vendor shall insure removal of outdated material.

B. Procured and fabricated articles and materials shall be inspected and tested to insure conformance to requirements set forth in this purchase order. Such inspection shall occur during receiving, processing, fabrication, assembly and testing.

C. Records of all inspections and tests shall be maintained. Such records shall provide evidence that required inspections and tests for the individual articles have been performed and shall include the article identification, the inspection, or test involved.

D. Non conforming articles shall be identified as such and segregated from the work operation. Such articles shall be scraped or called to the attention of Dudley Observatory for review.

E. Metrology Controls -

All estimation used in testing and measurement of articles purchased shall be calibrated to a source traceable to National Bureau of Standards or equivalent.

Table 2 - continued

### Neutral Density Filter Tests

Exposures of the sun were made through the P.I. neutral density filter to determine the best exposure for solar photography. This data was required for flight filter selection tests at Martin Marietta and for the pointing calibration picture during the operation of T025. An important supplemental result of this testing was the detection of a multiple imaging effect. This was caused by internal reflections within the filter due to its multiple layer characteristics. This multiple imaging, step wedge effect could be utilized to absolutely calibrate the flight film. As a result, this test was subsequently conducted at Martin Marietta to calibrate the flight neutral density filter.



### Interference Filter Calibration Tests

Photographs of the sun directly through both the P.I. and flight set of interference and polarizing filters were made to determine if multiple images, similar to that obtained through the neutral density filter, could be detected. This effect could be used as an additional calibration to the system. However, no multiple imaging effect was detected.

### Optimum Development

In order to maximize the resolution of Tri-X 2403 film, photographic processing tests were conducted using numerous developers and at a variety of development times. Developers D-76, acufine, and UFG were found to be superior and all generated approximately the same speed and resolution. Although PTD preferred to use D-19 due to their familiarity with it in the automatic processing machine, Kodak developer D-76 was selected for flight film processing due to its availability, compatibility with PTD automatic processing equipment, and superior resolution characteristics. Tri-X film developed in D-76 for  $8\frac{1}{2}$  minutes at  $70^{\circ}\text{F}$  generated a gamma value equal to one. We decided to have PTD process the flight film with the automatic machine due to its standardization and repeatability. However, we were disappointed with the results as they did not achieve the same degree of resolution that we had previously obtained by hand development.

### EVA Vibration Simulation

While monitoring astronaut EVA training exercises at the 1-G trainer at JSC, vibration of the coronagraph was detected during the operation of the experiment. Consequently, vibration damping tests were conducted to determine the extent of resolution degradation caused by the vibration. The small portable resolution board, constructed specifically for this test, was used along with NK01 electric Nikon and a 46 mm f/1.2 visible lens with Tri-X film.

Although vibration could be seen to continue for about 30 seconds, appreciable loss of resolution was not encountered after 10 seconds. Fig. 5 summarizes the vibration damping results. These results were supported by Pilot Pogue who commented during the November 22 EVA that the experiment seemed steady during operation, and by the high quality images on the in-focus frames returned.

ORIGINAL PAGE IS  
OF POOR QUALITY

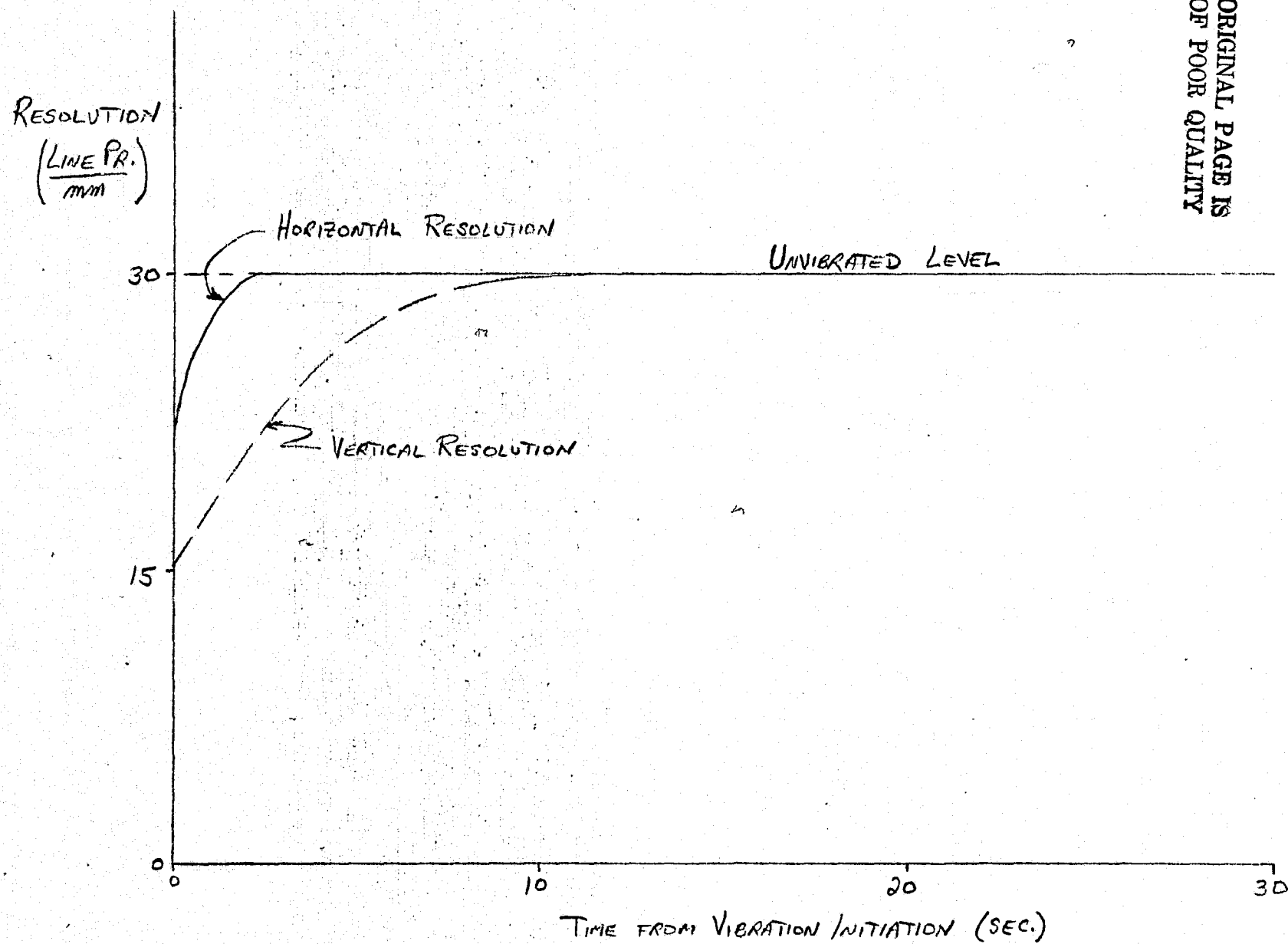


FIG. 5

### Kohoutek Flight Filter Resolution

Resolution tests were conducted with the set of 15 flight filters for Comet Kohoutek observations. To assure their quality and to obtain a better expectation of results from Skylab, the Nikon 27 mm f/2.0 UV lens was used with Tri-X film. The results of this test are presented in Table 3. We were generally very pleased with the high quality of resolution achieved over all wavelengths, particularly in the visible region since the UV lens was designed particularly for UV observations.

Table 3

Filter Resolution Summary

<u>P/N</u>	<u>S/N</u>	<u>H</u>	<u>V</u>
6000	03	39 lp/mm	35 lp/mm
5890	02	39	39
5500	02	39	35
4900	01	28	31
4700	01	28	28
4430	03	25	31
4262	01	49	49
3940	05	49	49
3873	01	62	62
3361	04	35	39
3250	03	24	31
3100	01	35	35
3600	06	55	55
2800	05	39	44
2530	04	31	31

### Refractive Index Tests

Refractive index tests were conducted on all the interference filters acquired for Comet Kohoutek observations. The tests were conducted on an optical bench using a specially created device to allow each filter to be precisely rotated to vary the angle of incidence ( $\phi$ ). Thus, by observing with a monochromator the shift in the peak wavelength of a filter at a number of incident angles, the index of refraction for that filter can be directly computed from:

$$n = \left[ \frac{\sin^2 \phi}{1 - \frac{\lambda_\phi^2}{\lambda_0^2}} \right]^{\frac{1}{2}}$$

Thus we can calculate the pass band for off axis images.

### Filter Photography Tests

Photographs were taken of the entire set of Kohoutek filters to detect pin holes, internal irregularities, UV leakage, and any other anomaly photographically detectable. A deuterium lamp was used to illuminate the ultraviolet filters and a carbon arc used for the remainder of the set. The results of this test were used for acceptance evaluation and flight filter determination.



### Occulting Disk Filter Tests

Photographs were made of the sun with the EVA modified coronagraph to determine the effect of the addition of the occulting disk filter (ODF) on the rejection ratio of the instrument and the crossover of the ODF with the Kohoutek set of interference filters. It was determined that a slight increase in density on the film could be attributed to the passage of light through the ODF only with the 6000Å and 5850Å filters. There was no detectable increase in density with the remainder of the filters. Additionally, the solar image appeared through the ODF filter for a one second exposure at f/2.0 with the UV lens only with the 6000Å, 5850Å, 3250Å, 3100Å, and 2800Å filters.

Since T025 was to be deployed and operated during several EVA's on SL-4, we became concerned about the extreme temperature variations often experienced around spacecraft and its possible adverse effect upon the transmission characteristics of the filters. Consequently, we constructed a thermally controlled vacuum chamber and established procedures for determining the transmission of the filters over a wide range of temperatures. However, subsequent tests conducted at Martin Marietta indicated that room temperatures (i.e. in the vicinity of 70°F) could be expected during the operation of the experiment. Since all our transmission tests were conducted at that temperature, no further testing was required.

### Point Source Tests

Point source tests were conducted to empirically determine with different films the limits of detectability for particles in space including both in and out-of-focus images. The theoretical detection of point sources depends upon the MTF of the system, which is dependent upon the camera lens, its focus, and the photographic film. However, we decided to use the empirical method as it was felt to be a more reliable method than the application of MTF and film functions. Consequently, in a series of tests using pinholes and spherical image reducers, we simulated a variety of micron-sized particles by point sources. We were able to use pinholes for images as small as  $3\text{ }\mu\text{m}$ . However, for smaller micron and sub-micron sized particles, a spherical image reducing technique was utilized. This consisted of a highly reflective ball bearing, of radius  $r$ , located at a distance  $d$  from a point source of diameter  $a$ . The effective image reduced diameter,  $a'$ , is equal to  $a \frac{r}{d}$ . Smaller point sources, below the resolution limit of the film were used to precisely attenuate the light level.

Initial problems encountered in setting up the experiment included a very limited area in which to work and a high level of background light. Consequently, both the pinhole and image reduction experiments were conducted inside the coronagraph test tunnel, where the background light level could be controlled.

It was found that Tri-X 2403 was generally a better detector

Point Source Tests - continued

than 2485. However, for larger images, substantially above the resolution of the film, 2485 exhibited superior detectability since the extreme graininess of the film did not significantly affect the results. This was also the case for images which were considerably out-of-focus.

Absolute results were never generated due to other immediate commitments at the time, such as the complete reorganization of T025 objectives for EVA and Kohoutek operations. Additionally, the loss of the meteoroid shield precluded the use of the solar airlock and eliminated contamination investigations as a functional objective.

Tests also proved commercial Tri-X to be similar to Tri-X 2403. As a result, we were able to use the less expensive and more readily available commercial Tri-X for all our testing.

Analysis of the point source tests indicated that the effective imaging properties of 2485 are such that the effectiveness is about the same as 2403 due to the grain effect of the film. It was determined that the minimum exposure required to obtain a detectable image of a  $3\text{ }\mu\text{m}$  solar illuminated point source was a  $1/4$  second exposure at 10 feet.

### S052 Point Source Defocus Simulation

Because approximately 10% of the several thousand S052 photographs contained out-of-focus particle tracks, we formalized an agreement with Dr. McQueen, Principal Investigator, to gain access to the data. Additionally, since one of the functional objectives of T025 was to photograph such particles, we had developed programs to reduce and analyze such data. Due to the fact that all the S052 photographs were focussed at infinity, all the particle track data available was out-of-focus. Therefore, tests were conducted to determine the relationships between photographing, at infinity, various sized sources at different distances using a lens of focal length similar to that used for S052. The results indicated that the point source size does not affect the image size on the film. Therefore, given the lens characteristics and the length of exposure, it is possible to determine the size of a point source from the image density, and the distance from the camera by means of the image size. Sample frames, containing several particle tracks, were digitized. However, they were not subsequently reduced due to time and funding limitations.

### Camera and Lens Historical Background

In order to provide a reflex viewing capability and a means of real-time discrimination in taking photographs, a Nikon camera was introduced to replace the previous Hasselbald camera system. It was felt that this would generate a much higher proportion of scientifically useful photographs. Two lenses, a 46 mm f/1.2 visible and a 27 mm f/2.0 UV, were included in the revised camera system. The loss of the meteoroid shield and the subsequent deployment of a solar parasol made operation of T025 in the solar scientific airlock impossible. The decision to operate the experiment during EVA on SL-4 required the utilization of the electric, battery operated motor driven Nikon camera instead of the manually operated camera.

### Plate Scale Tests

Plate scale tests were conducted with both the visible and UV lenses to determine an accurate function relating the distance from the center of the photograph frame to the viewing angle.

The experimental procedure consisted of photographing a bar of known length, in different positions in the frame, at a known distance from the camera. A function relating the distance  $\xi$  (in mm) from the center of the frame to the viewing angle  $\theta$  (in degrees) was derived as follows:

For the visible lens:

$$\theta = 94.07 \arctan (.01091 \xi)$$

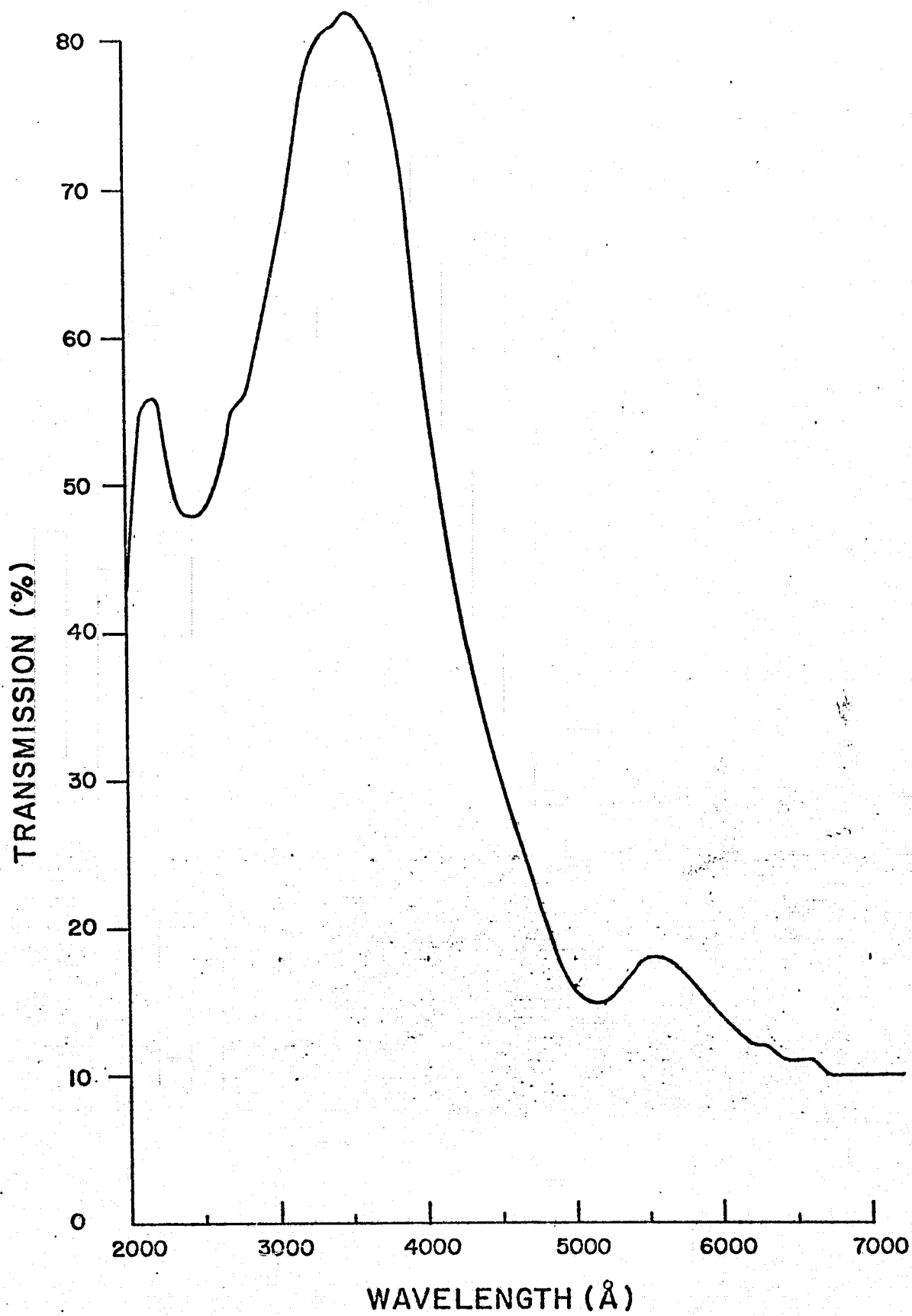
For the UV lens:

$$\theta = 92.942 \arctan (.011090 \xi)$$

### UV Lens Transmission Determination

Since the published transmission curve for the UV lens covered the 2000-4000Å range only, the extension of this curve, within the sensitivity range of the film, was generated.

The procedure to determine the unknown transmission values was to photograph a uniformly illuminated (ground glass) field with both the visible and UV lenses at f/2.0. Interference filters with a central wavelength of 4430Å, 4700Å, 5000Å, and 6000Å were used to determine the ratio of transmissions of the two lenses at each of these wavelengths. Since the transmission of the visible lens was known, the transmission of the UV lens was determined. The results are plotted in Fig. 6.



ORIGINAL PAGE IS  
OF POOR QUALITY

Fig. 6



### Defocus Simulation

Tests were conducted with both the manual Nikon and electric Nikon camera bodies to determine the reason an out-of-focus condition existed on most of the T025 photographic data.

Initially, photographic tests were conducted to determine the degree of "defocusing" caused by the K1 adapter on the UV lens to determine whether the use of the adapter could be a possible cause of the majority of T025 photographs being out-of-focus. Photographs were taken of Sirius directly and toward the sun with the 27 mm UV lens with and without the K1 adapter. It was determined that the K1 adapter did not defocus the image similar to the flight film. Therefore, the K1 adapter could not be the cause of the "defocused" flight film. This was subsequently verified by the crew during debriefing. Since five other experiments using the same camera body (NK02) experienced similar photographic degradation, the most logical explanation for the problem is that the pressure plate, which maintains the film in the focal plane and can very easily be removed from the camera back, was somehow lost. Tests conducted at Dudley, using the electric Nikon camera body with the pressure plate removed, reproduced the out-of-focus condition of the flight photographs.

### Lens/Filter Scatter Tests

Tests were conducted to determine the extent of internal scattering within the 27 mm UV lens. The experimental procedure was to photograph carbon arc illuminated white strips on a black background to simulate an atmosphere. Generally, the amount of scatter caused by the lens was insignificant although a minimal background effect could be possible in the extreme upper portion of the atmosphere of flight photographs. However, this scattering effect could be subtracted out of the photos by examination of the complete set of flight photographs and calibration of the scattering effect.

Additional tests were conducted with the returned set of flight filters to determine, if any, additional scattering effect could be introduced by the addition of a filter. Scattering produced by the flight 2530 filter was found to be quite significant, while no significant scatter resulted from the 3600Å filter.

### Vignetting Tests

Tests were conducted to determine the attenuation, due to vignetting, as a function of radial and angular distance from the optical axis of the T025 coronagraph with the Nikon camera and 27 mm UV lens. The experiment consisted of photographing three tungsten filament 25 watt light bulbs mounted 10 feet in front of a black wall using the T025 coronagraph, Nikon UV lens and camera with Tri-X film. The coronagraph was placed 50 feet from the three lamps. The current to the lamps, fixed rigidly in position, was regulated to maintain a constant light output. The camera was oriented to simulate the Skylab EVA position and the coronagraph was rotated so that the lamps could be photographed in different areas of the field of view. A telescope with cross hair was mounted inside the coronagraph occulting disk to provide an in-focus center of frame reference for the fixed focus UV lens.

For reduction, the X and Y position of each lamp was determined with respect to the center of the field and the density of each lamp image was measured. As a result, an equation was determined using the least squares method relating the radial distance R from the center of the field to the attenuated irradiance  $S_R$ .

The relation is given by:

$$S_R = 1.0 - (4.15 \pm .11) \times 10^{-3} R^2$$

where  $S_0 = 1.0$ .

## Sensitometer Design and Calibration

In order to have the capability to calibrate film for data reduction, a sensitometer was constructed to generate a repeatable range of densities in 15 steps on the film. The calibration of laboratory and flight films required that a means of irradiating the film with a known amount of light be created. Consequently, a sensitometer, based on a design developed by HAO, was constructed. Numerous tests were made to calibrate and determine the proper exposure for all film used in the course of our studies.

The sensitometer was at first only relatively calibrated by making precise transmission measurements of each step of the inconel step wedge using a Joyce-Loebl Microdensitometer. From the determined transmissions, the relative irradiance on the film was calculated. Later, because of the special needs of the T025 experiment, these irradiances were calculated in absolute terms by directly comparing the T025 sensitometer step wedge with an absolutely calibrated wedge from JSC/PTD. By this comparison, direct conversion was then possible from the T025 calibrated wedge to absolute irradiances in  $\text{ergs/cm}^2\text{-sec}$ .

A second, more compact, UV sensitometer was constructed utilizing the Nikon 27 mm UV lens. The UV sensitometer provided us the capability to achieve a calibration in the UV (1800 to 4000 $\text{\AA}$ ) region. UV filters were used to provide spectral discrimination over this entire range. Although exposures were established, the UV sensitometer was never operationally utilized due to the major reduction by NASA of

Sensitometer Design and Calibration - continued

the amount of calibration film we were permitted to fly on board Skylab. This made it impossible to fly sufficient calibration film to adequately cover the range of filters and exposures required for flight operation of T025. Consequently, as a result of a vast number of photographic observations with Tri-X films, we were forced to apply reciprocity corrections for all the exposures in the observing program based on results from our ground control films. Although a reasonably reliable reciprocity correction factor was derived in this manner, the error introduced in the reciprocity determination for all densities and wavelengths are significant. We feel that it was poor scientific procedure however, to limit the amount of calibration film for a photographic experiment to only operational films when the film was expected to experience a large radiation dose. Reciprocity can not be firmly established from ground control tests under these conditions.

### Extension of Sensitometer Wedge Latitude

We attempted to extend the latitude of the sensitometer wedge by introducing neutral density filters into the sensitometer. However, due to internal reflections and scatter within the sensitometer, the low flux levels required for latitude extension were not possible.

### Sensitometry Deteoriation

Tests were conducted to determine whether sensitometry exposures made over a period of 16 days would deteoriate or otherwise be affected by a lapse of time. Plots of both the step function and individual density steps with time exhibited no detectable fluctuation. Further comparison of some sensitometer wedges taken over a few years had the unusual result of actually indicating an increase in film speed in some cases.

### Vacuum Effect on Sensitometry

Since the T025 flight film would be subjected to vacuum conditions during the EVA operations on SL-4, tests were conducted to determine whether a vacuum condition would have any effect on the sensitivity of 2403 Tri-X flight film. The results of these tests did not conclusively demonstrate a change in sensitivity, i.e. the loss or gain in sensitivity was less than  $\Delta \log E < .1$ .



### Microdensitometer

A Joyce-Loebl scanning microdensitometer, along with associated digitization hardware, was received as Government Furnished Equipment for photographic data reduction and digitization. The instrument was completely refurbished and subsequently housed on a vibrationally isolated table in an environmentally controlled laminar flow clean room in the Laboratory for Particle Scattering. This proved to be very beneficial as it provided us the capability to environmentally control all microdensitometer testing. Initial reduction of the flight film generated poor magnetic tape records when recording large amounts of data and this necessitated the complete refurbishment of the digital stepping recorder. Because our microdensitometer was non-operational for this period of time and because no precise position indication was provided by the Joyce-Loebl, we decided to digitize the flight negatives with the Spec - Scan microdensitometer at JSC.

In the process of preparing the Joyce-Loebl for operation, numerous tests and calibrations were required. In order to have the ability to compare our measurements directly with those from the JSC Spec - Scan as well as the results of other investigations, the Joyce-Loebl was calibrated in diffuse density units. Inconel filters, whose spectral transmission had been previously determined with the Jarrell-Ash monochromator, were used for the absolute calibration of the instrument. A secondary set of neutral density filters were also calibrated with respect to the inconel filters for daily recalibration of the instrument.

Microdensitometer - continued

The microdensitometer ratio arms were precisely calibrated using a Bauch and Lomb standard microscope scale. This enabled us to attain precise specimen positioning during microdensitometer measurements.

Stability and reproducibility tests of the microdensitometer were also conducted. As a result, we obtained very high reproducibility and were able to maintain linearity and calibration with very low drift.

### Diffuse Density Calibration

An experiment was conducted to relate diffuse density to the Joyce-Loebl instrument specular density  $D$ . A Kodak calibration step-wedge was used as a reference for diffuse density and a density ( $D'$ ) to diffuse density ( $D$ ) relationship of  $D = 1.32 D'$  was obtained.

## Rejection Ratio Determination, Flight Film

White Light: Two methods were employed to generate rejection ratio values from the flight photographs. The first method utilized the actual measured energy of the solar image on the film modified by a factor correcting for the limited transmission through the occulting disk filter. This value was then used to calculate the rejection ratio over the field. The optimum rejection ratio measured and calculated by this method was  $2.88 \times 10^{-8}$  at 4.4 mm from the sun on the film (frame BE03-01). The second method calculated the theoretical energy of the solar disk on the film. Lens transmission, solar spectral irradiance, the normalized film sensitivity, the area of the lens surface, and the area of the solar image on the film were introduced into the calculations. Maximum rejection was  $2.14 \times 10^{-8}$  at 4.4 mm.

3600Å Filter: The procedure for calculating the rejection ratio with the 3600Å filter was similar to method #2 for white light except the filter transmission was introduced into the calculations. A rejection ratio of  $1.03 \times 10^{-8}$  was calculated.

### Image Restoration

Subsequent to receipt of the out-of-focus flight photographs, conversations with experts at Goddard Space Flight Center, Jet Propulsion Laboratory, and the State University of New York at Albany indicated to us that image processing techniques could possibly restore a major portion of the blurred data. Numerous defocus simulation tests including point and line spread image tests were conducted by shimming the film in the electric flight-type Nikon away from the focal plane. These tests were conducted to recreate the out-of-focus condition observed on the flight film in order to define the lens and camera properties required for image restoration. After a careful inspection of the point and line spread functions and recognizing the uncertainties involved in the exact reproduction of the out-of-focus condition, we felt that precise image restoration could not be guaranteed and therefore, considering the limited time available for reduction, we decided not to pursue the matter further.